

Gas explosions in process pipes

Kjetil Kristoffersen

Telemark University College
Faculty of Technology
Porsgrunn, Norway

Thesis submitted for the degree of Dr. Ing.
NTNU / HiT 2004

Contents

Preface	xii
Abstract	xiii
Nomenclature	xiv
1 Introduction	1
1.1 Background	1
1.1.1 Examples of explosions in industrial pipelines	2
1.2 Objective	3
1.3 Overview of thesis	5
2 Theory on flame propagation in pipes	6
2.1 Introduction	6
2.1.1 Propagation regimes	6
2.2 Ignition sources	8
2.3 Laminar flame propagation	8
2.3.1 Initial flame propagation	8
2.3.2 Flame wrinkling by instability mechanisms	13
2.4 Turbulent flame propagation	16
2.5 Criteria for FA	21
2.6 Modeling of flame propagation	22
2.6.1 Models for turbulent burning velocity	22
2.7 Experimental work on flame propagation in pipes	23
2.8 DDT	27
2.8.1 Experimental studies of DDT	28
2.8.2 Mechanisms involved in DDT	31
2.8.3 Criteria for DDT	34
2.8.4 Models for DDT	35

3	Experiments	37
3.1	Experimental details	37
3.1.1	Pipes	37
3.1.2	Ignition system	39
3.1.3	Gas handling system	39
3.1.4	Diagnostic systems	41
3.1.5	Data acquisition system	46
3.2	Test of Kistler pressure transducers	46
3.3	Experimental results	48
3.3.1	Propane-air mixtures in various lengths of steel pipes	49
3.3.2	Propane-air mixtures in a 2 m steel pipe	58
3.3.3	Acetylene-air mixtures in a 2 m steel pipe	66
3.3.4	Acetylene-air mixtures in a 5 m steel pipe	70
3.3.5	Hydrogen-air mixtures	72
3.3.6	Propane-air mixtures, SLR camera	74
3.3.7	Propane-air mixtures, high speed camera	78
4	Numerical simulations	80
4.1	FLACS	80
4.1.1	Flame models in FLACS	80
4.1.2	Burning velocity	83
4.1.3	Turbulent viscosity	84
4.1.4	Courant numbers	85
4.1.5	Simulations	85
4.1.6	Summary FLACS	92
4.2	Random Choice Method	92
4.2.1	The Riemann problem for the Euler equations	93
4.2.2	Solution of the Riemann problem by the RCM	96
4.2.3	Combustion model	97
4.2.4	Method for estimation of the quasi 1D burning velocity	98
4.2.5	Determination of pipe outlet conditions	100
4.2.6	Modeling of heat loss and friction	101
4.2.7	Simulation of experiments	103
5	Conclusions	123
5.1	Main conclusions	123
5.2	Recommendations for further work	126
5.3	End statement	126

List of Figures

1.1	A view of the pipeline that was destroyed during the incident at Hydro Agri Porsgrunn (Norsk Hydro ASA).	3
1.2	Project Road Map	4
2.1	Regimes of flame propagation from ignition to DDT (Dorofeev, 2002).	7
2.2	The flame front at two positions. The angle θ to the pipe wall is indicated (Guénoche, 1964).	9
2.3	Representation of the flame front as a cylinder connected to a hemisphere (Clanet and Searby, 1996).	9
2.4	Reduced pressure versus reduced time. t_{wall} and t_{tulip} are pointed out (Clanet and Searby, 1996).	10
2.5	Photographs of the flame propagation in a closed pipe (Ellis and Wheeler, 1928).	10
2.6	The inversion of the flame front. The pictures are taken just before, during and just after the tulip flame inversion (Clanet and Searby, 1996).	11
2.7	Example of how the flame front again can become convex towards the unburnt mixture (Guénoche, 1964).	12
2.8	Shape of flame front for propagation in a normal gravity field (left) and a microgravity field (right) (Kawakami et al., 1999).	12
2.9	Deviation in flow lines leading to the Darrieus-Landau instabilities (Clanet and Searby, 1998).	14
2.10	The mechanism of thermal-diffusive instability (Williams, 1985).	15
2.11	Normalized turbulent burning velocities versus normalized turbulent intensity (Shy et al., 2000). Data obtained by Bradley (1992) and Shy et al. (2000). The numbers used are the turbulent Reynolds number (Re), the Karlovitz number (Ka or K), and the Lewis number (Le).	17
2.12	The Borghi diagram (He, 2000).	18
2.13	Interaction of a hemispherical flame front with a rarefaction wave (Laviollette et al., 2003).	20

2.14	Schematic description of the experimental set-up to Chatrathi et al. (2001).	24
2.15	Shlieren photographs of the flame in propane-air mixtures at equivalence ratios of 0.8 and 1.0 (Schmidt et al., 1952). The flame is propagating from a closed towards an open pipe end.	25
2.16	Various locations of transition to detonation observed in $2H_2 + O_2$ mixtures: (a) onset between flame and shock, (b) onset at flame front, (c) onset at shock front, (d) onset at a contact discontinuity (Kuo, 1986, after Urtiew and Oppenheim, 1966).	27
2.17	Schematic description of shock tube with several spherical flames. A computational domain is stated (Thomas et al., 1997).	28
2.18	Demonstration of the determination of the L/D ratio at DDT. 6" pipe, 6.5% ethylene (Chatrathi et al., 2001).	29
2.19	The effect of pipe diameter on the L/D ratio at the deflagration to detonation transition distance, for different fuels (Chatrathi and Going, 1996).	30
2.20	General phases observed during a transition to detonation event following turbulent acceleration (Thomas, 1999).	32
2.21	Typical pressure histories expected at locations (a)-(d) in Figure 2.20 (Thomas, 1999).	33
2.22	Formation of a temperature gradient in the boundary layer along a wall (Bartenev and Gelfand, 2000).	33
2.23	Formation of a temperature gradient between a shock wave and flame front (Bartenev and Gelfand, 2000).	34
2.24	Formation of temperature and pressure gradients ahead of a flame front. T_{selfign} is the self-ignition temperature (Bartenev and Gelfand, 2000).	34
3.1	The circular steel pipes used in the experiments. Pipe lengths of 1, 2, 5 and 11 m are used. Lengths are given in mm.	38
3.2	Piston cylinder and plexiglass pipe with the ignition electrodes and the gas inlet tube.	39
3.3	System for ignition of gas mixture and generation of a trigger signal to the logging system. c is the capacitor.	40
3.4	The spark produced between the two electrodes.	40
3.5	Kistler 603B, $D = 5.5$ mm (left) and 7261, $D = 35$ mm (right), (Kistler Instrument Corp.).	42
3.6	Dimensions for the mounting of Kistler 7261 to the pipe. Dimensions are given in mm.	42

3.7	Dimensions for the mounting of Kistler 603B to the pipe. Dimensions are given in mm.	43
3.8	The pipe cross section at the placements of Kistler 603B transducers. Dimensions are given in mm.	43
3.9	The optical sensor TSL250 consists of a photodiode and an amplifier. V is the supply voltage and R_I is the input resistance (Texas Instruments Inc, 1995).	44
3.10	Data for TSL250, a) output voltage versus irradiance, b) spectral responsivity versus wavelength and c) maximum output voltage versus supply voltage (Texas Instruments Inc, 1995).	45
3.11	Mechanical data for TSL250 (Texas Instruments Inc, 1995).	45
3.12	Results of shock-tube experiments and simulations. Three transducers are tested.	47
3.13	Experimental results for two stoichiometric propane-air mixtures in the 1 m steel pipe. The pressure values recorded at the four transducer positions along the pipe are shown at their locations.	50
3.14	Experimental results for two propane-air mixtures at $\phi = 1.2$ in the 1 m steel pipe. The pressure values recorded at the four transducer positions along the pipe are shown at their locations.	51
3.15	Experimental results for two propane-air mixtures at $\phi = 1.0$ in the 2 m steel pipe. The pressure values recorded at the four transducer positions along the pipe are shown at their locations.	52
3.16	Frequency spectrum for the pressure oscillations in the 2 m steel pipe with a stoichiometric propane-air mixture.	52
3.17	Experimental results for two propane-air mixtures at $\phi = 0.8$ in the 5 m steel pipe. The pressure values recorded at the four transducer positions along the pipe are shown at their locations.	53
3.18	Experimental results for two propane-air mixtures at $\phi = 1.0$ in the 5 m steel pipe. The pressure values recorded at the four transducer positions along the pipe are shown at their locations.	54
3.19	Maximum pressure recorded in the experiment for various equivalence ratios of propane-air mixtures in the 5 m pipe.	54
3.20	The first maximum pressure recorded at transducer 1 for propane-air mixtures at various equivalence ratios in the 5 m pipe.	55
3.21	Experimental results for two propane-air mixtures at $\phi = 1.0$ in the 11 m steel pipe. The pressure values recorded at the four transducer positions along the pipe are shown at their locations.	56

3.22	First frequency mode from an FFT analysis of the pressure records compared to the resonance frequency in unburnt gas. Stoichiometric propane-air mixtures.	57
3.23	Pressure records at the first transducer for the three pipe lengths. Propane-air mixtures at equivalence ratio 1.0.	58
3.24	Experimental results for propane-air mixture at $\phi = 0.9$ in the 2 m steel pipe. The pressure and photodiode records are shown at their four positions along the pipe.	59
3.25	Experimental results for propane-air mixture at $\phi = 1.0$ in the 2 m steel pipe. The pressure and photodiode records are shown at their four positions along the pipe.	60
3.26	Experimental results for propane-air mixture at $\phi = 1.1$ in the 2 m steel pipe. The pressure and photodiode records are shown at their four positions along the pipe.	61
3.27	Experimental results for propane-air mixture at $\phi = 1.2$ in the 2 m steel pipe. The pressure and photodiode records are shown at their four positions along the pipe.	62
3.28	Experimental results for propane-air mixture at $\phi = 1.4$ in the 2 m steel pipe. The pressure and photodiode records are shown at their four positions along the pipe.	62
3.29	Experimental results for propane-air mixture at $\phi = 1.5$ in the 2 m steel pipe. The pressure and photodiode records are shown at their four positions along the pipe.	63
3.30	Average flame speed to photodiodes 3 or 4 for various propane-air mixtures in the 2 m steel pipe.	64
3.31	Time of the first pressure maximum for experiments with various propane-air mixtures in the 2 m steel pipe.	64
3.32	Flame arrival times at the four photodiodes for various propane-air mixtures in the 2 m steel pipe.	65
3.33	Flame arrival times at the four photodiodes for various propane-air mixtures in the 2 m steel pipe. (Enlarged version of Figure 3.32)	65
3.34	Experimental results for acetylene-air mixture at $\phi = 0.8$ in the 2 m steel pipe. The pressure and photodiode records are shown at their four positions along the pipe.	67
3.35	Experimental results for acetylene-air mixture at $\phi = 1.0$ in the 2 m steel pipe. The pressure and photodiode records are shown at their four positions along the pipe. Maximum value at transducer 4 is 629.8 kPag.	68

3.36	Experimental results for acetylene-air mixture at $\phi = 1.2$ in the 2 m steel pipe. The pressure and photodiode records are shown at their four positions along the pipe. Maximum values for the pressure peaks that have been cut off are in chronological order 367.6 kPag, 364.2 kPag and 796.3 kPag.	68
3.37	First pressure peak at transducer 1 versus equivalence ratio for acetylene-air mixtures in the 2 m steel pipe.	69
3.38	Average flame speed versus equivalence ratio for acetylene-air mixtures in the 2 m steel pipe.	69
3.39	Example of pressure histories for an acetylene-air mixture at $\phi = 1.1$. The initial positions are displaced with 5 kPa for each transducer to make the figure more readable.	71
3.40	The times after ignition at which the maximum recorded pressure occurs. The transducer positions where the pressures are measured are indicated by symbols. Experiments with acetylene-air mixtures in the 5 m steel pipe.	71
3.41	Flame speed between transducer 3 and 4 for acetylene-air mixtures in the 5 m steel pipe. The CJ values from SuperSTATE are indicated by the solid line.	72
3.42	Experimental results from an experiment with hydrogen-air mixture at $\phi = 1.1$ in the 2 m steel pipe.	73
3.43	Finger shaped flame front.	73
3.44	Flame front influenced by gravity.	74
3.45	Flame front disturbed by pressure waves. The flame is probably a vortex ring along the pipe wall.	75
3.46	Picture captured with open shutter of the flame propagation in the 1.9 m plexiglass pipe for a propane-air mixture at $\phi = 0.8$. The amount of blue colour in the picture is shown in the upper part.	76
3.47	Experimental results for a propane-air mixture at $\phi = 1.0$ in the 1.9 m plexiglas pipe.	76
3.48	Picture captured with open shutter of the flame propagation in the 1.9 m plexiglass pipe for a propane-air mixture at $\phi = 1.0$. The amount of blue colour in the picture is shown in the upper part.	77
3.49	Picture captured with open shutter of the flame propagation in the 1.9 m plexiglass pipe for a propane-air mixture at $\phi = 1.2$. The amount of blue colour in the picture is shown in the upper part.	77

3.50	Pictures captured with a high speed camera of the flame propagation in the 1.9 m plexiglass pipe. Propane-air mixture at $\phi = 1.0$	78
3.51	Pictures captured with a high speed camera of the flame propagation in the 1.9 m plexiglass pipe. Propane-air mixture at $\phi = 1.2$	79
4.1	The six possible configuration types for fluid interfaces in a control volume (Noh and Woodward, 1976).	83
4.2	Simulations in FLACS with a stoichiometric propane-air mixture for various CFLC numbers. 11 grid cells are used in each direction of the cross section and the default model for generation of turbulent viscosity is applied.	87
4.3	Maximum pressure at the second peak for various CFLC numbers. Simulations in FLACS with a stoichiometric propane-air mixture. 11 grid cells are used in each direction in the cross section and the default model for generation of turbulent viscosity is applied.	87
4.4	Simulations in FLACS with a stoichiometric propane-air mixture for various numbers of grid cells in the pipe cross section. CFLC = 0.5 and the default model for generation of turbulent viscosity is applied.	88
4.5	The maximum pressure at the second peak for various numbers of grid cells in the pipe cross section. Simulations in FLACS with a stoichiometric propane-air mixture. CFLC = 0.5 and the default model for generation of turbulent viscosity is applied.	89
4.6	Maximum pressure at the second pressure peak for various CFLC numbers and models for generation of the turbulent viscosity (Table 4.1). Simulations in FLACS with a stoichiometric propane-air mixture and with 11 grid cells in each direction in the pipe cross section.	90
4.7	Maximum pressure at the second pressure peak for various numbers of grid cells in each direction in the pipe cross section and for various models for generation of the turbulent viscosity (Table 4.1). Simulations in FLACS with a stoichiometric propane-air mixture and with CFLC = 0.5.	91
4.8	Test of the combustion model with 7 grid cells in each direction of the cross section and with CFLC = 1. Simulations in FLACS with a stoichiometric propane-air mixture.	91
4.9	Principles for a shock tube.	93
4.10	Possible wave patterns of a Riemann problem.	94
4.11	Piecewise constant distribution.	96
4.12	Sampling scheme of RCM.	98

4.13	The combustion model used in RCMLAB.	99
4.14	Location of Δp (x_{TD}, t_{TD}).	99
4.15	Simulation in RCMLAB of a propane-air mixture at $\phi = 1.0$ in the 1 m steel pipe.	105
4.16	Simulation in RCMLAB of a propane-air mixture at $\phi = 1.2$ in the 1 m steel pipe.	105
4.17	Estimated quasi 1D burning velocity for $\phi = 1.0$ and 1.2 for propane-air mixtures in the 1 m steel pipe.	106
4.18	Simulation in RCMLAB of a propane-air mixture at $\phi = 1.0$ in the 2 m steel pipe.	107
4.19	Pressure histories at transducer position 3 from experiment and simulation in RCMLAB with a stoichiometric propane-air mixture in the 2 m steel pipe. The simulation has an offset of 5 kPa. The transducers used for estimation of the quasi 1D burning velocity are indicated. . . .	107
4.20	Simulation in RCMLAB of a propane-air mixture at $\phi = 1.0$ in the 5 m steel pipe.	108
4.21	The estimated quasi 1D burning velocity for three pipe lengths. Propane-air mixtures at $\phi = 1.0$	109
4.22	Estimated quasi 1D burning velocity for stoichiometric propane-air mixtures in steel pipes of different lengths. The transducers used for estimation of the quasi 1D burning velocity are indicated.	110
4.23	Simulation in RCMLAB of a propane-air mixture at $\phi = 0.9$ in the 2 m steel pipe.	110
4.24	Simulation in RCMLAB of a propane-air mixture at $\phi = 1.2$ in the 2 m steel pipe.	111
4.25	Simulation in RCMLAB of a propane-air mixture at $\phi = 1.5$ in the 2 m steel pipe.	112
4.26	The density development ahead of the flame front for a simulation in RCMLAB of a propane-air mixture at $\phi = 1.2$	113
4.27	The simulated flame positions for four trials with propane-air mixtures at $\phi = 0.9, 1.0, 1.2, 1.5$	113
4.28	The estimated quasi 1D burning velocity, S , for propane-air mixtures at three equivalence ratios in the 2 m pipe.	114
4.29	Simulation in RCMLAB of a acetylene-air mixture at $\phi = 1.0$ in the 2 m steel pipe.	115
4.30	Estimated quasi 1D burning velocity for a stoichiometric acetylene-air mixture in the 2 m steel pipe.	115

4.31	Light emission from experiment and integrated local burning rate from simulation. Propane-air mixture at $\phi = 0.8$ in the plexiglass pipe. . . .	116
4.32	Light emission from experiment and integrated local burning rate from simulation. Propane-air mixture at $\phi = 1.0$ in the plexiglass pipe. . . .	117
4.33	Light emission from experiment and integrated local burning rate from simulation. Propane-air mixture at $\phi = 1.2$ in the plexiglass pipe. . . .	117
4.34	Simulation of an experiment with a stoichiometric propane-air mixture. The simulated pressure histories are shifted 5 kPa above the experimental histories. The transducers used for estimation of the quasi 1D burning velocity are indicated.	119
4.35	Pictures from the high speed camera compared to simulated flame position. Propane-air mixture at $\phi = 1.0$	119
4.36	Pictures from the high speed camera compared to simulated flame position. Propane-air mixture at $\phi = 1.2$	120
4.37	The density development ahead of the flame front for a simulation in RCMLAB of a propane-air mixture at $\phi = 1.0$ in the plexiglass pipe. . .	120
4.38	Quasi 1D burning velocities for simulations at three equivalence ratios with propane-air mixtures in the plexiglass pipe. The transducers used for estimation of the quasi 1D burning velocity are indicated.	121
4.39	Quasi 1D burning velocities for simulations at three equivalence ratios with propane-air mixtures in the 1.9 m plexiglass pipe. The transducers used for estimation of the quasi 1D burning velocity are indicated. . . .	121

List of Tables

2.1	Run-up distance for DDT obtained by Chatrathi et al. (2001).	29
3.1	Experimental work, only diagnostics other than pressure transducers are given.	49
4.1	Models for generation of turbulent viscosity.	86
4.2	Number of grid cells used in each direction of the pipe cross section and the associated grid sizes.	88
4.3	Simulations performed in RCMLAB. References to the experimental campaigns are indicated.	104

Preface

This work has been carried out at Telemark Technological Research and Development Centre (Tel-Tek) and Telemark University College (HiT), Faculty of Technology. Financial support from Norsk Hydro ASA is gratefully acknowledged.

I want to thank Professor Dag Bjerketvedt for his clever supervising of this work, and for his patience and many creative suggestions that have brought this work ahead. His infectious enthusiasm in the field of combustion is very much appreciated.

A reference group was established for this project. The group members were Professor Dag Bjerketvedt from HiT/Tel-Tek and dr. Olav Sæter, dr. Jan Pappas and dr. Erik Odgaard from Norsk Hydro ASA. I want to thank the members of the reference group for spending time on our meetings and for all useful discussions. Special thanks to dr. Olav Sæter for his guidance and encouragement, for introducing me to FLACS and for cooperation during projects at Hydro Research Centre.

I want to thank GexCon AS for their contributions to my work with FLACS. Discussions with Idar Storvik, dr. Bjørn Arntzen and R&D Director Olav Roald Hansen are appreciated.

Thanks also to colleagues at HiT and Tel-Tek, especially Professor Torstein K. Fanneløp and Professor Are Mjaavatten for the useful discussions and advice, my fellow Ph.D. students Knut Vågsæther and Nina Bjerkebo Brovig, divisional engineer Talleiv Skredtveit for his contribution during the construction of experimental equipment and lecturer Jan Gunnar Lode for his contribution with the optical sensors. I would also like to thank M.Sc. Bjørnar Johnsen for his contribution during the experiments with the plexiglass pipe, Torstein Johnsen for taking the pictures with the SLR camera, Per Otto Ålråk from Saven Hitech for capturing the high-speed film, and the Norwegian Defence Estates Agency for placing experimental equipment at my disposal.

Porsgrunn, 2004

Kjetil Kristoffersen

Abstract

In this thesis, gas explosions inside pipes are considered. Laboratory experiments and numerical simulations are the basis of the thesis.

The target of the work was to study gas explosions in pipes and to develop numerical models that could predict accidental gas explosions inside pipes.

Experiments were performed in circular steel and plexiglass pipes. The steel pipes have an inner diameter of 22.3 mm and lengths of 1, 2, 5 and 11 m. The plexiglass pipe has an inner diameter of 40 mm and a length of 1.9 m. Mixtures of propane, acetylene and hydrogen with air at various equivalence ratios were used. Pressure was recorded by Kistler pressure transducers and flame propagation was captured by photodiodes, a SLR camera and a high-speed camera. The experiments showed that acoustic oscillations would occur in the pipes, and that the frequency of these oscillations are determined by the pipe length. Several inversions of the flame front can occur during the flame propagation in a pipe. These inversions are appearing due to quenching of the flame front at the pipe wall and due to interactions of the flame front with the longitudinal pressure waves in the pipe. Transition to detonation was achieved in acetylene-air mixtures in a 5 m steel pipe with 4 small obstructions.

Simulations of the flame propagation in smooth pipes were performed with an 1D MATLAB version of the Random Choice Method (RCMLAB). Methods for estimation of quasi 1D burning velocities and of pipe outlet conditions from experimental pressure data were implemented into this code. The simulated pressure waves and flame propagation were compared to the experimental results and there are good agreements between the results.

Simulations were also performed with the commercial CFD code FLACS. The code was tested for gas explosions in smooth pipes and the results compared to experimental results. To properly handle the longitudinal pressure oscillations in pipes, at least 7 grid cells in each direction of the pipe cross-section and a Courant number (CFLC) of maximum 1 should be used. It was shown that the current combustion model in FLACS gave too high flame speeds initially for gas explosions in a pipe with an inner width of 40 mm.

Nomenclature

Latin letters

Symbol	Unit	Description
A	m^2	area
A_i		number in the Van der Corput sequence
A_l		constant in RCMLAB
A_r		constant in RCMLAB
A_T	m^2	wrinkled flame area
AC	$1/\text{m}$	parameter defining area increase
a		constant in FLACS
B_l		constant in RCMLAB
B_r		constant in RCMLAB
C		Courant number in RCMLAB
C_f		friction factor
C_p	$\text{J}/\text{kg K}$	heat capacity at constant pressure
c	m/s	speed of sound
c_b	m/s	speed of sound in burnt mixture
c_l	m/s	speed of sound to the left
c_r	m/s	speed of sound to the right
c_u	m/s	speed of sound in unburnt mixture
D	m	pipe diameter
Da		Damköhler number ($Da = \frac{l_T S_L}{\delta u'}$)
E	J	energy
f		volume fractions
h	$\text{W}/\text{m}^2 \text{K}$	heat transfer coefficient
IL		fluid occupation number in control volume to the left
IR		fluid occupation number in control volume to the right

Symbol	Unit	Description
i		index number
K	kg m ² /s	gain
Ka		Karlovitz number ($Ka = \frac{\delta/S_L}{\sqrt{\nu/\varepsilon}}$)
k	m ² /s ²	turbulent kinetic energy
k_{angle}		angle of expansion
L	m	length
L_{DDT}	m	run-up distance to DDT
Le		Lewis number ($Le = \lambda/\varkappa$)
l_F	m	flame thickness
l_T	m	integral length scale
$l_{T,\text{min}}$	m	minimum integral length scale for DDT
Ma		Markstein number
m		number in the Van der Corput sequence
n		natural numbers
nt		number of grid cells in a pipe in RCMLAB
Pr		Prandtl number
p	kPa	pressure
p_*	kPa	pressure at contact surface
p_l	kPa	pressure at left side
p_{RCM}	kPa	pressure from RCMLAB
p_r	kPa	pressure at right side
p_{TD}	kPa	pressure from transducer
\dot{Q}	W/m ²	heat flux
R	J/K mol	gas constant
R_I	Ω	input resistance
Re		Reynolds number
Re _T		turbulent Reynolds number
r	m	pipe radius
r		recovery factor
S	m/s	quasi 1D burning velocity
S_L	m/s	laminar burning velocity
S_{QL}	m/s	quasi laminar burning velocity
S_T	m/s	turbulent burning velocity
T	K	temperature
T_F	K	flame temperature

Symbol	Unit	Description
T_r	K	recovery temperature
T_{selfign}	K	self-ignition temperature
t	s	time
t_F	s	flame time scale ($t_F = \delta/S_L$)
t_K	s	Kolmogorov time scale ($t_K = \sqrt{\nu/\varepsilon}$)
t_T	s	integral time scale ($t_T = l_T/u'$)
t_{TD}	s	time for x_{TD}
t_{sphere}	s	time when flame front changes from spherical to finger shaped
t_{tulip}	s	time of tulip inversion
t_{wall}	s	time when flame front first reaches the pipe wall
U		primitive variables
U_l		primitive variables at left side
U_r		primitive variables at right side
u	m/s	velocity
u_*	m/s	velocity at contact surface
u_{CJ}	m/s	speed of CJ detonation
u_L	m/s	laminar flame speed
u_l	m/s	velocity at left side
u_r	m/s	velocity at right side
u_{sp}	m/s	spontaneous wave speed
u'	m/s	turbulent intensity
V	V	supply voltage
w		number of grid cells in the β flame model
X_{wall}	m	axial flame position when flame front first touches the pipe wall
x	m	position
x_B	m	start position for left running characteristic
x_F	m	flame position
x_{TD}	m	transducer position
x_{tip}	m	position of flame tip
z		number in the Van der Corput sequence

Greek symbols

Symbol	Unit	Description
α		expansion ratio
β		factor in β flame model
Γ_+	m/s	right running characteristic
Γ_-	m/s	left running characteristic
γ		heat capacity ratio
Δ	m	grid cell size
Δp	kPa	pressure difference
Δp_ε	kPa	pressure error value
ΔT	K	temperature difference
Δt	s	time step length
Δx	m	grid cell size in x-direction
Δu	m/s	velocity difference
δ	m	laminar flame thickness
ε	m^2/s^3	dissipation rate of turbulent kinetic energy
ζ		random number
θ		angle of flame front to pipe wall
κ		wave number
\varkappa	m^2/s	mass diffusivity
Λ		constant in β flame model
λ	m^2/s	thermal diffusivity
μ	$\text{kg}/\text{m} \cdot \text{s}$	dynamic viscosity
μ_{eff}	$\text{kg}/\text{m} \cdot \text{s}$	effective dynamic viscosity
μ_L	$\text{kg}/\text{m} \cdot \text{s}$	laminar dynamic viscosity
μ_T	$\text{kg}/\text{m} \cdot \text{s}$	turbulent dynamic viscosity
ν	m^2/s	kinematic viscosity
ν_T	m^2/s	turbulent kinematic viscosity
ξ		pipe wall factor
ρ	kg/m^3	density
ρ_{*l}	kg/m^3	density to the left of contact surface
ρ_{*r}	kg/m^3	density to the right of contact surface
ρ_b	kg/m^3	density in burnt mixture
ρ_l	kg/m^3	density to the left
ρ_r	kg/m^3	density to the right

Symbol	Unit	Description
ρ_u	kg/ m ³	density in unburnt mixture
σ	m/ s	growth rate of instability
τ	s	characteristic time ($r/2\alpha S_L$)
τ_{resp}	s	response time
τ_{wall}	N/ m ²	wall friction
ϕ		equivalence ratio

Subscripts

Symbol	Description
0	ambient conditions
0	initial conditions
B	before flame
b	burnt mixture
d	direction (left or right)
F	flame
f	friction
I	input
i	index number
ig	initial guess
K	Kolmogorov
k	iteration number
L	laminar
l	left
p	constant pressure
QL	quasi laminar
RCM	values from Random Choice Method
r	recovery
r	right
sp	spontaneous
T	turbulent
TD	transducer
u	unburnt mixture
*	contact surface

Abbreviations

Symbol	Description
<i>1D</i>	one dimensional
<i>CCD</i>	charge-coupled device
<i>CFD</i>	computational fluid dynamics
<i>CFLC</i>	Courant-Friedrich-Levy number based on the speed of sound
<i>CFLV</i>	Courant-Friedrich-Levy number based on the flow velocity
<i>CHA</i>	change between iterations
<i>CJ</i>	Chapman-Jouguet
<i>DG</i>	digital group
<i>DDT</i>	deflagration to detonation transition
<i>FA</i>	flame acceleration
<i>FFT</i>	Fast Fourier Transform
<i>FLACS</i>	FLame ACcelerator Simulator
<i>ID</i>	inner diameter
<i>I/O</i>	in and outputs
<i>ISO</i>	International Organization for Standardization
<i>JPDF</i>	Joint probability density function
<i>RCM</i>	Random Choice Method
<i>RGB</i>	colour chart (red, green and blue)
<i>SIF</i>	simple interface flame model
<i>SLIC</i>	simple line interface calculation
<i>SLR</i>	single lens reflex
<i>SWACER</i>	Shock Wave Amplification by Coherent Energy Release
<i>TOL</i>	tolerance value
<i>VOF</i>	volume of fluid

Chapter 1

Introduction

1.1 Background

Gas explosions inside pipes have been studied for more than a hundred years. The studies have been concerned with industrial safety and with a desire to describe general mechanisms of flame propagation. An extensive amount of work has therefore been devoted to understand the phenomena related to flame acceleration (FA) and transition from deflagration to detonation (DDT) in pipes. The first experimental studies on flame propagation in pipes were performed in 1883 by Mallard and Le Chatelier. In 1920 Mason and Wheeler observed flame oscillations in methane-air mixtures. The first photographs of flame propagation in pipes were published by Ellis and Wheeler in 1928. They observed that the shape of the flame was changing during the propagation from being convex towards the unburnt mixture to being concave. Salamandra et al. (1959) called this change of shape a tulip flame inversion. The oscillating flame propagation was confirmed by the schlieren photographs obtained by Schmidt et al. (1952) of combustion waves in propane-air mixtures. In 1956 Markstein presented studies of the interaction between a shock wave and a flame front in a shock-tube. Considerable work on flame propagation in pipes has also been performed by Guenoché (1964). He analyzed the various mechanisms that are significant during the flame propagation in a pipe and the coupling between acoustic oscillations and the flame front.

Increased understanding of the transition to detonation was obtained by the pictures presented by Urtiew and Oppenheim in 1966. The idea of the induction time gradient as the determining parameter for DDT was proposed by Zeldovich et al. in 1970 and by Lee et al. in 1979. Lee et al. (1979) introduced the name SWACER (Shock Wave Amplification by Coherent Energy Release) for the processes taking part during the transition.

In roughly the last thirty years all these theories have been further developed and implemented in numerical models. A large part of the work has also been devoted to defining criteria for FA and DDT. According to Sivashinsky (2002) and Dorofeev (2002) there is at the present time no numerical method or simulation tool that can cover the entire range of phenomena in FA and DDT. These processes include complicated interactions of compressible flow, turbulence and chemical reactions.

In the industry today there is a lot of transport of potentially hazardous materials in pipelines. Combustible mixtures can arise when oxygen is allowed to enter the pipelines, e.g. at mixing joints or when there is an underpressure in the pipe. The combustible mixtures represent a potential risk e.g. when possible ignition sources are present or when the pressure or temperature in the pipe rises above the self-ignition conditions. To achieve a better understanding of the potential for flame initiation and propagation in pipelines, further investigation has to be accomplished. Both experimental and numerical work is necessary to increase our knowledge.

1.1.1 Examples of explosions in industrial pipelines

Incidents with gas explosions inside pipelines have occurred frequently in the process industries and on offshore installations. In this subsection, two recent examples of such incidents in Norway are described.

Hydro Agri Porsgrunn, 1997

On 17 April, 1997 an 800 mm ID pipeline for CO₂ gas connecting an Ammonia Plant with a CO₂ plant at Hydro Agri's production site in Porsgrunn, Norway exploded. Few people were working that Sunday, resulting in no physical injuries. 850 m of the pipeline were destroyed and a large number of windows were blown out in the nearby buildings. A view of the destroyed pipeline is shown in Figure 1.1.

In connection with a shutdown for maintenance, the line was purged with nitrogen. Nevertheless some hydrogen entered the pipeline and after six days the explosive mixture formed was ignited. The ignition source has not been determined but an operator was cutting a bolt on a flange shortly before the explosion. The pipeline was broken at points certain distances apart, and the damage indicated that the gas had detonated (Pande and Tonheim, 2000 and Bjerketvedt et al., 1997).

Sleipner T, 2002

On 9 September, 2002 an ignition in the flare system occurred at Statoil's platform Sleipner T. Splitting a flange on a 14" flare pipe resulted in air penetration into the



Figure 1.1: A view of the pipeline that was destroyed during the incident at Hydro Agri Porsgrunn (Norsk Hydro ASA).

flare system. At the same time, other systems at Sleipner T were depressurized, resulting in large delivery of gas into the flare system. During the depressurization, the gas mixture in the system was too rich to ignite, but when the depressurization was finished and the delivery of gas was reduced it is assumed that the mixture in the flare system became combustible. The mixture was ignited by the flare and the explosion propagated from the flare tip through the pipe to the open flange. A group of four people were working close to the open end. After the ignition, they heard increasing rumbling in the flare system and experienced a strong shaking of the trestle where they were working. When the explosion reached the open end they saw a gleam of light and heard a bang before large amounts of black smoke were flowing out of the flange opening. There were no personal injuries except for some buzzing in the ears after the explosion pressure. No visible damages in the system were recognized and it was assumed that the design pressure was not exceeded during the explosion. The investigation disclosed that the marking of the split flange was wrong, indicating that the pipe was transporting sea water while it then was connected to the flare system. (Bratseth et al., 2002)

1.2 Objective

The objective of this work is to investigate gas explosions inside pipes, and from this establish models for predicting the consequences of accidental gas explosions in

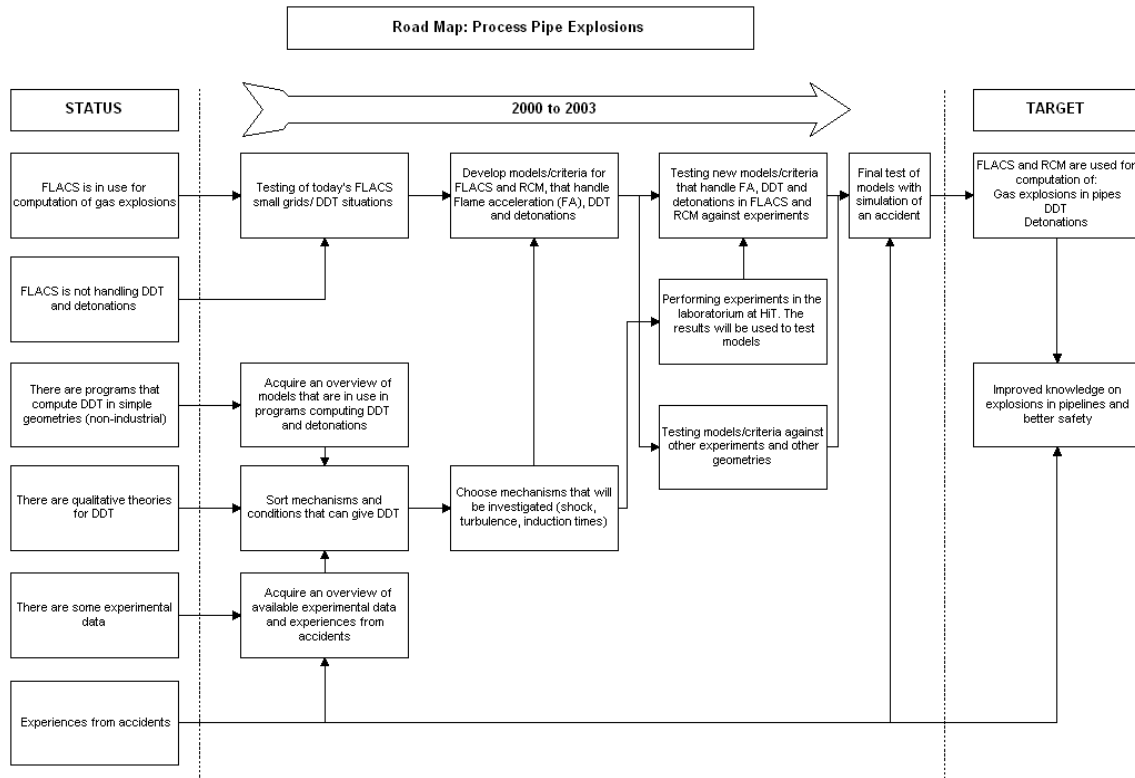


Figure 1.2: Project Road Map

industrial pipelines.

A MATLAB version of the Random Choice Method (RCMLAB) has been developed at Telemark University College. This 1D code, which also includes a combustion model, should be further developed to handle flame propagation in pipes properly. Important issues are burning velocity, boundaries at pipe outlet and friction and heat transfer.

The commercial CFD code FLACS (www.gexcon.com) has mainly been developed for gas explosions in large volumes like offshore modules. It is therefore necessary to test the code for flame propagation in pipes and if possible define parameter values that would make the code able to handle both acoustic oscillations and flame propagation in pipes.

It will also be important to increase the understanding of the mechanisms that control the flame propagation in pipes. Experimental studies and literature reviews will be used and compared to the numerical results.

A Road Map is used in the project management. The final version is shown in Figure 1.2. The main targets are that RCM and FLACS could be used to calculate gas explosions in pipes and to improve the knowledge on gas explosions in pipes. Both FA and DDT are mentioned, but it is also clear that to properly calculate the

DDT process a thorough understanding of the basic mechanisms for FA is necessary. The experimental and numerical work will therefore mostly be concentrated on the propagation of deflagration waves and their interactions with acoustic waves in pipes without obstructions. Only a small part of the work will be devoted to the study of DDT.

1.3 Overview of thesis

A theoretical study of flame propagation and DDT in pipes is given in Chapter 2. This chapter also includes descriptions of models and of some published experimental work. Chapter 3 contains a description of the experimental test facilities and the experimental results obtained. The numerical codes used are discussed in Chapter 4, and the conclusions and recommendations for further work are in Chapter 5.

Chapter 2

Theory on flame propagation in pipes

2.1 Introduction

A flame initiated in a pipeline will undergo flame acceleration (FA) and under certain conditions also transition from deflagration to detonation (DDT). The maximum flame speed reached is determined by mixture properties such as laminar burning velocity and expansion ratio, physical states such as temperature and pressure and the geometrical properties of the pipe such as diameter, inner wall smoothness, length and whether bends, obstructions etc. are present.

The flame propagation can be categorized into different regimes according to the value of the flame speed and to the mechanisms that are working. In this chapter the different regimes from ignition to DDT will be explained and the mechanisms and criteria included in the flame propagation will be discussed. The main focus is on smooth-walled pipes with the ignition point at a closed end.

2.1.1 Propagation regimes

Propagation of a flame front in a pipeline after initiation by an ignition source can result in different propagation regimes, as shown in Figure 2.1. When the combustion process is initiated by a weak ignition source at the closed end of the pipe, its first propagation will be as a smooth laminar flame front governed by the laminar burning velocity and the expansion ratio. The flame speed is increased as the area of this smooth surface is increased when the flame front propagates spherically away from the point of the ignition source. As the flame front hits the rear wall and the side walls, the flame speed is decreased due to the decrease of the flame surface area when the flame

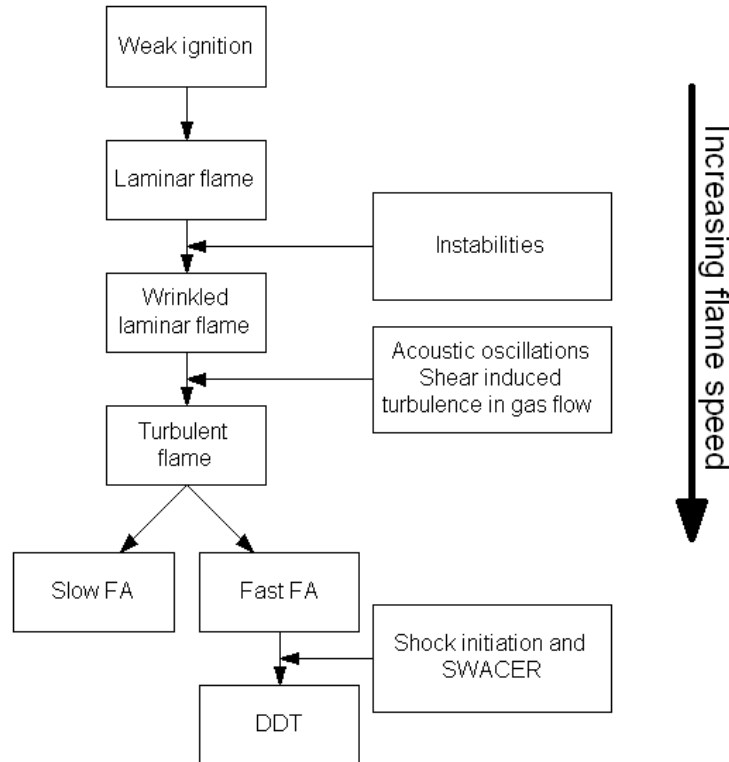


Figure 2.1: Regimes of flame propagation from ignition to DDT (Dorofeev, 2002).

is quenched in the contact areas. The flame front is intrinsically unstable because of the density discontinuity across the front, and during the propagation, instability mechanisms give the flame front a cellular or wrinkled shape. The non-planar flame surface will have an increased surface area, and the flame is accelerated.

Further flame acceleration includes development of a turbulent flame regime. In a pipe, turbulence is mainly generated due to wall effects and by interactions of the flame front with the acoustic waves in the pipe. When bends, tees and area changes are present in the pipe, these will generate more turbulence. Turbulence will increase the overall burning rate by increasing the flame surface area and by increasing the heat and mass diffusion rates. Stretch and curvature effects will however reduce the local burning velocity, and at strong turbulent intensities these effects can quench the flame.

The flame propagation in a deflagration mode can develop further into a detonation. The transition can occur in the turbulent flow field after the pressure wave ahead of the flame or in the turbulent flame brush itself. The pressure waves generated under the flame acceleration enhance the temperature in the unburned gas mixture. An increase in temperature will decrease the ignition delay time. In the turbulent flow field, the temperature distribution is non-homogenous and in some points with the

lowest ignition delay time auto-ignition of the mixture can first occur. New pressure waves are generated when new flame fronts are accelerated from these points, which further increase the temperature and can also merge with the leading pressure wave and strengthen it. These processes continue until the leading pressure wave is strengthened to a shock wave strong enough to initiate and maintain a detonation.

2.2 Ignition sources

The combustion process has to be initiated by an ignition source. In this work only a weak ignition source that initiates a laminar combustion process is considered. In other situations with stronger ignition sources, fast flame propagation or detonation can occur directly from the ignition. In industrial pipelines, the mixtures can be ignited by sparks from welding or other works on the pipelines, by heating of pipe walls etc. In experimental work, the mixtures can be ignited by a spark produced between two electrodes, by a filament or glow plug in the mixture etc.

2.3 Laminar flame propagation

2.3.1 Initial flame propagation

When a flame is initiated in a pipe by a sufficiently small and weak ignition source near the closed end of the pipe, it initially propagates as a sphere outward from the ignition point. The flame acceleration is large due to the relatively large increase of flame surface area of a sphere propagating freely in all directions. If the ignition source is placed close to the rear end wall, the backward propagating flame will very soon reach the end wall. When the flame front hits this wall, it is quenched in the contact area, and the flame will only propagate in the forward direction with a hemispherical shape. In this initial stage, the flame front is smooth and is accelerated due to an increasing surface area. Experiments performed by Kerampran et al. (2001) indicate that the growing flame surface is the only source to the initial flame acceleration. They found that the ratio of the surface area of the flame front to the pipe cross section was in agreement with the ratio between the measured flame speed and the laminar flame speed. As discussed by Guenoché (1964), the hemispherical flame front will change shape to what he calls an increasingly elongated semi-ellipsoid (i.e. finger shaped flame). The axial velocity increases with the flame surface area and becomes much higher than the radial velocity towards the pipe walls. The proximity of the pipe walls prevents expansion of combustion products in the radial direction and it is assumed

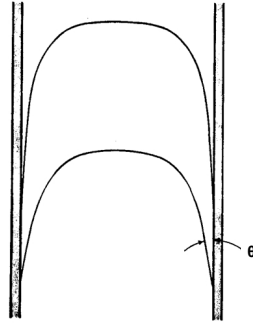


Figure 2.2: The flame front at two positions. The angle θ to the pipe wall is indicated (Guénoche, 1964).

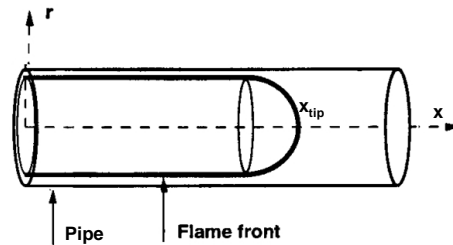


Figure 2.3: Representation of the flame front as a cylinder connected to a hemisphere (Clanet and Searby, 1996).

that the radial velocity is close to the laminar burning velocity. Clanet and Searby (1996) distinguished four stages in the initial propagation of the flame front. The first stage is the hemispherical propagation undisturbed by the pipe walls. In the second stage as the flame is accelerated in the axial direction it takes the mentioned finger shape. This stage lasts until the flame first reaches the pipe walls, and is characterized by an exponential increase of flame propagation and thereby pressure. Because of the very small angle between the flame and the wall as shown in Figure 2.2, the flame front can be presented as a cylinder connected to a hemisphere, as shown in Figure 2.3. The location of the flame tip can then be given by an exponential expression as:

$$\frac{x_{\text{tip}}}{r} = e^{\frac{t - t_{\text{sphere}}}{\tau}} \quad (2.1)$$

where τ is a characteristic growth time: $\tau = \frac{r}{2\alpha S_L}$, r is the pipe radius, x_{tip} is the position of the flame tip, S_L is the laminar burning velocity, α is the expansion ratio,

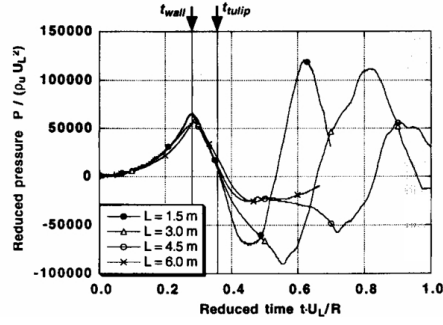


Figure 2.4: Reduced pressure versus reduced time. t_{wall} and t_{tulip} are pointed out (Clanet and Searby, 1996).



Figure 2.5: Photographs of the flame propagation in a closed pipe (Ellis and Wheeler, 1928).

t is the time and t_{sphere} is the time when the flame front changes from spherical to finger shaped. The flame reaches the pipe wall at time t_{wall} , and in experiments t_{wall} coincide closely with the first pressure maximum measured, as shown in Figure 2.4. From experiments Clanet and Searby (1996) have found an empirical model for t_{wall} :

$$t_{\text{wall}} = 0.26 (r/S_L) \pm 0.02 (r/S_L) \quad (2.2)$$

By using t_{wall} as the variable time in Equation 2.1, t_{sphere} is given as:

$$t_{\text{sphere}} = t_{\text{wall}} - \frac{r}{S_L} \frac{1}{2\alpha} \ln \left(\frac{X_{\text{wall}}}{r} \right), \quad (2.3)$$

where X_{wall} is the axial flame position when the flame front first touches the pipe wall. t_{sphere} can also be given as a linear relationship:

$$t_{\text{sphere}} = 0.1 (r/S_L) \pm 0.02 (r/S_L) \quad (2.4)$$

In the third stage, the flame surface area decreases as the flame is quenched when it hits the side walls of the pipe. The flame propagation decreases while the velocity of the propagation of the flame front edge near the pipe walls remains almost constant. Then the inversion to a tulip flame begins. The time when the tulip flame occurs

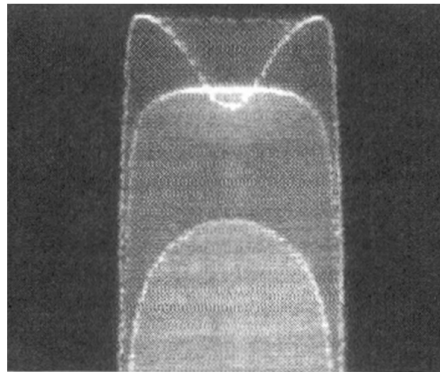


Figure 2.6: The inversion of the flame front. The pictures are taken just before, during and just after the tulip flame inversion (Clanet and Searby, 1996).

can be determined as the time at which the curvature of the flame front changes sign. A linear relationship with the laminar burning velocity and the pipe radius is also empirically developed for t_{tulip} :

$$t_{\text{tulip}} = 0.33 (r/S_L) \pm 0.02 (r/S_L), \quad (2.5)$$

which gives that $t_{\text{tulip}} = 1.29t_{\text{wall}}$. The fourth stage concerns the time after the tulip inversion. In this stage, acoustic oscillations in the pipe can have an effect on the flame propagation.

The tulip flame phenomenon was first observed in the photographic studies of Ellis and Wheeler (1928). An example of their photographs is shown in Figure 2.5. The name tulip flame was introduced by Salamandra et al. (1959). They assumed that during the flame propagation, the pressure before the flame front becomes higher than the pressure behind the front and that the inversion occurs because of a flow in the direction opposite to that of the flame front propagation. The flame inversion was also studied in experiments by Clanet and Searby (1996) as shown in Figure 2.6. They assumed that, except in the boundary layer at the walls, the viscous effects are small compared to inertia effects, because the Reynolds number, defined by the pipe radius and the velocity of the flame tip, is typically of the order 10^5 . The effects of the boundary layer were investigated by igniting two flames beside each other. Images of the flames show a symmetry in the tulip flame formation, which confirms that boundary layers at the wall are not directly involved in the phenomenon. For experiments in different pipe lengths, the tulip inversion occurs at approximately the same time. This indicates that the inversion time is independent of pipe length and acoustic waves in the pipe. Clanet and Searby concluded that the tulip flame inversion is a result of Rayleigh-Taylor instability. This instability mechanism arises at an



Figure 2.7: Example of how the flame front again can become convex towards the unburnt mixture (Guénoche, 1964).

interface between a light fluid and a heavier fluid when this interface is exposed to an acceleration. Pressure and density gradients will then generate instabilities on the fluid interface. The Rayleigh-Taylor instabilities can therefore also occur when the flame propagation is decelerated as the flame surface area is decreased when the flame front reaches the pipe walls. The inversion time was also predicted by the models of Taylor (1950) and Richtmyer (1960), and was found to be in agreement with the experimental results.

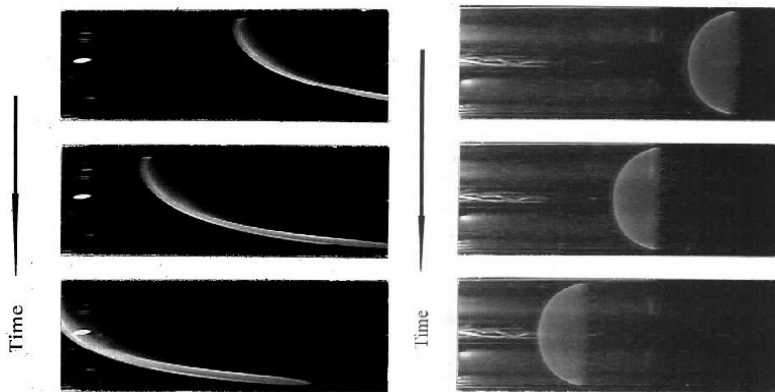


Figure 2.8: Shape of flame front for propagation in a normal gravity field (left) and a microgravity field (right) (Kawakami et al., 1999).

Salamandra et al. (1959) proposed that if the pipe is long enough and there is no influence by acoustic waves on the flame propagation, the flame front can reaccelerate after the deceleration during the flame inversion. The tulip flame has become concave towards the unburnt mixture and the flame front area is therefore increased. This results in an acceleration of the flame front, which would be strongest in the centre of the pipe. In the new acceleration, the flame front can again become convex towards the unburnt mixture, e.g. as shown in Figure 2.7. Then a new inversion process can occur and the flame propagation is decelerated by the same mechanisms as in the first inversion. It is therefore possible (Guénoche, 1964) that the flame propagation can become oscillating due only to its own internal instability mechanisms. In the

reacceleration period, Salamandra et al. (1959) recognized that the shape of the flame front was asymmetrical relative to the pipe walls. Because of the larger density of the unburnt mixture, it is drawn to the lower part of the horizontal pipe by the gravity, while the lighter burnt mixture will rise to the upper part of the pipe, as shown in Figures 2.5 and 2.7. The gravity is therefore causing a larger acceleration in the upper part of the pipe than in the lower. The effect of the gravity on the shape of the flame front has also been studied by Kawakami et al. (1999). They compared flame propagation in a field with normal gravity to a field with microgravity and found that in the microgravity field, the shape of the flame front remains hemispherical, as shown in Figure 2.8.

2.3.2 Flame wrinkling by instability mechanisms

Instabilities will arise during the flame propagation in a pipe. Williams (1985) categorized the instabilities into three categories. Primarily all flames are intrinsically unstable and these instabilities will develop independently of geometrical conditions. Chamber instabilities play a role for flame propagation inside a chamber as a pipe. The last category is system instabilities which occur when processes in other parts of the system interact with the combustion process. Phenomena that can give intrinsic instabilities are e.g. hydrodynamic effects, diffusive-thermal effects and body-force effects. Chamber instabilities in a pipe may be caused by acoustic and shock waves when the flame front interacts with the longitudinal acoustic waves in the pipe or by the influence of the pipe walls on the flame propagation. System instabilities may be associated with pipe outlet conditions or rupture discs for example.

The density of the combustion products is considerably lower than that of the reactants. Temperature increase due to the energy release in the combustion process will give an expansion in the burnt mixture. The expansion ratio is a characteristic parameter for a gas mixture and is defined as the ratio between the densities of the unburnt and burnt mixtures:

$$\alpha = \frac{\rho_u}{\rho_b} \quad (2.6)$$

The gravity effects will generate instabilities on the flame front in situations where a flame is propagating upwards in a vertical pipe. The less dense burnt mixture is below the denser unburnt mixture, and buoyancy effects will influence the flame front. The phenomenon is also called Rayleigh-Taylor instability. These instabilities occurring at a surface between two fluids with different densities in a gravitational field were first studied by Lord Rayleigh in the second part of the nineteenth century.

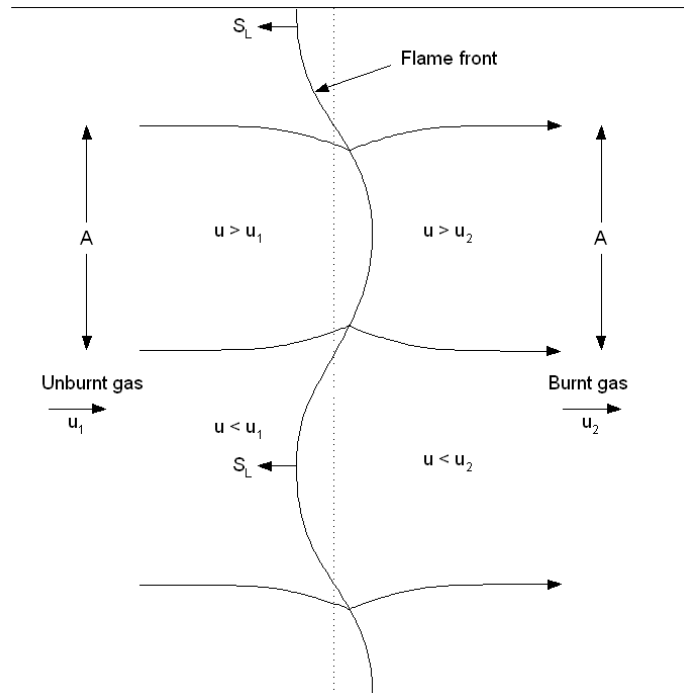


Figure 2.9: Deviation in flow lines leading to the Darrieus-Landau instabilities (Clanet and Searby, 1998).

The same instability mechanisms were also studied by Taylor (1950) in a situation with accelerating fluids. When a flame is accelerated, the lighter burnt mixture is accelerating the unburnt mixture and the same mechanisms which appear in a gravitational field will make the flame front instable.

The expansion ratio through the flame due to the heat release is, as already mentioned, the reason for the inherent instability of a flame front. The mechanisms of this hydrodynamic instability were first recognized by G. Darrieus in 1938 and L. Landau in 1944 (Clanet and Searby, 1998). As shown in Figure 2.9, the expansion ratio gives a deviation of the streamlines through a perturbed flame front with a deviation towards the normal to the flame front of the downstream streamlines. In Figure 2.9, the flame front is stationary and the unburnt mixture is flowing to the flame front. A perturbation with an upstream flame displacement must therefore have a curvature convex towards the unburnt gas mixture. The continuity principle requires then a decreased flow velocity because of the increased flame front area due to the convex curvature and the displacement will tend to move even farther upstream. A downstream flame displacement results in a contradiction of the streamlines and the area is decreased. Then the flow velocity is increased and the flame front displacement moves farther downstream. Landau found a model for the growth rate of this instability:

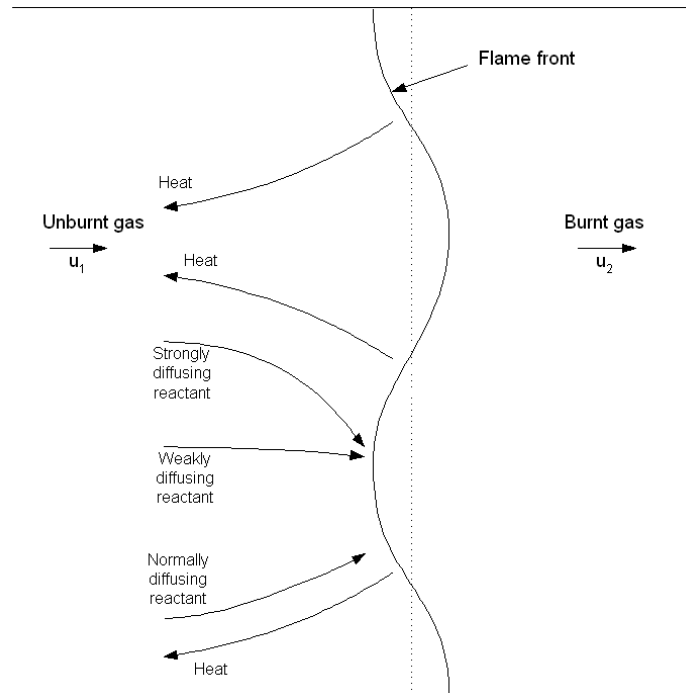


Figure 2.10: The mechanism of thermal-diffusive instability (Williams, 1985).

$$\sigma = \kappa S_L f(\alpha), \quad (2.7)$$

where κ is the wave number of the perturbation, $f(\alpha)$ is a positive function of order unity vanishing for $\alpha = 1$ and α is the expansion ratio. Dorofeev (2002) stated that in situations with no flow obstacles, FA are mainly due to Landau-Darrieus instabilities, and that the effect of this mechanism is often limited to slow FA. For flame propagation in pipes, the flame front propagates as a hemisphere and the initial area increase delays the onset of Landau-Darrieus instabilities. The pipe walls will also reduce the time available for growth of the instability. Non-accelerating curved flames in pipes could therefore represent a steady propagation. Williams (1985) mentions however that in absence of other phenomena there is a possibility that the Landau-Darrieus instability leads to turbulence.

The wavelengths of the unstable flame front will range from the size of the pipe diameter to the shortest wavelengths governed by thermal diffusion. As shown by Equation 2.7, the growth rate of the instability is inversely proportional to the wavelength and perturbations at small wavelengths will grow more rapidly than perturbations at larger wavelengths. As the wavelength approaches the thickness of the flame, thermal and diffusive effects within the flame will influence the flame propagation. These effects stabilize the perturbations when the wavelength is below a

critical wavelength. The growth rate has a maximum value at this wavelength and will decrease for smaller wavelengths and can become negative at a smaller critical wavelength (Williams, 1985). The mechanisms of the thermal-diffusive instability is shown in Figure 2.10. A perturbation in the upstream direction will appear as a local consumer of reactants and a local source of heat. If the Lewis number (Le) equals unity, i.e. that the thermal diffusivity equals the diffusivity of the deficient reactant, the flame temperature T_f will remain unchanged. If $Le > 1$, i.e. the thermal diffusivity is larger, T_f decreases, and if $Le < 1$, i.e. the diffusivity of the deficient reactant is larger, T_f increases. In the situation where T_f increases, the local flame speed increases and the perturbation grows in the upstream direction. The thermal-diffusive instabilities are therefore rising for $Le < 1$. On the other hand, the thermal-diffusive effects stabilize the Landau-Darrieus instability for $Le > 1$. A simpler mechanism of the thermal-diffusive stabilization effect is proposed for $Le = 1$ (Williams, 1985). In this mechanism, it is assumed that the temperature is constant on the flame front and in the burnt mixture. For a perturbation in the downstream direction in Figure 2.10 the unburnt mixture is surrounded by hot burnt gas and the heating rate will become greater than for a plane flame front. When the temperature is increased, the flame is accelerated and the perturbation tends to become more planar. For an upstream perturbation, the temperature is decreased because of heat loss and the flame speed is decreased. Thermal diffusivity can therefore have a stabilizing effect when $Le = 1$.

The effect of flame stretch on the burning velocity can be expressed by the Markstein number (Ma) or length. The Markstein number is given as the ratio between the Markstein length and the laminar flame thickness. The wrinkling of a flame front is increased at negative Markstein numbers and the flame acceleration can be significantly greater than for positive values of Ma (Bradley et al., 2001). When Ma is negative, the thermal-diffusive effects will not be able to withstand the Landau-Darrieus instability mechanisms and the thermal-diffusive instability can even contribute to the destabilizing of the flame front (Bradley, 1999). Negative values of Ma can be favoured by high pressures and when the deficient reactant is the more diffusive ($Le < 1$). Conversely, when Ma is positive, the thermal-diffusive effects will stabilize the Landau-Darrieus instabilities.

2.4 Turbulent flame propagation

When the flame propagation becomes turbulent, the FA is further increased. Turbulence will corrugate the flame front and increase the total flame surface area, and the local transport of mass and energy will increase. The local burning velocity is changed

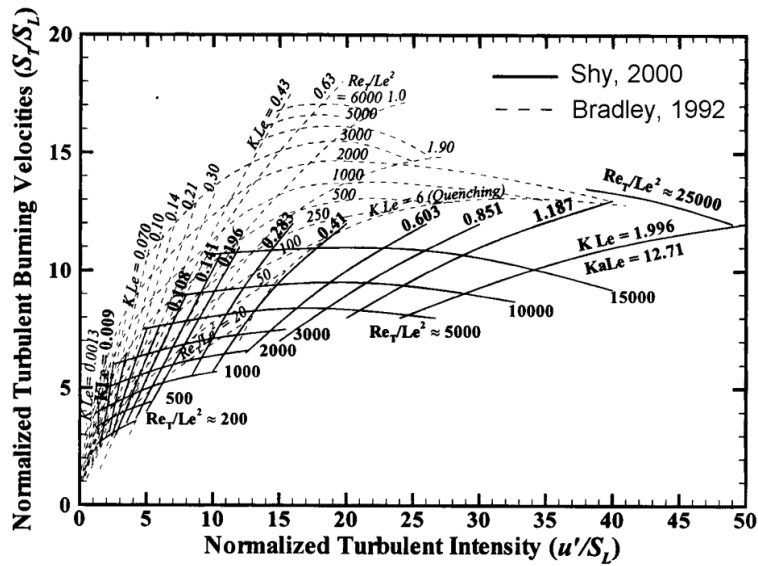


Figure 2.11: Normalized turbulent burning velocities versus normalized turbulent intensity (Shy et al., 2000). Data obtained by Bradley (1992) and Shy et al. (2000). The numbers used are the turbulent Reynolds number (Re), the Karlovitz number (Ka or K), and the Lewis number (Le).

due to the effects of curvature and stretch on the flame front. Shy et al. (2000) achieved turbulent burning velocities up to an order of 10 times the laminar burning velocity for methane and propane. Further increases in the turbulent intensity result in local quenching of the flame, which will reduce the FA. These results are around a factor 2 smaller than the results reported by Bradley (1992b). In Figure 2.11, the two sets of results are compared. The experiments are performed along iso-curves of the groups $KaLe$ and Re_T/Le^2 , where Ka is the Karlovitz number, Le is the Lewis number and Re_T is the turbulent Reynolds number. During inversions of the flame front the increased stretch rate can be related to flame extinction by a vortex, as observed in the experiments by Mueller et al. (1996).

The flame behaviour can be divided into different regimes as shown by the Borghi diagram in Figure 2.12. The diagram describes u'/S_L , which is the turbulent intensity normalized by the laminar burning velocity, versus l_T/δ , which is the integral length scale normalized by the laminar flame thickness. For $Re_T < 1$ and when $u' < S_L$, laminar flame propagation is observed. The turbulent domain is divided into three regimes denoted by the Karlovitz number, Ka , which is defined as the ratio between the time scale of the chemical reaction and the Kolmogorov time scale, $Ka = t_F/t_K$, and the Damköhler number, Da , which is defined as the ratio between the integral time scale and the time scale of the chemical reaction $Da = t_T/t_F$.

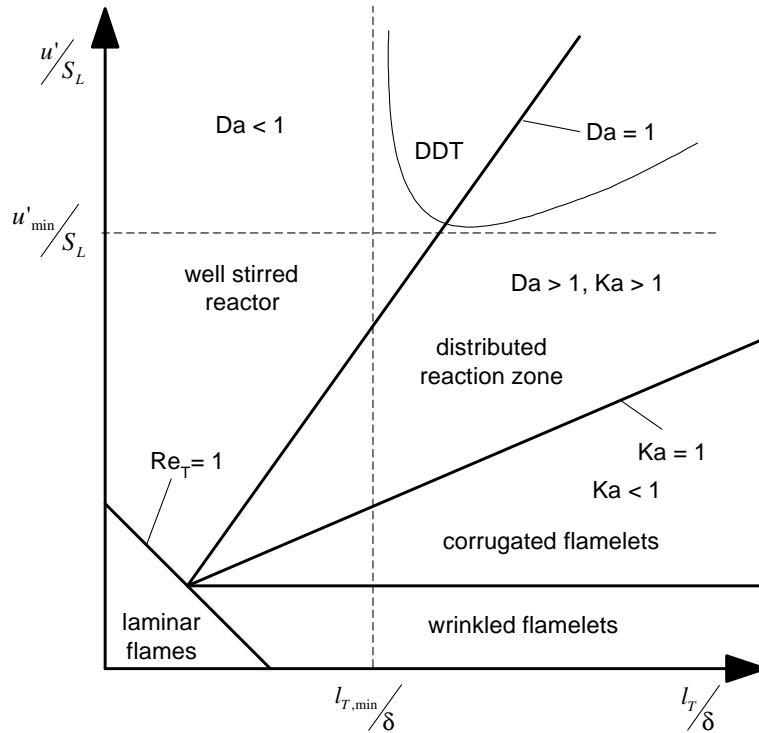


Figure 2.12: The Borghi diagram (He, 2000).

Above the line $Da = 1$, the regime can be described as an ideally stirred reactor. In this regime, the Kolmogorov eddies are smaller than the inner layer of the reaction zone. Almost all of the turbulent eddies are then embedded in the reaction zone. The two regimes considered when a turbulent flame is propagating in a pipe are the corrugated flamelets and the distributed reaction zone. In the corrugated flamelet regime where $Ka < 1$, the time scale of the chemical reaction is smaller than the Kolmogorov time scale, $t_F < t_K$. Then the whole flame is embedded within eddies at Kolmogorov scale, and the flame structure is therefore not perturbed by turbulent fluctuations, so the flame is said to be locally laminar (Warnatz et al., 1999). However, the flame area increases due to the turbulent wrinkling of the flame front. In the distributed reaction zone, $t_F > t_K$ and eddies at small scales can enter into the flame structure and disturb its structure.

Dorofeev (2002) categorized the FA in a turbulent regime through a branching point (Figure 2.1), where according to mixture properties and boundary conditions the acceleration can be either weak or strong. Weak acceleration results in a slow subsonic turbulent flame, while strong acceleration results in a fast supersonic turbulent flame. In the latter regime, the combustion wave consists of a leading shock followed by a turbulent flame brush. The burning rate is controlled by the transport of energy and species typical for deflagrations. Transition to detonation can only occur in this fast

propagation regime.

For flames propagating in pipes, turbulence is mainly generated due to wall effects and by pressure waves propagating in the pipe. When bends, tees and area changes are presented in the pipe, these will increase the turbulence. There could also be an extent of self-turbulisation due to instability mechanisms.

Interaction of both the pressure waves and the flame with the walls could generate turbulence. This turbulence is generated by shear forces acting in the wall boundary layer. Schmidt et al. (1952) explained the occurrence of a turbulent flame regime with the generation of turbulence in the unburnt mixture ahead of the flame as the pressure waves interact with the wall. Jones and Thomas (1991) proposed that the shear induced turbulence would only become important for FA after a rapid acceleration had started due to turbulence generated by interaction of the flame front with the pressure waves in the pipe.

When a flame front is accelerated or decelerated, pressure waves are generated that propagate outward from the front at the speed of sound (Chu, 1952). In the initial FA, a compression wave is generated that propagates toward the open end of the pipe. When this compression wave reaches the open end it is reflected in the opening as a rarefaction wave that propagates backwards in the pipe. Acoustic oscillations will then occur in the pipe. The amplitude of these acoustic oscillations is determined by the heat release in the combustion and their nature depends on the boundary conditions at the open end.

The interaction between a flame and a rarefaction wave has recently been studied by Laviolette et al. (2003). The experiments are performed in a shock-tube where the flame is ignited in the high pressure region at the diaphragm between the two regions. When the diaphragm is ruptured, a rarefaction wave reaches the flame front in the burnt mixture. Schlieren photographs of the shock tube are shown in Figure 2.13. The flame is propagating hemispherical as in the two first frames before the flame front is overtaken by the rarefaction wave between the second and third frame. The radius of the hemisphere is reduced and in frame four and five a funnel of unburnt mixture propagates into the burnt mixture. A secondary instability is formed at the tip of the funnel in frame five. The creation of a funnel indicates that the Richtmyer-Meshkov instability mechanism plays a role in the interaction between a flame front and a rarefaction wave. This instability mechanism is characterized by the formation of a funnel when the propagation speed of a density discontinuity is suddenly changed as when it is hit by a pressure wave (Richtmyer, 1960). The occurrence of the Richtmyer-Meshkov instability in the interaction of a shock wave with the flame front has been shown in the classical experiments by Markstein (1956). After a short backward propagation of

the flame front, the flame acceleration is further increased due to the increased flame surface area after the significant distortion of the flame front after the interaction with the rarefaction wave. A transition to a turbulent propagation regime can often occur. This increased FA after an interaction with a rarefaction wave can promote DDT (Laviolette et al., 2003). The rarefaction wave can create the necessary gradients in temperature and concentration for DDT to occur, but the rate of heat release must exceed the rate of cooling in the rarefaction wave.

In experiments by Sobesiak et al. (2003), the occurrence of several flame inversions were observed. They found that the number of inversions was reduced with increasing laminar burning velocity and that the number increased with the reduction of the area of the open end. The inversion of the flame front was described by the mechanism of tulip flame formation. Different instability mechanisms should however be responsible for the first inversions and the rest of the inversions. In the first inversions, tulip flame formation occurs when the flame speed is reduced as the flame surface area is reduced when part of the flame front reaches the pipe wall and is quenched. Clanet and Searby (1996) explained this inversion as a result of the Rayleigh-Taylor instability. During the other inversions, the flame front is probably interacting with pressure waves and the flame inversion should occur due to Richtmyer-Meshkov instabilities.

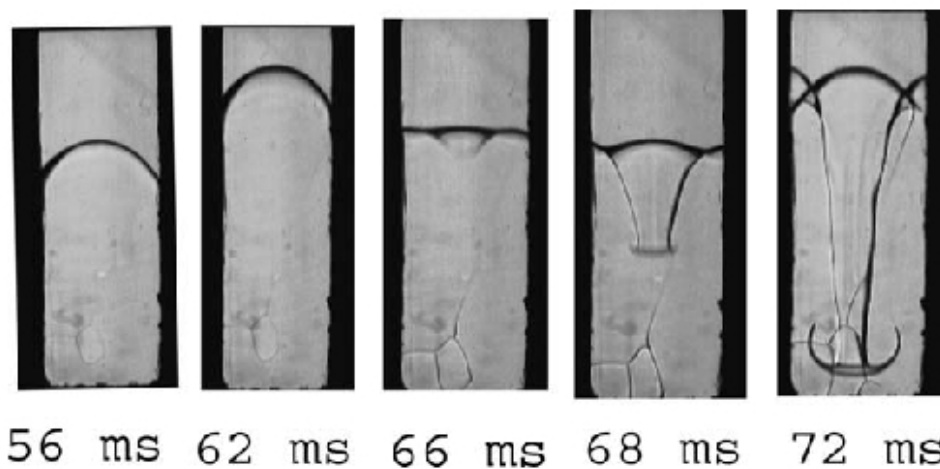


Figure 2.13: Interaction of a hemispherical flame front with a rarefaction wave (Laviolette et al., 2003).

Flame inversions can therefore occur by two mechanisms: i) by quenching the flame front at the pipe wall and ii) by interaction with the pressure waves in the pipe. Depending on the pipe length and diameter, and on mixture reactivity, one or more of both inversions can occur. For short pipes, even the first flame inversion is influenced by the rarefaction waves generated at the pipe outlet, but for all pipe

lengths above a critical value the first flame inversion is only due to quenching at the pipe wall. The critical pipe length is found to be between 0.72 - 1.22 m for a circular pipe of 22 ID (Kerampran et al., 2001) and between 2.1 - 2.6 m for a square pipe with a hydraulic diameter of 45 mm (Kerampran et al., 2000). The critical pipe length is inversely proportional to the mixture reactivity and proportional to the pipe diameter. When the flame speed is reduced after the first maximum value, a rarefaction wave is generated and a system of longitudinal acoustic oscillations will arise in the pipe. Depending on the wave length of the oscillations, which is determined by the pipe length, more inversions will occur either due to quenching at the pipe wall or due to interaction with these acoustic oscillations. The number of inversions due to quenching at the pipe wall increases with the wave length for a specific mixture concentration and pipe diameter.

2.5 Criteria for FA

A criterion for FA can be stated by the expansion ratio α . The effect of the expansion ratio on the flame acceleration is studied by Dorofeev et al. (2001b) and Kuznetsov et al. (1999, 2002). A critical expansion ratio can be defined, and for expansion ratios above this value there can be a strong FA as shown by the branching point in Figure 2.1. Below this value the flame speed would remain slow. The critical ratio has been shown to depend on the mixture composition and on effective dimensionless activation energy. Kuznetsov et al. (2002) found this critical expansion ratio to be $\alpha = 5.5$ for mixtures of hydrocarbon fuels in obstructed pipes. For hydrogen-air mixtures the critical ratio was found by Kuznetsov et al. (1999) to be $\alpha = 3.25 \pm 0.25$.

For expansion ratios above the critical value, the diameter of the pipe should be at least two orders of magnitude larger than the laminar flame thickness for strong FA to be possible (Kuznetsov et al., 1999). This criteria can be expressed by the dimensionless ratio:

$$l_T/\delta \approx D/\delta > 10^2, \quad (2.8)$$

where l_T is the integral length scale of turbulence, δ is the laminar flame thickness and D is the pipe diameter.

2.6 Modeling of flame propagation

The complexity of the phenomena involved in FA and DDT makes it difficult to include the whole range of phenomena in one model. There are mainly two approaches to the modeling of flame propagation. For the first type, as in Eddy break-up models for example, turbulent combustion is described by the reactive Navier-Stokes equations. In the other approach, the flame front is regarded as a reacting discontinuity and the reaction progress is determined by the turbulent burning velocity. In the following subsection, modeling of the turbulent burning velocity is briefly described.

2.6.1 Models for turbulent burning velocity

The turbulent burning velocity is used as an input to flame models and the effects of turbulence on the flame propagation can be incorporated by using models for the turbulent burning velocity. Considerable research has been devoted to understanding and achieving good models for the turbulent burning velocity. Today the two main approaches are by joint probability density function (JPDF) transport equations and by laminar flamelets.

The first flamelet model was presented by Damköhler (1947). He divided the effect of turbulence into two regimes, defined by the laminar flame thickness, and concluded that turbulence will always enhance the burning velocity. For the large scale turbulence, with turbulent scales larger than the laminar flame thickness, the burning velocity increases due to an enlarged flame area by wrinkling of the flame front. In the small scale regime, he assumed that turbulence increases the transport process of molecules and heat. Damköhler assumed that the large scale turbulence is almost always the controlling regime, and when the laminar burning velocity is unaffected by the turbulence an expression for the turbulent burning velocity can be written on the basis that mass flowing through the pipe will be the same as that passing through the wrinkled flame. This is expressed by the turbulent burning velocity, S_T , for the cross-sectional area, A , and by the laminar burning velocity, S_L , for the wrinkled flame area, A_T :

$$\rho S_T A = \rho S_L A_T, \quad (2.9)$$

where the density, ρ , in the unburnt mixture is assumed constant. The ratio between turbulent and laminar burning velocity is then:

$$\frac{S_T}{S_L} = \frac{A_T}{A} \quad (2.10)$$

When the area ratio is taken as $A_T/A = 1 + u'/S_L$, where u' is the turbulent

intensity, the turbulent burning velocity can be described as:

$$S_T = S_L \left(\frac{A_T}{A} \right) = S_L \left(1 + \frac{u'}{S_L} \right) = S_L + u' \quad (2.11)$$

The flamelet models for turbulent burning velocity can be divided into two categories, where the first one gives the velocity as a function of flame wrinkling only. The wrinkling is then determined by the turbulent intensity. This is true only for small Karlovitz numbers, where the stretch rate is small. In the second category, the effects of stretch and curvature on the burning velocity have been taken into account. These effects have often been called Lewis or Markstein effects. The expression proposed by Damköhler is in the first group.

More extended summaries of modeling of the turbulent burning velocity are presented by Peters (2000) and Bradley (1992a and 2002) for example.

2.7 Experimental work on flame propagation in pipes

There has been a growing interest in flame propagation in smooth pipes in recent years. In this section, some examples of experimental work that have recently been published are presented together with the classical experiments of Schmidt et al. (1952).

Flame propagation in smooth pipes

In the last years, some experimental work on flame propagation in smooth pipes have been performed at Université de Poitiers in France. Results are presented by Kerampran et al. (1999, 2000 and 2001) and Veyssi re et al. (2002 and 2003).

The experiments are performed in three set-ups: 1) a 21 mm ID circular pipe of plexiglass with a length varying from 0.72 to 2.72 m; 2) a 40 × 40 mm square cross section steel pipe, equipped with glass windows, with a length varying from 0.6 to 8.1 m and 3) a 100 mm ID circular steel pipe of length 26 m. In all the experiments, the gas mixture is ignited at the closed end by a heated wire. The other end is open, such that the flame can propagate freely. Measurements are obtained by a high-speed video camera, photocells and by piezoelectric pressure transducers disposed at the closed end and at other locations along the pipe. The fuels used are propane, ethylene and acetylene.

The effects of pipe length and mixture reactivity have been studied. Comparisons of the propagation at different pipe diameters are not made, but it is concluded that the effects of changing the pipe length are only moderately dependent on the cross section area, which indicates that mainly longitudinal acoustic waves are affecting the

flame propagation. The first pressure maximum is independent of pipe lengths above a minimal length, which was observed to be between 0.72 and 1.22 m in the 21 mm ID pipe. The pressure waves generated by the flame will initiate acoustic oscillations in the pipe. For gas mixtures with low flame speeds such as propane-air mixtures, these oscillations will give an oscillating flame propagation. In long pipes, the flame can remain oscillating around a certain length some distance out in the pipe, and may be quenched. Generally for low burning velocities, the average flame speed in the pipe, calculated as the pipe length divided by the retention time of the flame in the pipe, will be nearly independent of the pipe length because of the oscillating flame propagation. The average flame speed will however have some variations according to the point on the oscillating wave that the flame reaches the open end, i.e. in an accelerating or a decelerating phase. For more reactive mixtures, the flame propagation is less affected by the oscillating pressures and no reversal of the flame propagating is observed. For these mixtures, the average flame speed is dependent on the pipe length because the flame accelerates nearly continuously towards the open end.

Flame propagation in industrial scale piping

Experiments with flame propagation in industrial scale piping have been performed by Chatrathi et al. (2001). Three different pipe diameters were used, 6", 10" and 16", and three different fuels, propane, ethylene and hydrogen, in air were studied. The effects on the flame speed of gas composition, pipe diameter, fuel type and pipe geometry (bends) were tested. In addition, the DDT distances and the pressure development were recorded.

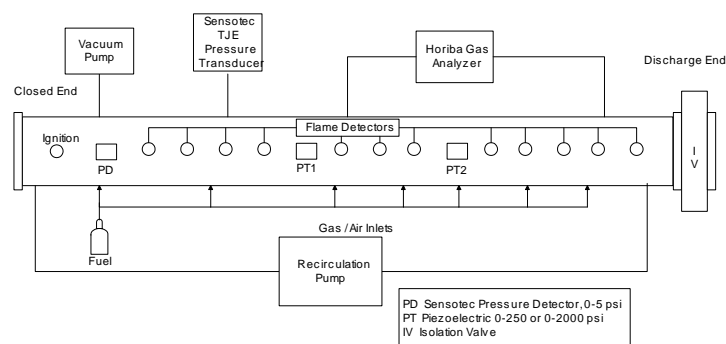


Figure 2.14: Schematic description of the experimental set-up to Chatrathi et al. (2001).

The experimental set-up is shown in Figure 2.14. This configuration was used for all three pipe diameters, but in the 6" piping system observations in three configurations

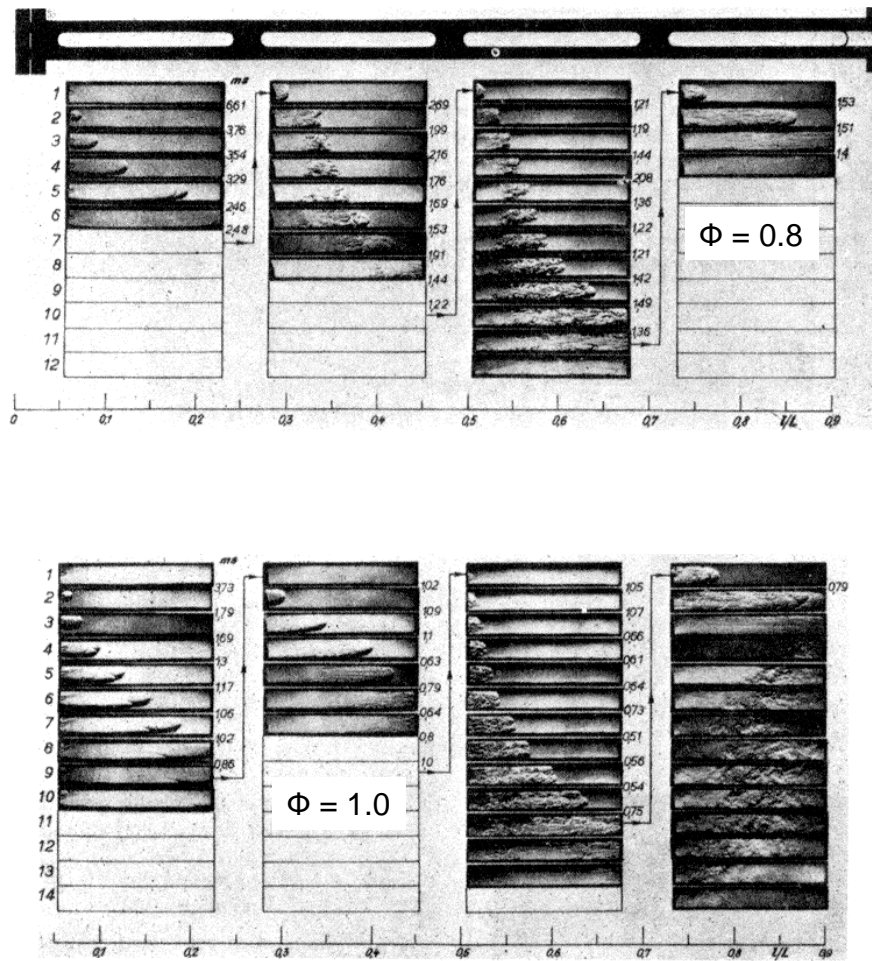


Figure 2.15: Shlieren photographs of the flame in propane-air mixtures at equivalence ratios of 0.8 and 1.0 (Schmidt et al., 1952). The flame is propagating from a closed towards an open pipe end.

with a single 90° elbow placed at distances of 6.1 m, 12.2 m and 18.3 m from the closed end were conducted as well. The length of the pipe was varied to obtain a length to diameter ratio (L/D) of approximately 98 in all three systems. The pipes were closed at the end near the ignition source and equipped with an isolation valve at the other end. The valve was closed during evacuation and filling and opened prior to ignition. To detect the arrival of the flame front, 12 Texas Instrument TSL250 optical sensors, placed at various distances along the pipe were used. The pressure was measured by two PCB piezoelectric pressure transducers and one Sensotec pressure detector. For data acquisition, a Nicolet Odyssey was used that could sample 16 channels at a rate of 100 kHz.

To determine the effect of composition on flame speed, experiments were performed at different equivalence ratios for the three fuels in the 6" pipe. For propane and ethylene in the near-stoichiometric range, the flame speed experienced a large acceleration to sonic velocities. At concentrations farther from the stoichiometric condition the acceleration became smaller until the flame was quenched. In the cases with hydrogen, detonations were observed for equivalence ratios between 0.79 - 1.59.

In general, the effect of pipe diameter on flame speed is that the flame speed will rise as the diameter increases. Testing was conducted for stoichiometric fuel-air mixtures in the three pipe sizes. Up to a L/D of about 50, the flame speed is not significantly affected by the diameter, but for longer distances the flame speed will increase more rapidly in the larger pipe diameters.

Flame and Schlieren photographs of combustion waves in pipes

Some considerable experiments were performed by Schmidt et al. (1952). They intended to describe the influence of turbulent motion of the gas on the burning velocity. The experiments were performed with a steel pipe of 24×24 mm² inner cross section and a length of 1.09 m. Flame propagation was recorded by Schlieren photographs and with photographs of the light from the flame itself. For Schlieren photographs, the pipe had four windows on each side, each 195 mm long and covering the whole width of the pipe, and for photographs of the light from the flame there were windows only on one side. The glass was thick enough to withstand explosion pressures up to 10^4 kPa. Photographs were taken at rates up to 25000 frames per second, and the distance of the pictures on the film together with the film velocity gave the time distance. The experiments had three different set-ups with one end open and ignition at the open or the closed end and with both ends closed, and they were performed at different equivalence ratios of propane-air mixtures. The results for flames ignited at the closed end and propagating towards the open end are shown in Figure 2.15 for equivalence ratios of 0.8 and 1.0. Different flame propagations were observed for the three set-ups. In the case with ignition at the open end, the flame first propagates at a steady speed, but after a while the turbulence generation is great enough to accelerate the flame before it again is slowed down near the closed end. When the flame is ignited at the closed end, the flame will first slow down, but when the rarefaction wave from the open end reaches the flame and draws it to the open end the flame speed is increased. In a pipe closed at both ends, the flame speed will decrease towards the closed end.

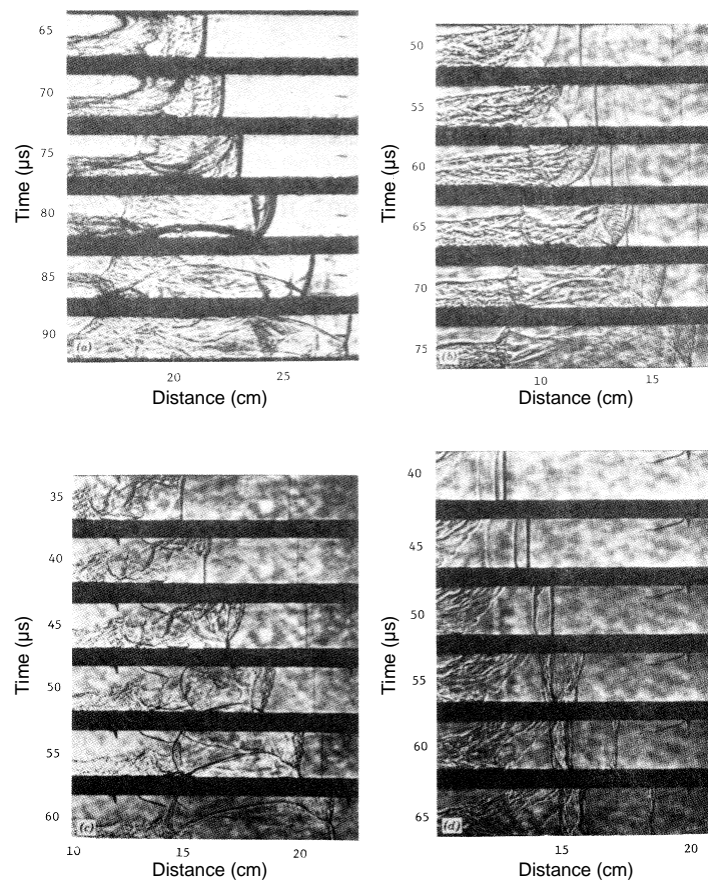


Figure 2.16: Various locations of transition to detonation observed in $2H_2 + O_2$ mixtures: (a) onset between flame and shock, (b) onset at flame front, (c) onset at shock front, (d) onset at a contact discontinuity (Kuo, 1986, after Urtiew and Oppenheim, 1966).

2.8 DDT

When a fast turbulent deflagration regime is achieved, a transition to detonation can occur. In this section, the mechanisms and criteria comprised in the transition process are discussed. In the CJ-theory, the detonation wave is treated as a discontinuity with infinite reaction rate. Based on this one dimensional theory, it is possible to calculate detonation velocity, pressure etc., if the gas mixture is known. As a continuation of the previous section, this section is opened with a summary of some experimental work before mechanisms, criteria and models for DDT are discussed briefly. Since most FA mechanisms are very effective in confined pipes, acceleration of the flame to speeds sufficient to cause the onset of detonation can be expected, provided that the pipe is long enough. Long pipes or channels represent one of the most hazardous configurations for DDT (Moen, 1993).

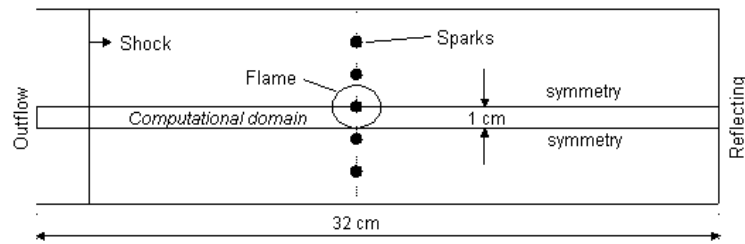


Figure 2.17: Schematic description of shock tube with several spherical flames. A computational domain is stated (Thomas et al., 1997).

2.8.1 Experimental studies of DDT

Some classical experiments on DDT in pipes were performed by Urtiew and Oppenheim (1966), in which the onset of detonations were recorded on stroboscopic laser-schlieren photographs. Premixed $2H_2 + O_2$ mixtures were used in a 1 m long pipe with cross section $1'' \times 1.5''$. They observed local explosions that initiated DDT at four different locations, as shown in Figure 2.16. The locations were defined as:

1. Local explosion between flame and shock front.
2. Local explosion at the flame front.
3. Local explosion at the shock front.
4. Local explosion at a contact discontinuity.

The existence of the different locations depends on the particular pattern of the shock wave. The generation of this pattern depends again on minute inhomogeneities in its development, and therefore the transition to detonation is nonreproducible in its detailed development (Kuo, 1986).

The situation with DDT after shock-flame interactions is observed experimentally by Thomas et al. (1997). The experiments are performed in a shock tube, where several spherical laminar flames are ignited simultaneously, as shown in Figure 2.17. When the incident shock reaches the flames it will interact with the flame fronts. The shock wave travels through the flames and is reflected at the other end. The reflected wave again interacts with the flames and after the reflected shock has travelled a distance in the left direction from the flame fronts, a detonation was initiated. The shock-flame interactions produced flame instabilities, which resulted in hot spots with gradients in induction time. When the conditions were appropriate, supersonic spontaneous waves occurred, and these transitioned to detonations.

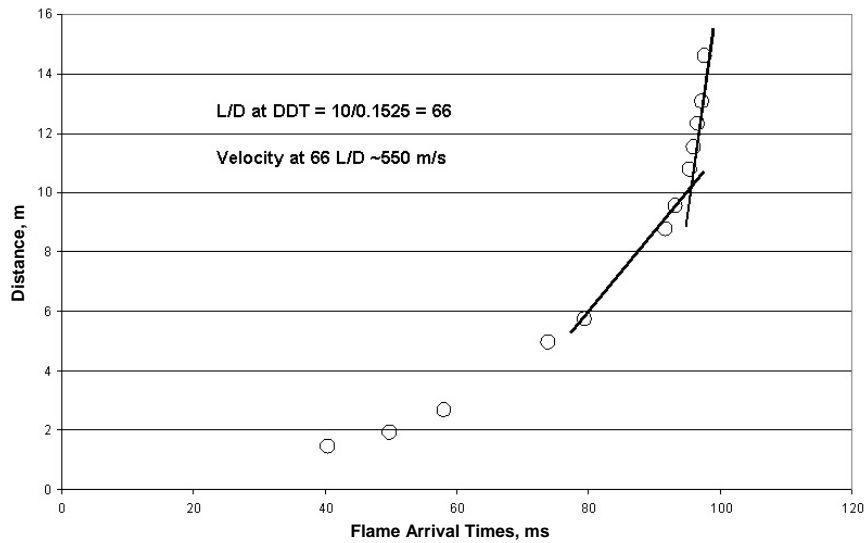


Figure 2.18: Demonstration of the determination of the L/D ratio at DDT. 6" pipe, 6.5% ethylene (Chatrathi et al., 2001).

Table 2.1: Run-up distance for DDT obtained by Chatrathi et al. (2001).

Pipe diameter	Length/Diameter		
	Propane	Ethylene	Hydrogen
6"	72	66	59
10"	71	69	59

DDT was also experienced in some of the experiments to Chatrathi et al. (1996) described in Section 2.7 and determination of a run-up distance was necessary. They have described a method where the values of the length to diameter ratio $(L/D)_{DDT}$ was approached by plotting distances versus flame arrival times to graphically determining the point. Figure 2.18 shows this approach used for the 6" pipe and 6.5% ethylene, which resulted in a DDT distance of about 10 m or L/D of 66. The velocity is then about 550 m/s. More values for L/D ratios are given in Table 2.1.

The effects of fuel and pipe diameter on the run-up distance $(L/D)_{DDT}$ are shown in Figure 2.19. The diagram is presented by Chatrathi and Going (1996) from the experimental work performed by Bartknecht (1981) and Steen and Schampel (1983). The run-up distance $(L/D)_{DDT}$ for transition is inversely proportional to the pipe diameter.

Experiments with DDT in smooth pipes have recently been presented by Kuznetsov et al. (2003). The experiments are performed with stoichiometric $H_2 - O_2$ mixtures in a 24 m long pipe of 105 mm ID. The initial pressure is varied from 20 to 800 kPa,

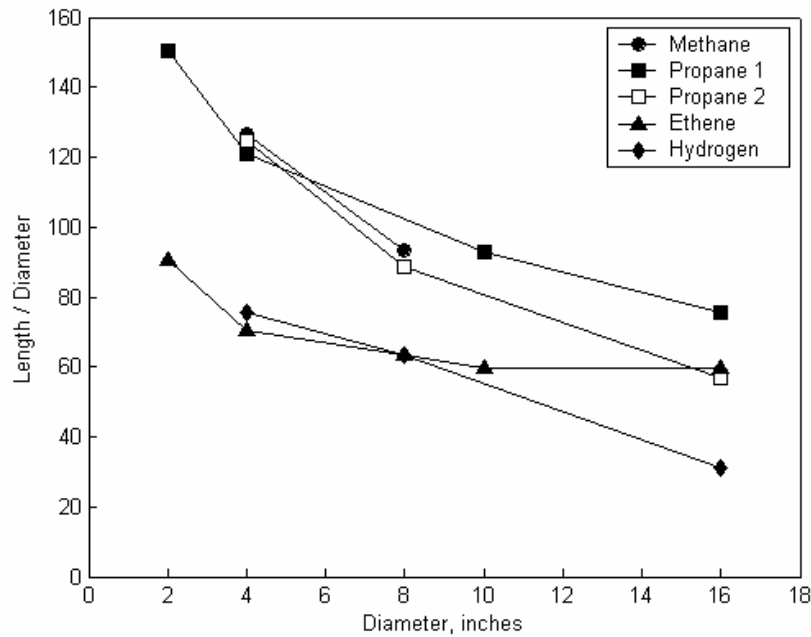


Figure 2.19: The effect of pipe diameter on the L/D ratio at the deflagration to detonation transition distance, for different fuels (Chatrathi and Going, 1996).

which gives a variation in the detonation cell size from 8.5 mm to 0.17 mm. The pipe is made long enough to avoid effects from pressure waves reflected at the end wall on the flame propagation. A glow plug is used for ignition because a spark plug could directly initiate a detonation. Flame propagation and pressure waves were recorded by photodiodes and pressure transducers. A photodiode was placed axial to the pipe to record the light signal continuously. The transition could then be recognized as an inflection on the signal curve. Just before the transition, the flame speed had values of about 800 m/s to 1000 m/s. The overdriven detonations had speeds up to 4000 m/s and the detonation speed decreased to the CJ value of 2760 m/s to 2960 m/s at about 1 m from the transition point. The run-up distance to DDT was found to decrease with initial pressure:

$$L_{\text{DDT}} \sim \frac{1}{p^{1.17}} \quad (2.12)$$

The only important parameter that was varied in the experiments at the various initial pressures was found to be the ratio of the integral length scale of turbulence to the flame thickness. When the pipe diameter was held constant in these experiments it was found that the run-up distance for DDT was proportional to the flame thickness. It was concluded that the flame propagation has to reach a specific flame speed for DDT to occur and that the ability of a mixture to accelerate the flame to this speed

is an important parameter in the DDT process.

2.8.2 Mechanisms involved in DDT

Many phenomena can be involved in DDT, but both experiments and numerical calculations indicate that the underlying mechanism is the generation of an induction time gradient. This gradient is associated with gradients in temperature and concentration. The significance of the formation of an induction time gradient for DDT was first proposed by Zeldovich et al. (1970) and Lee et al. (1979). Lee et al. (1979) generated gradients in the concentration of free radicals by exposing a combustible mixture to ultraviolet radiation. The reaction was initiated in the gas layer with the largest concentration of free radicals and therefore with the shortest induction time. From the experiments, they proposed a mechanism for DDT that was called SWACER (Shock Wave Amplification by Coherent Energy Release). The mechanism can be formulated:

1. The gas layer having the shortest induction time is ignited first.
2. The shock wave generated by this primary explosion propagates to the next layer, which has a slightly longer ignition delay.
3. The shock wave reduces the induction time of this layer and an explosion is initiated. The energy released in the explosion strengthens the shock wave, that propagates to the following layers where the same process takes place. The induction time gradient provides therefore a method of coherent energy release that strengthens the shock wave up to a detonation.

Bartenev and Gelfand (2000) described some limitation of the SWACER mechanism. The mechanism is comprised of a set of elementary processes which would not be quite correct when there is continuous distribution of induction time. The ignition could also occur without the formation of shock waves, and during the amplification, the structure of the flow and the reaction wave are changed such that the same scheme of interactions should not be used in the whole process.

Thomas (1999) divided the transition process into four phases, as illustrated in Figure 2.20:

1. Initial shock-flame complex. A leading shock (S) and a turbulent flame (R) propagate together. Energy release here may lead to a slight acceleration of the leading shock (A).
2. Local explosion leading to transition to detonation (DDT).

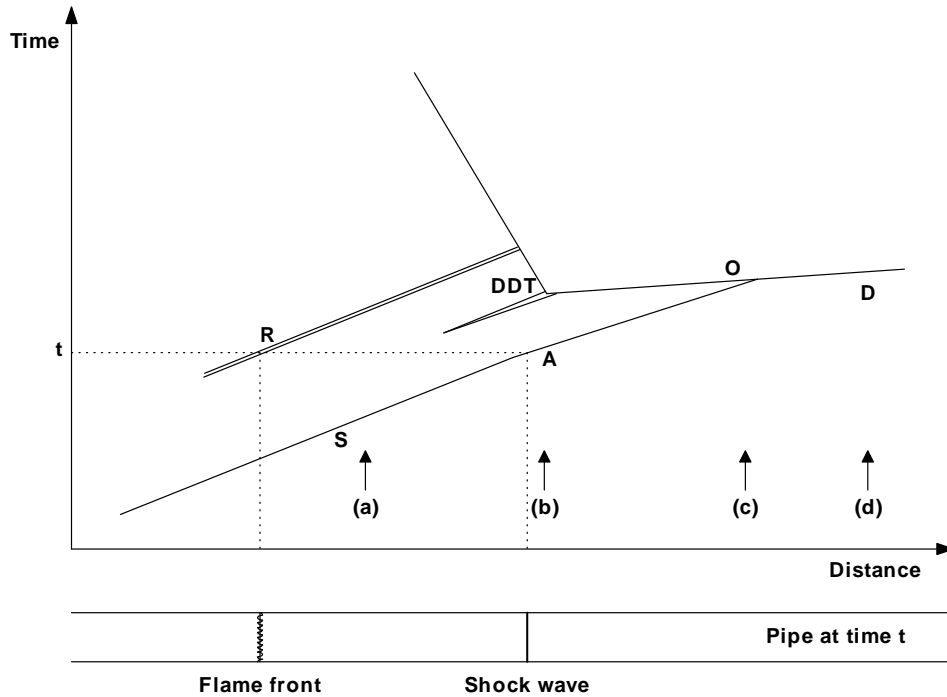


Figure 2.20: General phases observed during a transition to detonation event following turbulent acceleration (Thomas, 1999).

3. An overdriven detonation (O).
4. Steady state detonation (D).

Typical pressure histories associated with the transition process are shown in Figure 2.21, as indicated in Figure 2.20. At the first location (a) the pressure will rise when the shock passes and then survive through the deflagration-zone. At location (b) the pressure will first rise when the shock passes and then rise significantly in the DDT-zone. At location (c) the detonation has caught up with the primary shock, and at (d) the detonation has stabilized on the value of a CJ detonation.

Zeldovich (1980) distinguished four modes of propagation for a combustion wave. By comparing the spontaneous flame speed, u_{sp} , defined as the inverse of the induction time gradient, to the speed of a CJ detonation u_{CJ} , these four modes were defined as:

1. $u_{sp} > u_{CJ}$, propagation of a weak detonation wave, but no shock front is formed. At the limit $u_{sp} \rightarrow \infty$ a constant volume explosion will occur.
2. $u_{sp} \leq u_{CJ}$, combustion of some parts of the mixture results in a shock wave and a detonation wave could be formed.
3. $u_L < u_{sp} \leq c < u_{CJ}$, propagation of a deflagration wave. c is the speed of sound in the unburnt mixture and u_L is the laminar flame speed.

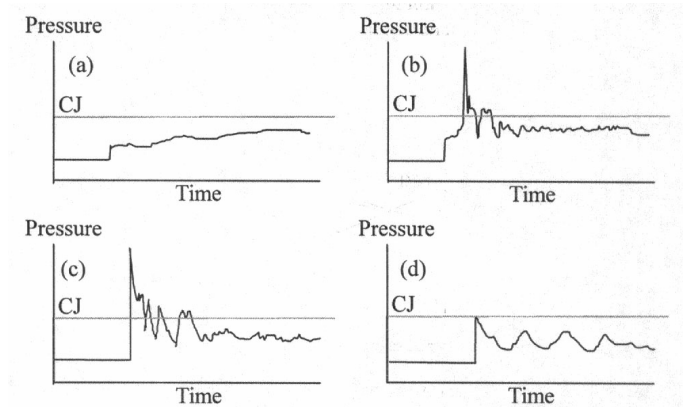


Figure 2.21: Typical pressure histories expected at locations (a)-(d) in Figure 2.20 (Thomas, 1999).

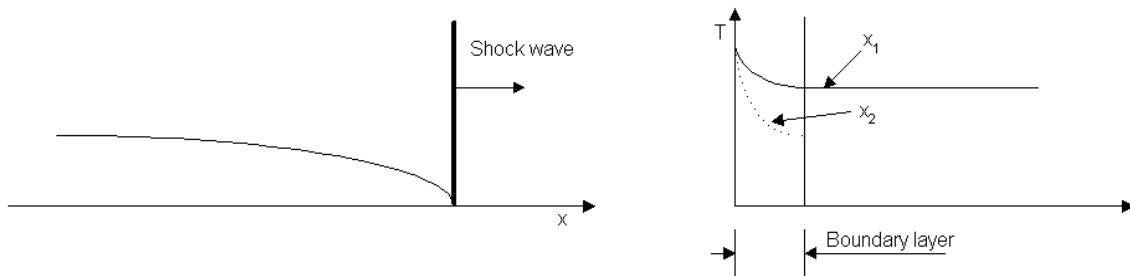


Figure 2.22: Formation of a temperature gradient in the boundary layer along a wall (Bartenev and Gelfand, 2000).

4. $u_{sp} < u_L$, laminar flame propagation which is controlled by heat conduction and diffusion.

Formation of spatial non-uniformities

Bartenev and Gelfand (2000) have given several examples on the formation of spatial non-uniformities or hot-spots with low induction times. Cases which are important for flame propagation in pipes are presented here. In Figure 2.22, it is shown how temperature gradients form due to a boundary layer along the wall after a shock wave for example. Figure 2.23 shows the distribution of pressure and temperature between the flame front and the shock wave generated by the flame. Combustion fronts propagating in long pipes will give a rise of pressure and temperature, as shown in Figure 2.24. During the process of compression of fresh mixture, its temperature can reach the level of self-ignition.

As proposed by Khokhlov et al. (1997) the mechanism for preparing a non-uniformity may differ in different situations. The gradient in induction time may be created by turbulence, a shock wave, photo-irradiation, intrinsic flame instabilities,

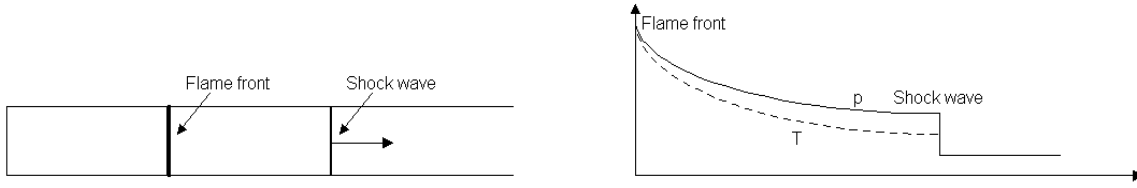


Figure 2.23: Formation of a temperature gradient between a shock wave and flame front (Bartenev and Gelfand, 2000).

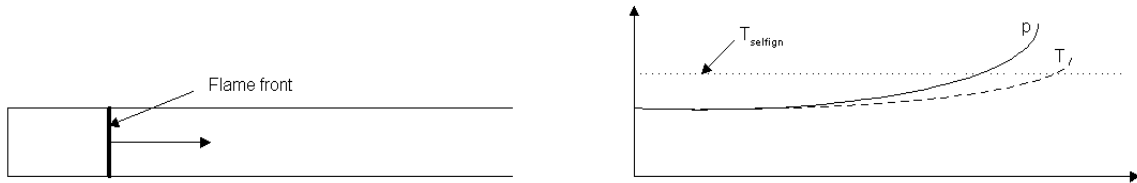


Figure 2.24: Formation of temperature and pressure gradients ahead of a flame front. T_{selfign} is the self-ignition temperature (Bartenev and Gelfand, 2000).

rarefaction waves or a combination of several of these.

2.8.3 Criteria for DDT

It is difficult to determine whether or not DDT will occur in a specific case. A set of necessary criteria for DDT is established to estimate if a transition can occur. These criteria are not sufficient to determine that a transition will occur, but if at least one of them is not satisfied a detonation should not be expected. For flame propagation in pipes, the transition should follow a fast FA. The α criterion described for FA is therefore also a necessary condition for DDT. The transition can occur above some critical flame speeds, which is observed to be between 500 m/s and 800 m/s (Moen, 1993).

Experiments performed in obstructed pipes (e.g. Peraldi et al., 1986) have resulted in a criterion based on the detonation cell size. For pipes with obstructions, the size of the unobstructed passage should be larger than the size of one detonation cell. This criterion has also been extended to smooth walled pipes, and states that the pipe diameter should be larger than one detonation cell.

When the criteria for strong FA is met, a sufficiently long run-up distance is necessary for development of DDT. It is shown by Veser et al. (2002) that the minimum run-up distance for pipes with obstructions is inversely proportional to the ratio of the laminar burning velocity to the sound speed of the combustion products, S_L/c_b .

Critical size of the spatial non-uniformities

The process of DDT can be separated into two phases. First, the pressure wave must steepen into a shock, and this shock must accelerate the combustion wave so that a shock-reaction complex forms. Second, this shock-reaction complex must survive the propagation down the temperature gradient. Two limits can be defined. When the size of the hot-spot is below the first limit, the shock-reaction complex does not form. When the size is above this limit, a shock-reaction complex can successfully form, and when the size is above the second limit, the shock-reaction complex also survives and propagates as a detonation wave into the unburnt mixture.

Numerical simulations, performed by Khokhlov et al. (1997), show that the second limit is sensitive to the initial temperature. An increase in initial temperature will decrease this limit. This can be explained if the criterion for the detonation formation is not the creation, but rather the survival of the shock-reaction complex. For higher initial temperatures, the post-shock induction time is less sensitive to variations of background conditions and so it is easier for the shock-reaction complex to adjust to changing conditions.

Criterion on strength of turbulence

He (2000) proposed that DDT is possible only in the upper part of the Borghi diagram, as shown in Figure 2.12. There exists a minimum turbulent intensity and a minimum turbulent length scale below which DDT cannot occur. A typical minimum turbulent velocity should be in the order of 500 m/s.

As indicated in Figure 2.23, a detonation can be initiated ahead of the flamefront by a shock wave driven by the flame front. Possible effects of shock waves are temperature increase and creation of vorticity. The increased temperature may facilitate the survival of the shock-reaction complex and the vorticity reduces the amount of turbulence that must be created by the primary source (Khokhlov et al., 1997). Assuming that the flame front behind the shock wave is a CJ deflagration wave, the intensity of the shock wave can be determined in terms of the flame front velocity (Chu, 1952). When the shock is sufficiently strong to heat the unburnt mixture to a temperature higher than a critical value, transition to detonation can occur. Such a shock wave can only be produced at turbulent burning velocities above a critical value.

2.8.4 Models for DDT

There have been numerous calculations on the SWACER mechanism. In these calculations it is usually assumed that the formation of an induction time gradient appears

spontaneously. Particularly in situations with turbulent mixing, where the formation occurs by a variety of mechanisms, the assumption of spontaneous formation will not be true. One of the most promising numerical results has been obtained by Khokhlov et al. (1997, 1999a, 1999b, 2001).

Khokhlov et al. (1999) studied the difficult problem of shock-flame interactions. The experimental results of the same problem, obtained by Thomas et al. (1997), are described in subsection 2.8.1. The shock-flame interaction will result in Meshkov-Richtmyer instability as described in subsection 2.4 and the flame distortion produced by this instability will result in Kelvin-Helmholtz instability. The instabilities increase the flame surface area and the flame speed and provide the sufficient conditions for DDT. A very high resolution of the domain is used in the calculations making it possible to resolve the instabilities and to estimate DDT from the basic principles of the reactive flow. The multidimensional, time-dependent, reactive Navier-Stokes equations were solved during the calculations, and a simplified single-step Arrhenius model was used to calculate 1D flame and detonation properties.

Chapter 3

Experiments

3.1 Experimental details

Experiments were performed to enhance the understanding of the phenomena that occur during flame propagation in a pipe. The experimental data are used to validate the numerical models and are used as input to the methods for estimating the quasi 1D burning velocity and the outlet conditions in the RCMLAB code.

Two types of pipes have been used in the experiments. Seamless circular steel pipes of 22.3 mm ID and lengths of 1, 2, 5 and 11 m were used in experiments with propane, acetylene and hydrogen. A 1.9 m long circular plexiglass pipe of 40 mm ID was used in experiments with propane. In addition, shock tube experiments with air were performed in the 22.3 mm ID pipe to test the transducer response.

3.1.1 Pipes

Steel pipes

In these experiments, 3/4" circular seamless smooth steel pipes have been used. The inner diameter is therefore 22.3 mm and the wall thickness is 2.3 mm. The pipes are delivered in lengths of 6 m and are cut into the pipe lengths of 1, 2 and 5 m. The dimensions of the pipes are shown in Figure 3.1.

In the closed end of the pipes, the gas flow is controlled by a hand valve. The ignition electrodes are mounted on this valve to get as near as possible to the closed end of the pipe. The valve is closed just prior to the ignition.

Four pressure transducers and four photodiodes are located along the pipe. The apertures used are of 3 mm for the transducers and of 2 mm for the photodiodes. The location points are 100 mm, $0.382 \times$ pipe length and $0.7 \times$ pipe length from the closed end, and 100 mm from the open end. Acoustic oscillations will occur in

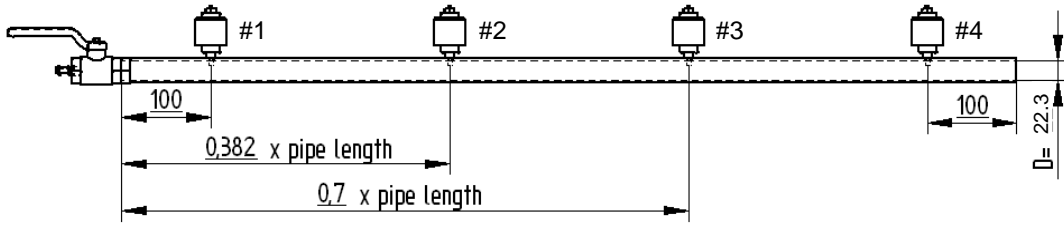


Figure 3.1: The circular steel pipes used in the experiments. Pipe lengths of 1, 2, 5 and 11 m are used. Lengths are given in mm.

the pipe with wave lengths determined by the pipe length. If the measure points are evenly distributed along the pipe their positions can become proportional to the wave lengths. The location of the second measure point is therefore determined from the principle of the golden profile. The pipe is divided into two parts by this measure point, and the length of the longest part is given by:

$$\text{long part} = \frac{\text{pipe length}}{1.618} = 0.618 \times \text{pipe length}. \quad (3.1)$$

The location of the second measure point is then:

$$x_2 = (1 - 0.618) \times \text{pipe length} = 0.382 \times \text{pipe length}. \quad (3.2)$$

Plexiglass pipe

Experiments are performed in a circular plexiglass pipe of a total length of 2 m. The pipe has an inner diameter of 40 mm and a wall thickness of 5 mm. The two ignition electrodes are placed 100 mm from one end of the pipe, which means that 1.9 m of the pipe is used in the flame propagation experiments. The four pressure transducer positions are at 100 mm, 710 mm, 1319 mm and 1785 mm from the ignition source. The fuel-air mixtures are carried to the pipe through a plastic tube mounted on the pipe wall as shown in Figure 3.2. A piston cylinder is placed at the left end of the pipe. The diameter of the piston is adjusted to fit the inner diameter of the pipe, and can therefore propagate back and forth in the pipe. Leakage of gas and pressure through the small gap between the piston and the pipe wall is assumed to be negligible. The piston is alternated between two positions. During gas filling, the piston is in the rear position where it makes the rear closed pipe end. Before the gas mixture is ignited, the piston is moved up to the electrodes, as shown in Figure 3.2, ensuring that the flame is only propagating in one direction. The piston cylinder is controlled by a pneumatic

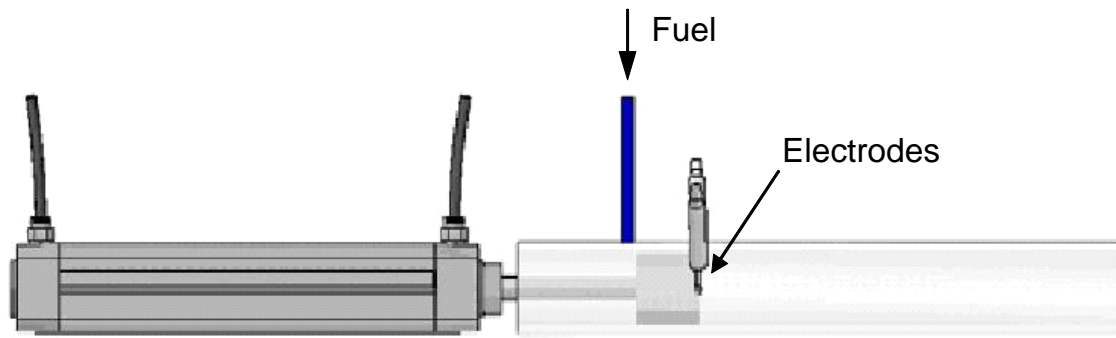


Figure 3.2: Piston cylinder and plexiglass pipe with the ignition electrodes and the gas inlet tube.

system.

3.1.2 Ignition system

The gas mixtures are ignited by generation of a spark between two electrodes that are placed in the centre at the closed end of the pipe. The distance between the two electrodes where the spark is generated is around 2 mm. The two electrodes are connected to a transformer where the supply voltage of around 220 V is transformed to a high voltage current of around 14000 V, as shown in Figure 3.3. The circuit to the transformer is closed by a relay controlled by a hand switch. The relay closes the circuit in 30 ms. An example of the spark is given in Figure 3.4.

A trigger signal to the acquisition system is induced by a capacitor, which is formed by twisting an insulated wire once around the wire from the high-voltage side of the transformer. A voltage divider is connected to this secondary circuit to avoid damage to the trigger board by too high voltage on the trigger signal.

3.1.3 Gas handling system

Three types of gases are used: propane, acetylene and hydrogen. To produce combustible gas mixtures, these gases are mixed with air. Compressed air is supplied from a compressor in the laboratory and commercial grade propane, acetylene and hydrogen from gas cylinders. The compressed air is carried through a filter to remove any oil following the gas flow. The composition of the gas mixtures was controlled by rotameters, one for the compressed air and one for the fuel gas. The same rotameter was used for the three fuel gases. The rotameters were calibrated with the same flowmeter,

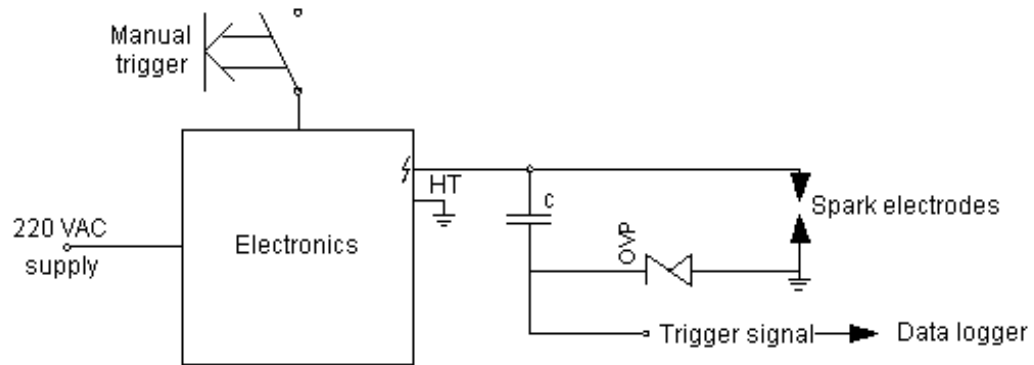


Figure 3.3: System for ignition of gas mixture and generation of a trigger signal to the logging system. c is the capacitor.



Figure 3.4: The spark produced between the two electrodes.

ensuring that the relative relation between fuel and air is known. For propane and hydrogen, the inlet pressure to the rotameter was 2 bar both for fuel and air, and for acetylene 1.5 bar was used both for fuel and air. After coupling the two flows with compressed air and fuel, the gas mixture is transported in a tube approximately 10 m long, in which the mixture should undergo satisfactory mixing so that a homogenous mixture enters the pipe.

3.1.4 Diagnostic systems

Four types of diagnostic systems were used. Kistler pressure transducers were used to measure the pressure, photodiodes were used to capture the flame front propagation and in the plexiglass pipe a reflex camera and high speed camera were used to analyze the flame behaviour in the pipe.

Pressure diagnostics

The pressure is measured with Kistler transducers 7261 and 603B, which are shown in Figure 3.5. In each experiment, four transducers are located along the pipe. Kistler 7261 has a measuring range of -1 to 10 barg and is therefore used in the experiments with propane and with less reactive hydrogen mixtures. The frequency of the 7261 is 13 kHz when the transducer is directly in contact with the pressurized volume and 0.35 kHz when the transducer is coupled to the pressurized volume by a thin tube. The natural frequency of the 603B is 400 kHz. In small diameter circular pipes, the size of the apertures used for mounting the transducers are of importance because apertures that are too large will act as obstructions in the pipe. To avoid any disturbances of the gas flow and the flame propagation, small apertures of 3 mm diameter are used. These small apertures will however be at the sacrifice of the recording frequency, and a test of the pressure rise time has been performed, which is described in Section 3.2. The dimensions of the mountings are given in Figure 3.6 for Kistler 7261 and in Figure 3.7 for Kistler 603B. The openings are only 1.5 mm. For 7261, this thin channel is 15.3 mm long before the gas enters into the measuring volume inside the adapter. The channel for 603B is 7 mm and there is also a small volume inside the nut. The charge signal of the transducers is transformed into a proportional voltage signal in Kistler 5011 charge amplifiers.



Figure 3.5: Kistler 603B, $D = 5.5$ mm (left) and 7261, $D = 35$ mm (right), (Kistler Instrument Corp.).

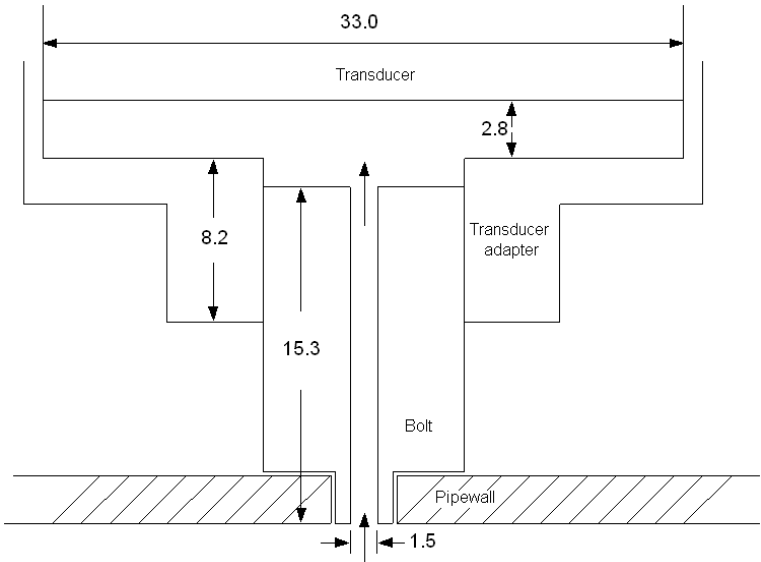


Figure 3.6: Dimensions for the mounting of Kistler 7261 to the pipe. Dimensions are given in mm.

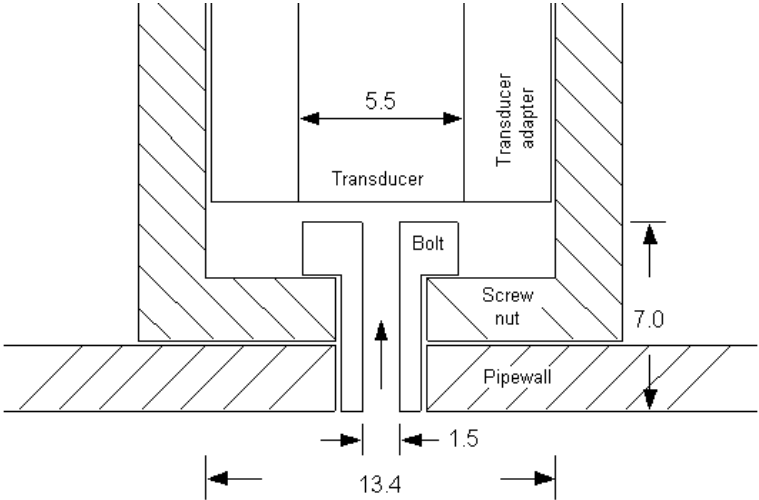


Figure 3.7: Dimensions for the mounting of Kistler 603B to the pipe. Dimensions are given in mm.

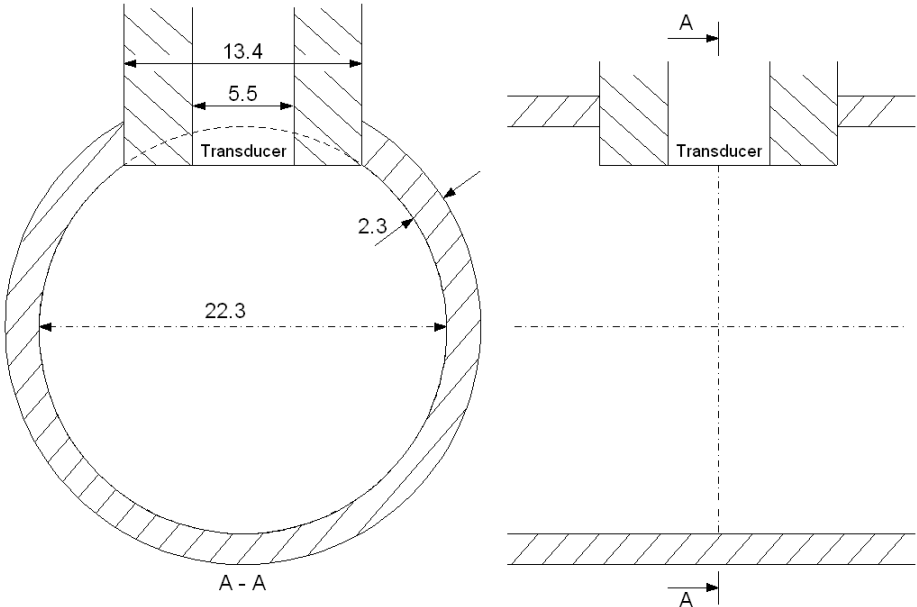


Figure 3.8: The pipe cross section at the placements of Kistler 603B transducers. Dimensions are given in mm.

Experiments are also performed where 603B transducers in adapters are mounted directly in the pipe wall. The adapters have an external diameter of 13.4 mm and can be considered as obstructions in the pipes. The cross section at the placements of the transducers are shown in Figure 3.8. This mounting of the transducers was only used in the 5 m steel pipe where the transducers were located at 100 mm, 1910 mm, 3500 mm and 4900 mm from the ignition point.

Flame front tracking

Texas Instrument TSL250 optical sensors were used to detect the arrival of the flame front. The TSL250 is a light-to-voltage optical sensor combining a photodiode and an amplifier, as shown in Figure 3.9. The output voltage is directly proportional to the light intensity on the photodiode. A supply voltage of approximately 5 V from the NI 6110 sampling board is used in all experiments. This gives a maximum output voltage of around 3.6 V, as shown in Figure 3.10c. The input resistance, R_I , is also delivered by the NI 6110 sampling board. The spectral responsivity is between 300 and 1100 nm, with a peak response at around 800 nm, as shown in Figure 3.10b. The rise time of the output pulse is 360 μ s. The mechanical data for TSL250 are given in Figure 3.11.

Photographic system

Flame propagation was captured by a Fujifilm Finepix S2 Pro digital SLR camera (Single Lens Reflex). This camera has a maximum shutter speed of 1/4000 s and a Super CCD sensor with 6.17 million effective pixels. The sensitivity is equivalent to ISO 100, 160, 200, 400, 800 or 1600. To capture the propagation history of an explosion, pictures were taken with open shutter and medium sensitivity (ISO 200 -

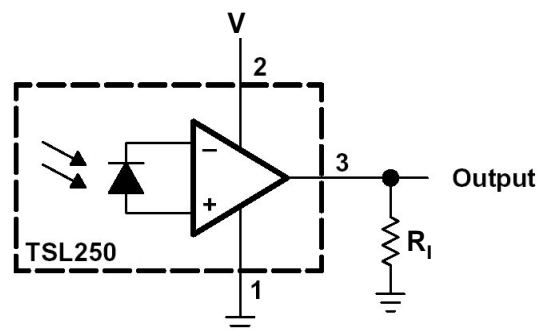


Figure 3.9: The optical sensor TSL250 consists of a photodiode and an amplifier. V is the supply voltage and R_I is the input resistance (Texas Instruments Inc, 1995).

400). To capture instant pictures of the flame front a high shutter speed and high sensitivity (ISO 800 - 1600) were used. The wide-angle lens Sigma EX 20 mm/f 1.8 DG was used in connection with the camera.

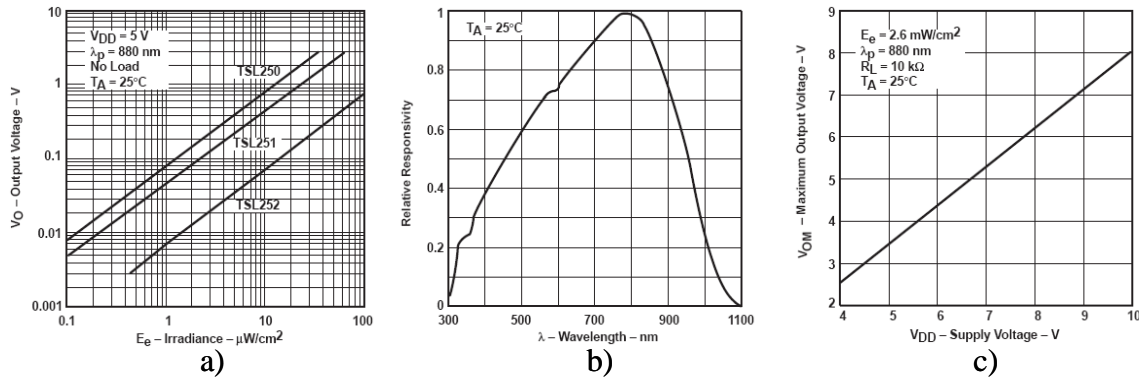


Figure 3.10: Data for TSL250, a) output voltage versus irradiance, b) spectral responsivity versus wavelength and c) maximum output voltage versus supply voltage (Texas Instruments Inc, 1995).

High-speed camera

High-speed digital video film was obtained with a Photron Fastcam APX 120K high-speed camera. Pictures were recorded at frame rates of 1000 fps and 2000 fps in black and white and at a resolution of 1024 by 1024 pixels. The camera has a capacity of 120000 fps, but at a lower resolution. The camera has a light-sensitivity of around one million $17.5\ \mu\text{m}$ pixels. The camera was controlled via a PC and images were downloaded to the PC.

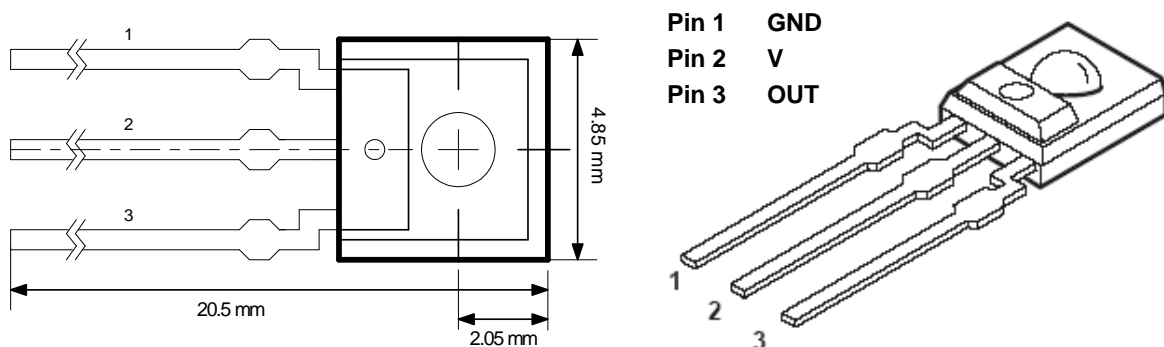


Figure 3.11: Mechanical data for TSL250 (Texas Instruments Inc, 1995).

3.1.5 Data acquisition system

In this subsection, the system used to record the signals from the pressure transducers and the optical sensors are described. The system consists of a 700 MHz P3 PC, where three PCI sampling boards are installed. Two of them deliver analogue I/O signals at a sampling rate up to 5 MS/s. Both are of NI 6110 with 4 inputs and perform 12-bit resolution at an input range of ± 42 V. The last board is a high-speed 32-bit digital I/O device, NI 6533. There are 16 digital I/O lines with a maximum sampling rate of 20 MS/s. All three boards can receive the trigger signal, and usually it is received by one of the analogue boards. The analogue boards are connected to measuring devices via BNC-2110 connector blocks, and the digital board via a SCB-68 connector block.

The data acquisition is controlled by a LabVIEW application. In the application, user interface parameters such as sampling rate, sampling time, project name and board and channel selections are easily defined. Four files are generated each time the application is triggered. There is a set-up file giving the settings for each run, an ASCII file giving the measured data for the eight analogue inputs, an ASCII file giving the measured data for the 16 digital inputs and a binary file gathering all the acquired data. In this first version of the LabVIEW application, a pretrigger function is not implemented. The application is activated by a signal induced by the ignition system, and because the activation of the application needs some time, the ignition time cannot be exactly determined. Analyses of the data is performed in MATLAB.

3.2 Test of Kistler pressure transducers

In some experiments with strong FA, where fuels such as acetylene and hydrogen were used, it seems as if the pressure records with Kistler 7261 had a delay in the signal due to a long response time in the transducer. To control the rise time for the Kistler 7261 transducers and to compare the rise time and the pressure record for Kistler 603B and 7261, experiments with a shock tube were performed.

The shock tube was prepared by connecting a 1 m steel pipe with a 2 m steel pipe, both of 22.3 mm ID, by screwed flanges. Four layers of aluminium foil are inserted as a diaphragm at the interface between the two pipes. The experiments are performed by increasing the pressure in the 1 m pipe until the diaphragm is broken. A shock wave will then propagate into the 2 m pipe. Four transducers are used to measure the pressure in the pipes. One 7261 is placed on the 1 m pipe, 100 mm from the flange, the three others on the 2 m pipe. The first one on the 2 m pipe is a 7261, placed 100 mm from the diaphragm, the second is a 603B at 760 mm from the diaphragm and the third is a 7261 at 1400 mm from the diaphragm. The pressure in the high pressure

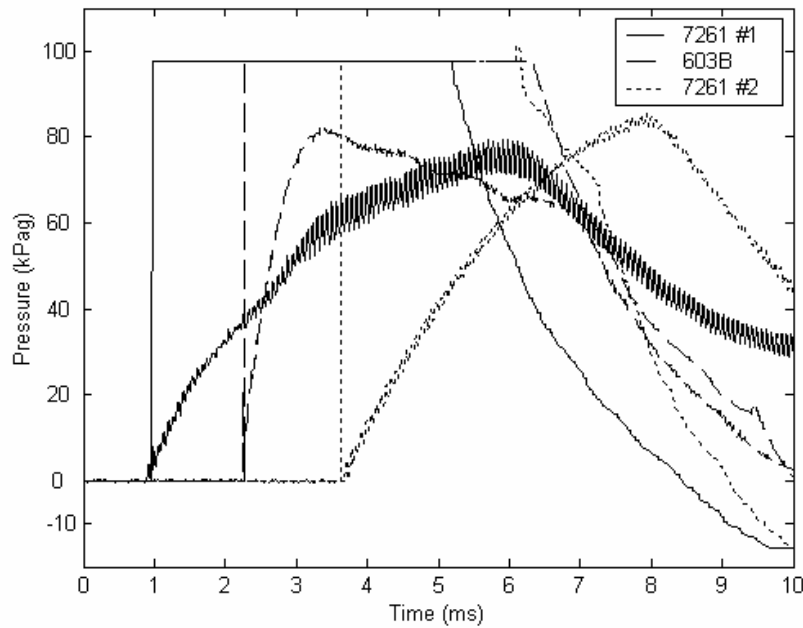


Figure 3.12: Results of shock-tube experiments and simulations. Three transducers are tested.

section increases monotonically from the initiation of air supply up to around 450 kPa, before the diaphragm is broken. The recorded pressures at the three transducers in the low pressure section are shown in Figure 3.12 together with simulation results. After the maximum pressure recorded at the 603B transducer is reached, the pressure starts to decrease because the piezoelectric transducer is not exposed to a change in pressure. This decrease continues in some ms until the transducer is hit by a rarefaction wave. The gradient of the pressure history is then considerably changed. To test if this first decrease is caused by temperature changes at the transducer, the transducer end was coated in silicone, but no effect could be recognized.

The response time is determined as the rise time from the initial atmospheric condition to 63%¹ of the maximum pressure is reached. The 603B transducer has a significantly lower response time than the 7261 transducers, with a response time of around 0.4 ms. The 7261 transducers have a response time just below 2.0 ms, which is too long to accurately measure pressure values in fast flames.

A simulation of the shock tube is performed in the 1D RCMLAB. The simulated pressure histories for the three transducer positions are also shown in Figure 3.12. Initial pressure values were 450 kPa in the high pressure section and 101.3 kPa in the

¹The value reached after a time t can be defined as the fraction $1 - e^{-t/\tau_{\text{resp}}}$ of the final value when τ_{resp} is the response time. The value reached at the response time is therefore $1 - e^{-1} \times$ final value = $0.63 \times$ final value.

low pressure section, and the same dimensions as in the experiments were used. The simulated pressure records show an instantaneous increase when the shock is passing the transducers, and remain constant for a period on pressure values somewhat higher than the experimental records. This means that neither of the transducers in these set-ups have a response time short enough to capture a shock wave. For the 7261, only pressure waves generated from slow FA can be considered as properly captured. 603B with the adapter (Figure 3.7) can capture pressure waves from stronger acceleration, but consequently not when shocks are generated.

3.3 Experimental results

Experiments are performed with the three fuels propane, acetylene and hydrogen in fuel-air mixtures at various equivalence ratios. According to the criteria given in Section 2.5, strong FA is only expected for acetylene-air and hydrogen-air mixtures in these experimental set-ups. In the steel pipes, all three fuels are used, but because the high pressures generated by combustion of acetylene and hydrogen are capable of destroying the plexiglass pipe only propane is used in this pipe. The experimental conditions are kept as close as possible to the normal conditions at 1 atm and 293 K. Some minor changes in the gas temperature will occur due to changes in room temperature and to increases in the temperature in the pipe wall during a sequence of trials. The premixed gas mixture is filled into the pipe for a sufficient time period whereby a homogeneous mixture at the right concentration can be assumed to exist in the pipe. During the filling time, all of the products from the previous trial are assumed to escape from the pipe. The gas filling is stopped just prior to the ignition of the gas mixture. For each equivalence ratio and pipe specification usually at least three trials were performed. In the following subsections, the results obtained in the experiments are described.

The experiments have been divided into 7 campaigns. The specifications for each campaign are pipe material, length and diameter, fuel type and diagnostic systems other than pressure transducers. A concise description of the experiments are given in Table 3.1.

Table 3.1: Experimental work, only diagnostics other than pressure transducers are given.

Campaign	1	2	3	4
Fuel	Propane	Propane	Acetylene	Hydrogen
Pipe material	Steel	Steel	Steel	Steel
Diameter (mm)	22.3	22.3	22.3	22.3
Length (m)	1, 2, 5, 11	2	2	2
Diagnostics		Photodiodes	Photodiodes	
Campaign	5	6	7	
Fuel	Acetylene	Propane	Propane	
Pipe material	Steel w/obstr	Plexiglass	Plexiglass	
Diameter (mm)	22.3	40	40	
Length (m)	5	1.9	1.9	
Diagnostics		SLR camera	High-speed camera	

3.3.1 Propane-air mixtures in various lengths of steel pipes

Experiments with propane-air mixtures at various equivalence ratios are performed in 4 pipe lengths of 1, 2, 5 and 11 m. Pressure records are obtained by four Kistler 7261 transducers along the pipes.

1 m steel pipe

Experiments are performed in the 1 m steel pipe with propane-air mixtures at various equivalence ratios. The transducer positions were at 100 mm, 382 mm, 700 mm and 900 mm from the closed end of the pipe. Two trials with stoichiometric mixtures are shown in Figure 3.13. The positions of the pressure transducers are given on the right ordinate axis with the measured overpressure by each transducer defined by the left ordinate axis. The repeatability is good, with a discrepancy only at the end of the last oscillation. The first pressure wave is generated during the initial flame acceleration. At the first transducer, an increase in the pressure is registered 3 ms after the logging is initiated. The first pressure maximum with an overpressure of 14.0 kPag occurs after 10 ms, and the flame is therefore accelerated in 7 ms. The flame is accelerated as long as the flame surface area is increased. When the flame front first reaches the pipe wall, the flame is quenched in the contact area. During this process, the flame surface area decreases and a rarefaction wave is generated. The first pressure maximum should therefore appear at the time when the flame front reaches the pipe wall and the maximum surface area is achieved. This time has previously been called t_{wall} . Equation 2.2 gives the value of t_{wall} defined from the model of propagation of a finger flame by Clanet and Searby (1996). The input variables to this model are the

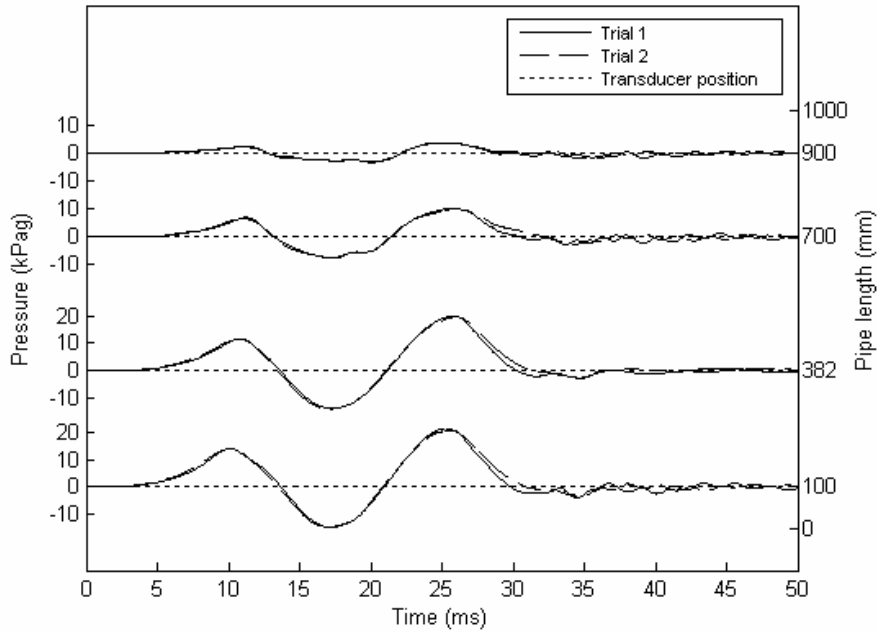


Figure 3.13: Experimental results for two stoichiometric propane-air mixtures in the 1 m steel pipe. The pressure values recorded at the four transducer positions along the pipe are shown at their locations.

pipe radius and the laminar burning velocity, which in the experiments are 0.011 m and 0.44 m/s (Law, 1993) respectively. The value of t_{wall} from the model is then:

$$t_{\text{wall}} = 0.26 (r/S_L) \pm 0.02 (r/S_L) = 6.50 \pm 0.50 \text{ ms}$$

The difference between the value of t_{wall} from the model and the time of the first pressure rise at transducer 1 in the experiments is 0.5 ms. In this case, there is good agreement between the pressure rise time and t_{wall} , but because of the uncertainties in the exact determination of the ignition time in the present experiments, further comparison of the values for t_{wall} will not be adequate. The second pressure maximum occurs at 25.2 ms, with an overpressure of 21.0 kPag. The frequency mode obtained by an FFT analysis of the acoustic oscillations in the pipe is therefore 66.7 Hz. The amplitude of the pressure wave is attenuated as it propagates through the pipe, and when the first pressure maximum is registered at transducer 4 after 11.5 ms the amplitude is reduced to an overpressure of 2.5 kPag.

The results of two experiments with an equivalence ratio of 1.2 in the same pipe length are shown in Figure 3.14. The generated pressure waves are somewhat larger in these rich mixtures and the first pressure maximum in trial 1 has an amplitude of 19.3 kPag.

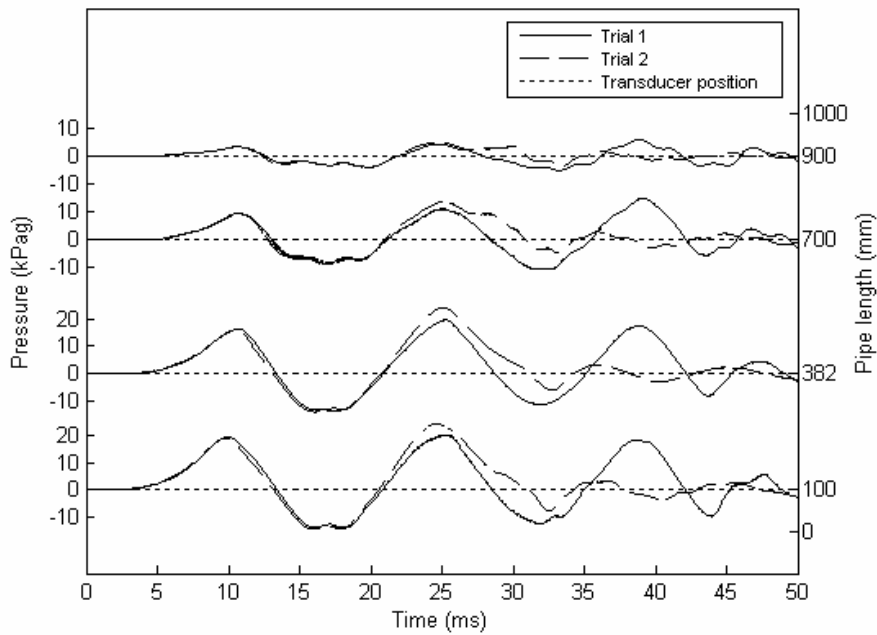


Figure 3.14: Experimental results for two propane-air mixtures at $\phi = 1.2$ in the 1 m steel pipe. The pressure values recorded at the four transducer positions along the pipe are shown at their locations.

2 m pipe

Experiments are performed in the 2 m steel pipe with propane-air mixtures at several equivalence ratios. The propagation of pressure waves in the pipe is recorded by pressure transducers located at 100 mm, 764 mm, 1400 mm and 1900 mm from the ignition point. Two examples of pressure records for stoichiometric propane-air mixtures are shown in Figure 3.15. The maximum pressures obtained are 20.6 kPag after 87 ms and 23.7 kPag after 60 ms respectively. The maximum pressure of the first pressure peak in trial 1 is 15.2 kPag. The frequency spectrum of the pressure oscillations is achieved by an FFT analysis, and in Figure 3.16 the frequency spectrum for trial 1 is given. The frequency mode is 38.2 Hz.

5 m pipe

Experiments are performed in the 5 m steel pipe with propane-air mixtures at several equivalence ratios. The propagation of pressure waves in the pipe is recorded by pressure transducers located at 100 mm, 1910 mm, 3500 mm and 4900 mm from the ignition point. In Figure 3.17, two examples of pressure records from experiments with equivalence ratio 0.8 are displayed. The acoustic waves are propagating in the pipe for a long time. Pressure is recorded at 800 ms and still there are oscillations in the pipe.

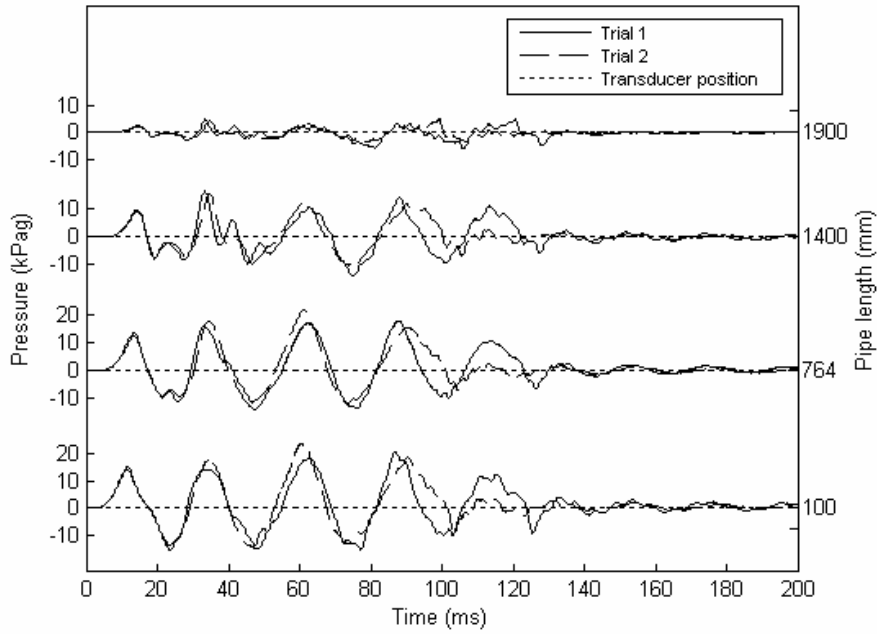


Figure 3.15: Experimental results for two propane-air mixtures at $\phi = 1.0$ in the 2 m steel pipe. The pressure values recorded at the four transducer positions along the pipe are shown at their locations.

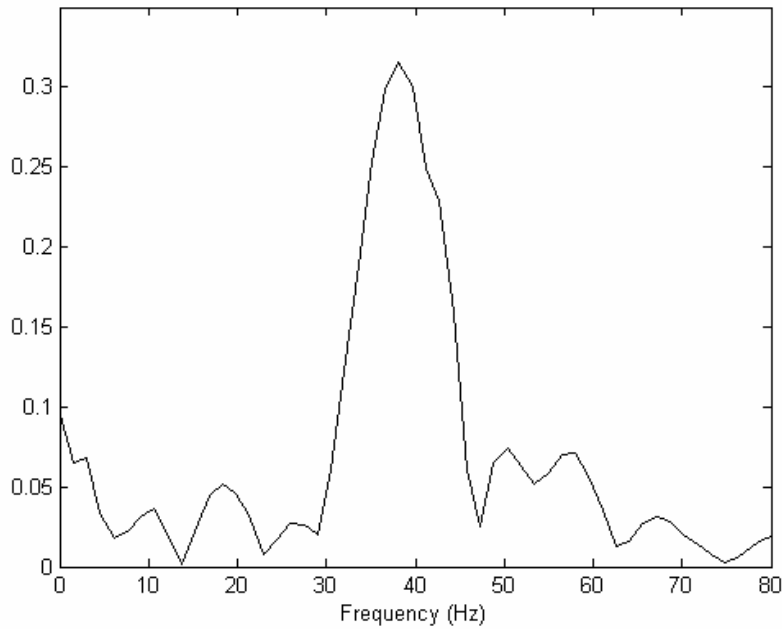


Figure 3.16: Frequency spectrum for the pressure oscillations in the 2 m steel pipe with a stoichiometric propane-air mixture.

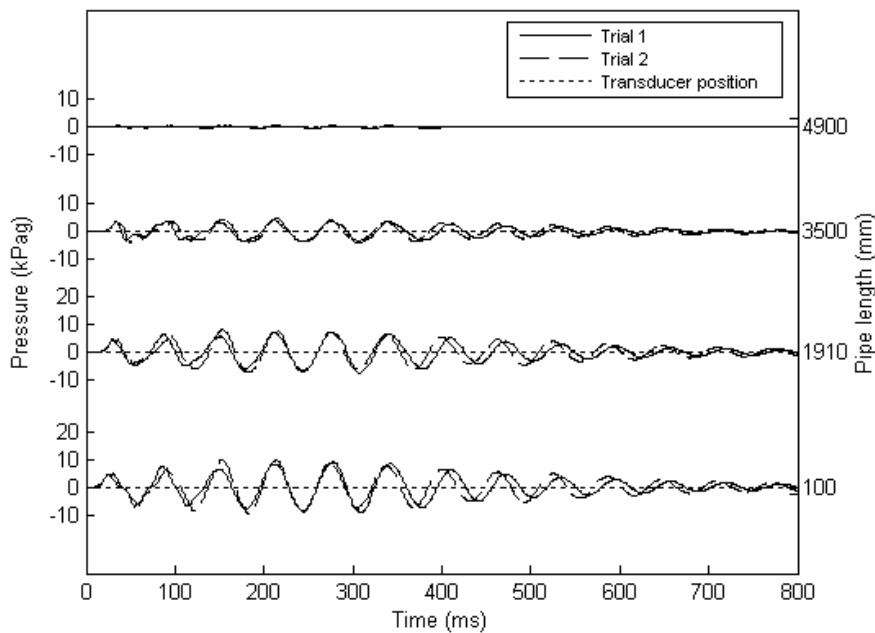


Figure 3.17: Experimental results for two propane-air mixtures at $\phi = 0.8$ in the 5 m steel pipe. The pressure values recorded at the four transducer positions along the pipe are shown at their locations.

The two trials have maximum pressures of 10.2 and 9.2 kPag at 215 and 278 ms, both recorded at transducer 1. After these maxima, the pressure continues to oscillate but the amplitude of the oscillations is continuously decreasing. This indicates that the heat release rate is decreasing and that the flame could be quenched. The frequency modes obtained from FFT analysis are 16.0 Hz for both trials.

Two trials with stoichiometric propane-air mixtures are shown in Figure 3.18. The pressure is greater than for the lean mixtures with a maximum pressure of 19.5 kPag for both trials, which occur at the third transducer at 103 ms and 63 ms respectively. In addition to the oscillations with larger wavelengths at a frequency of 16.0 Hz, there are initially oscillations with higher frequencies. These oscillations are probably occurring independently of the rarefaction wave reflected at the outlet and are therefore caused by acceleration and deceleration of the flame front due to the tulip flame phenomenon caused by quenching of the flame front at the pipe wall. The frequency of these oscillations is around 47.3 Hz for the first trial and varies from 46.5 to 51.1 Hz for the second trial.

When richer fuel-air mixtures were tested, higher pressures were observed and the maximum pressure of 30.4 kPag is achieved for an equivalence ratio of 1.6, as shown in Figure 3.19. These mixtures have initially an excess of fuel. When the acoustic

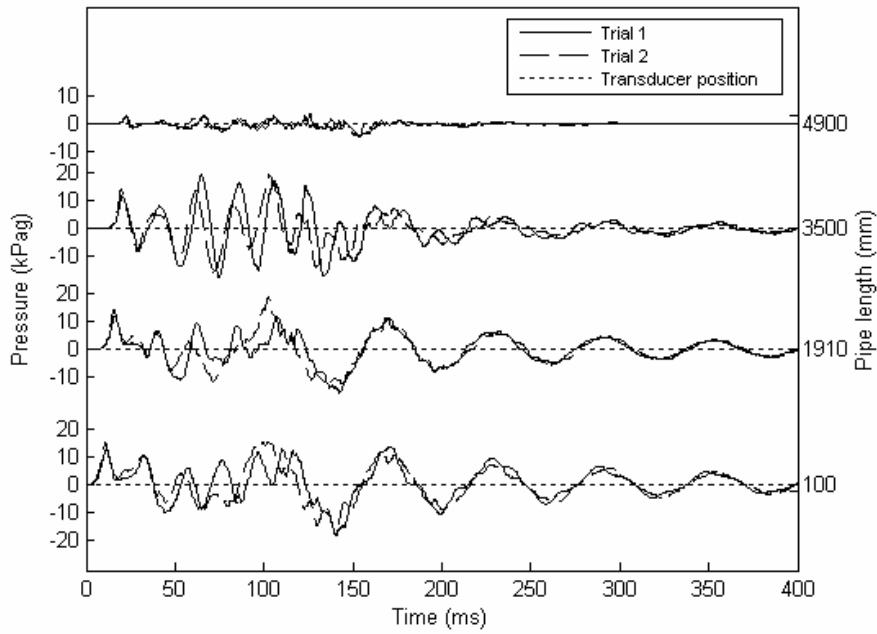


Figure 3.18: Experimental results for two propane-air mixtures at $\phi = 1.0$ in the 5 m steel pipe. The pressure values recorded at the four transducer positions along the pipe are shown at their locations.

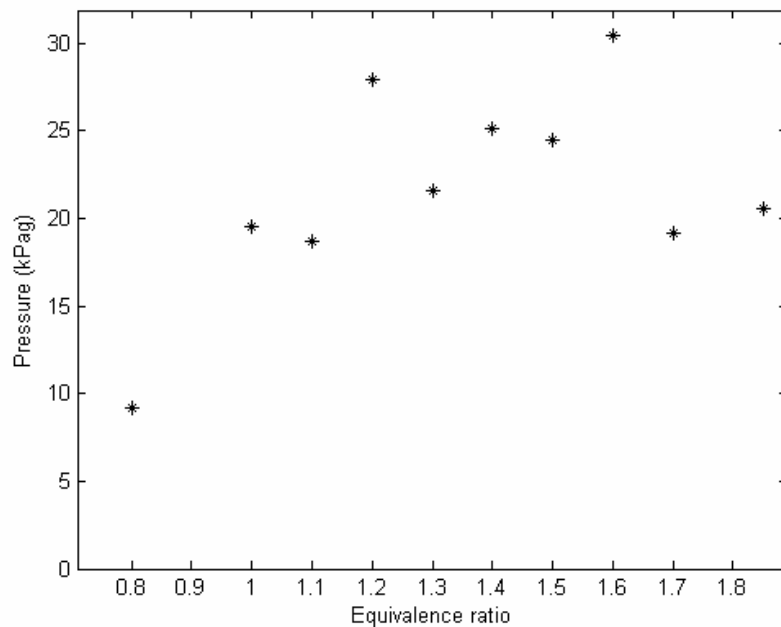


Figure 3.19: Maximum pressure recorded in the experiment for various equivalence ratios of propane-air mixtures in the 5 m pipe.

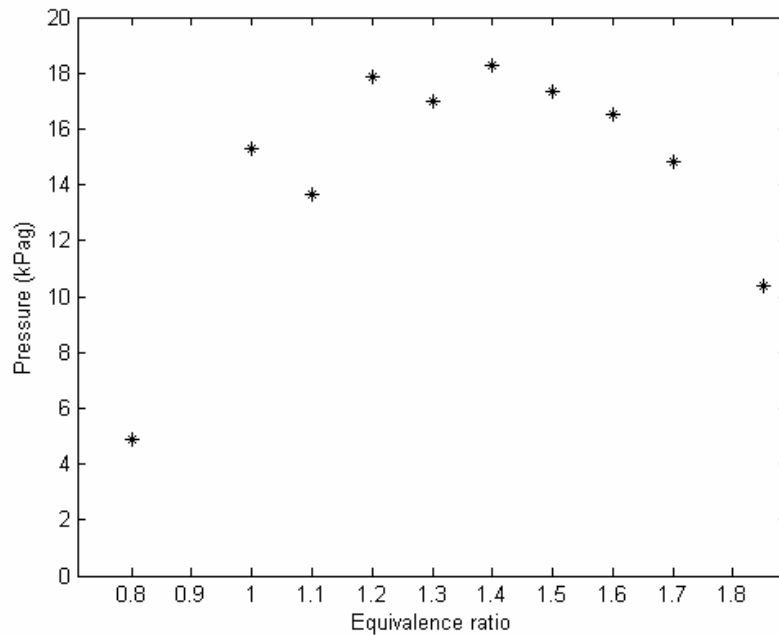


Figure 3.20: The first maximum pressure recorded at transducer 1 for propane-air mixtures at various equivalence ratios in the 5 m pipe.

waves are propagating in the pipe, oxygen from the vicinity of the pipe opening will be transported into the pipe while fuel escapes from the pipe. The unburnt mixture will then be more reactive than initially and the flame propagation is sustained for a longer time than in the initially more reactive mixtures with $\phi = 1.0$ and 1.1 , for which there are cases where the flame is quenched before it reaches the outlet. The heat release will therefore be larger for rich mixtures. The values of the first pressure maxima are summarized in Figure 3.20. The largest values are shifted slightly to the richer side than would be expected from the reactivity of the mixtures, with the maximum value observed at $\phi = 1.4$. For richer mixtures, the pressure values are decreasing monotonically. The frequency mode for the acoustic oscillations is close to 16.0 Hz for the various equivalence ratios in the 5 m pipe.

11 m pipe

Experiments are performed in the 11 m steel pipe with propane-air mixtures at various equivalence ratios. The pipe is prepared by connecting a 6 m pipe to the 5 m pipe described above. The pressure transducers are therefore placed at the same distances from the ignition point as for the 5 m pipe. The pipe length was increased to achieve a longer distance of flame propagation before the flame front is reached by the reflected rarefaction waves. One example of pressure records for the stoichiometric propane-air

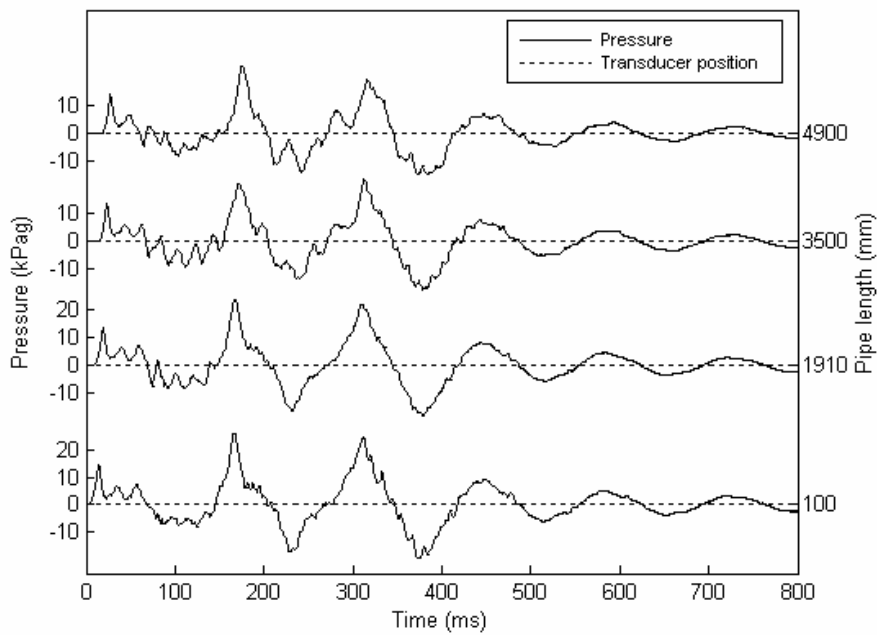


Figure 3.21: Experimental results for two propane-air mixtures at $\phi = 1.0$ in the 11 m steel pipe. The pressure values recorded at the four transducer positions along the pipe are shown at their locations.

mixtures is shown in Figure 3.21. Because the pressure transducers are placed in the first part of the pipe, only the first 5 m of the pipe length are shown. The pressure history at transducer 1 consists of three peaks before the acoustic oscillations begin to influence the flame propagation. These peaks are probably a result of acceleration and deceleration of the flame propagation due to multiple inversions of the flame front when the flame is quenched at the pipe wall. The first peak is somewhat higher than the two others, which are on an equal level. The first acceleration after ignition is therefore stronger than in the two following acceleration periods, where the acceleration occurs after inversions. The experiments in the 11 m pipe gave somewhat different pressure histories for the first pressure peak than for the shorter pipes. This may be explained by a slight deviation in the fuel concentrations since the experiments in the 11 m pipe were performed half a year later.

Concluding remarks

The experiments demonstrate that longitudinal acoustic waves appear in the pipes. These waves are initiated by the initial flame acceleration and are sustained by the continuous heat release as long as the flame is in the pipe. The frequency of the acoustic oscillations is given by the pipe length. As shown above, the frequency of the

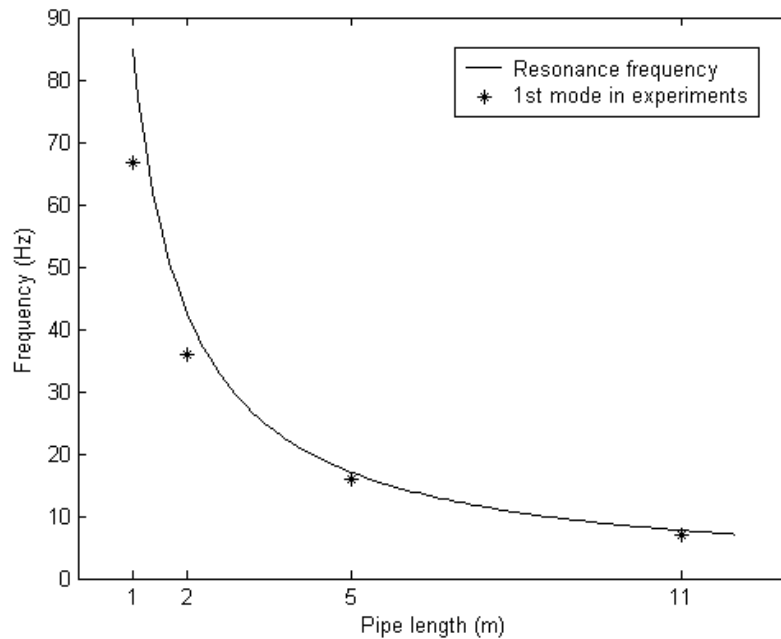


Figure 3.22: First frequency mode from an FFT analysis of the pressure records compared to the resonance frequency in unburnt gas. Stoichiometric propane-air mixtures.

oscillations can be determined by an FFT analysis. The first frequency mode obtained for the four pipe lengths are compared to the resonance frequency for the same pipe lengths with unburnt gas mixture in Figure 3.22.

The first pressure peak is, however, independent of the pipe length for pipe lengths exceeding a certain pipe length. As shown in Figure 3.23, the first pressure peaks are approximately similar for the 2 and 5 m pipes, but in the 1 m pipe the first pressure peaks are influenced by the acoustic oscillations in the pipe.

The acoustic oscillations are connected to inversions of the flame front. These inversions are caused either by the quenching of the flame front at the pipe wall or by interactions of the flame front with pressure waves. For long pipes, such as the 11 m pipe, there are multiple pressure peaks at higher frequencies than the oscillations controlled by the pipe lengths. This indicates that there are multiple inversions of the flame front by wall quenching. For shorter pipes, such as the 1 m pipe, the pressure waves will affect even the first inversion.

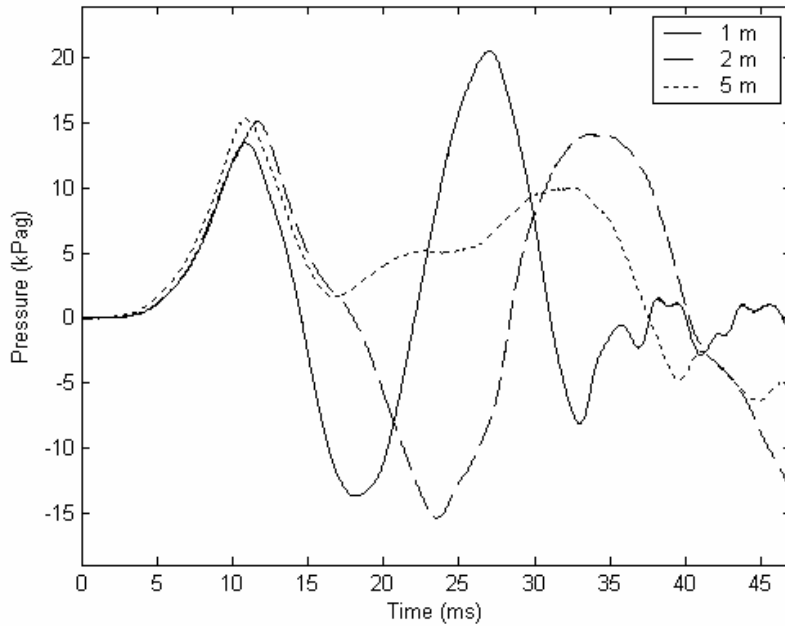


Figure 3.23: Pressure records at the first transducer for the three pipe lengths. Propane-air mixtures at equivalence ratio 1.0.

3.3.2 Propane-air mixtures in a 2 m steel pipe

In these experiments with propane-air mixtures in the 2 m steel pipe, the flame propagation is captured by the optical sensors TSL250 together with the pressure records. The photodiodes on the optical sensors and the pressure transducers are placed at the same positions along the pipe. It could often be a problem to determine one point as the flame arrival time at one photodiode positions. The flame front will have a certain extension, flame oscillations can occur around a photodiode position, and there is a question whether the time of the first light recognized by the photodiodes or the time of the maximum value captured should be defined as the flame arrival time. To better imagine how the flame propagates in the pipe, the analogue signals from each photodiode are therefore plotted at their positions together with the pressure records. The maximum value of the analogue signal from the optical sensors is around 3.6 V, which is obtained when an input voltage of 5 V is used. In the figures, the output analogue signal is multiplied with a factor of 6 to make it more visible in the range of the pressure records, and the maximum values plotted are around 22 V. The pressures in this campaign are lower than in campaign 1. These deviations may be attributed to the fact that campaign 2 was performed around one year later than campaign 1 after some modifications in the equipment had been accomplished.

The experimental results for an equivalence ratio of 0.9 are shown in Figure 3.24.

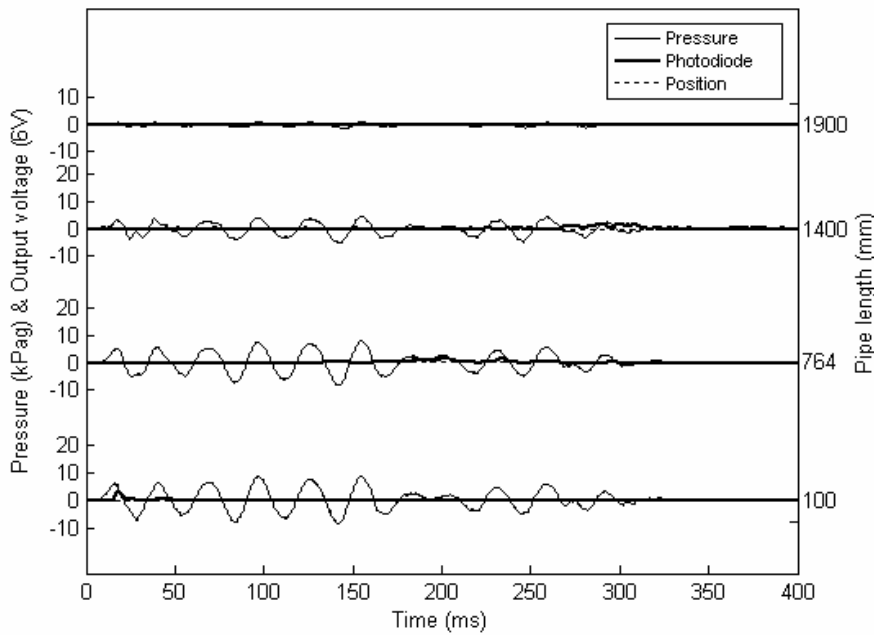


Figure 3.24: Experimental results for propane-air mixture at $\phi = 0.9$ in the 2 m steel pipe. The pressure and photodiode records are shown at their four positions along the pipe.

The signals from the photodiodes are small, which indicate that there is low light emission from the flame in this lean mixture. At photodiode 4, there is no signal and it can therefore be assumed that the flame is quenched between photodiodes 3 and 4. From the pressure records it seems as if the flame is partly quenched after around 200 ms, but the flame propagation is not completely stopped until it has passed photodiode 3 at 1.4 m from the ignition point. The first peak in the voltage signal from photodiode 3 occurs at 273 ms. When the flame arrival time is taken as the time of the first maximum value at this position, the average flame speed to the third position is 5.1 m/s. That a flame front would not reach the open end of the pipe has also been observed by Kerampran et al. (2001). They added helium to a stoichiometric mixture of propane-air and attributed the phenomenon to an increased frequency of the acoustic oscillations because of an increased sound of speed, and to the high diffusivity in air that could dilute the mixture near the outlet below the lower flammability limit.

One experiment with stoichiometric propane-air mixture is shown in Figure 3.25. The flame arrival time at photodiode 4 is 104 ms and the average flame speed is 18.3 m/s. The arrival time is determined as the time for the highest value or the time when the maximum output voltage value is reached for the first distinct light measurement.

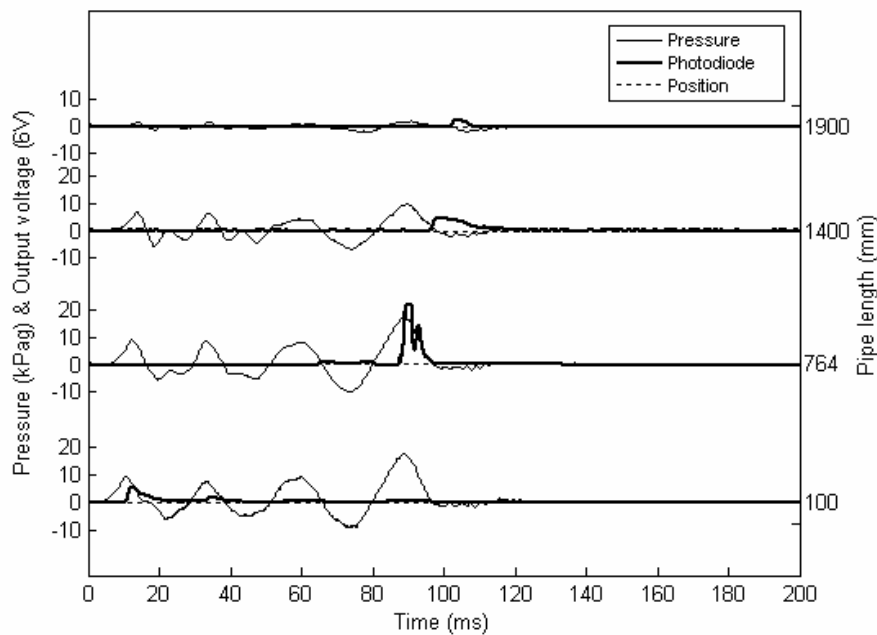


Figure 3.25: Experimental results for propane-air mixture at $\phi = 1.0$ in the 2 m steel pipe. The pressure and photodiode records are shown at their four positions along the pipe.

After the last peak at photodiode 2, the flame propagation is accelerated steadily towards the pipe opening.

The result of one experiment with propane-air mixture of equivalence ratio 1.1 is shown in Figure 3.26. The flame arrival time at the fourth position and the average flame speed are 102 ms and 18.6 m/s. From the photodiode measurements, it can clearly be concluded that the flame propagation has some oscillations before it is accelerated steadily towards the opening. At photodiode 2, three distinct peaks can be recognized. The first one is very small and probably occurs when the flame front is at its maximum position before an inversion. The flame front does not reach the photodiode position, however light emitted by the flame will be captured by the photodiode. The two other peaks reach the maximum output voltage and it can be assumed that the flame front reaches the photodiode position at both these peaks. The flame propagation is reversed between these two peaks and because the time of the second peak is somewhat longer than the first peak the last turning point of the flame propagation will probably be around position two at the time of the last peak.

In Figure 3.27, one example of the experiments with propane-air mixtures at $\phi = 1.2$ is shown. The flame is accelerated towards the opening after two oscillations around the second position, but after the flame has passed the fourth position it propagates

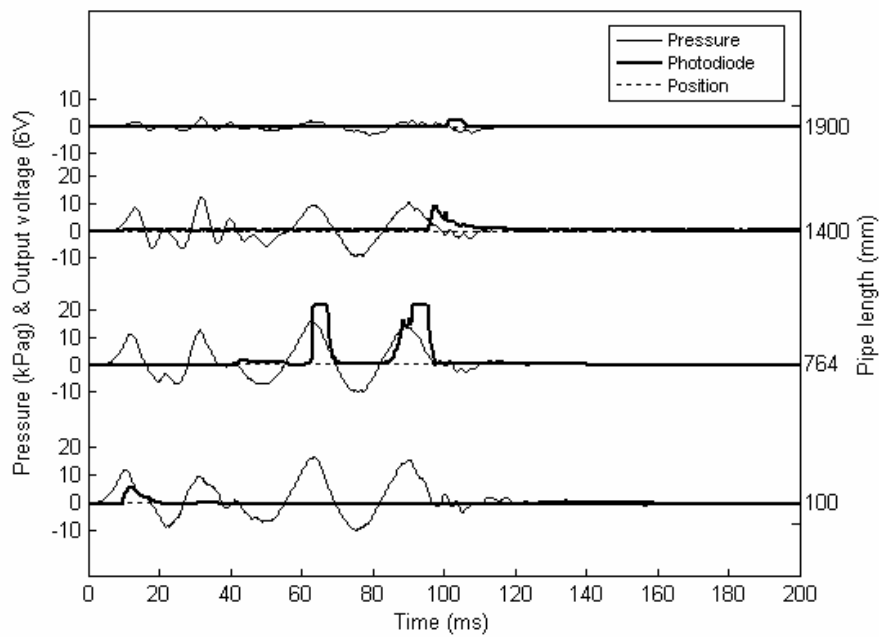


Figure 3.26: Experimental results for propane-air mixture at $\phi = 1.1$ in the 2 m steel pipe. The pressure and photodiode records are shown at their four positions along the pipe.

backwards in the pipe and is quenched after it has reached the third position. This reversal after the flame has reached the outlet could be due to an excess of fuel in the pipe and that the combustion is completed when air is supplied from the vicinity of the pipe opening. The arrival time at the fourth position is 94 ms, which gives an average flame speed of 20.2 m/s. The emission of light is greater for this mixture than for the mixture with less fuel, which can be seen from the increased voltage signal from the first photodiode and by the longer exposure time at all photodiodes.

In Figure 3.28, an interesting experiment with equivalence ratio 1.4 is shown. The flame is nearly quenched after the second position, but is reaccelerated again and propagates to the pipe outlet.

One trial with the propane-air mixtures at $\phi = 1.5$ is shown in Figure 3.29. The arrival time at the fourth position is 152 ms, which gives an average flame speed of 12.5 m/s.

The average flame speed can be determined by the time the flame front needs to reach a certain point. It has to be emphasized that there is an uncertainty in the exact determination of the ignition time. This uncertainty has to be taken into consideration also for the average flame speed. A summary of these average flame speeds is given in Figure 3.30. For $\phi = 0.8$ and 0.9 the flame is quenched before it

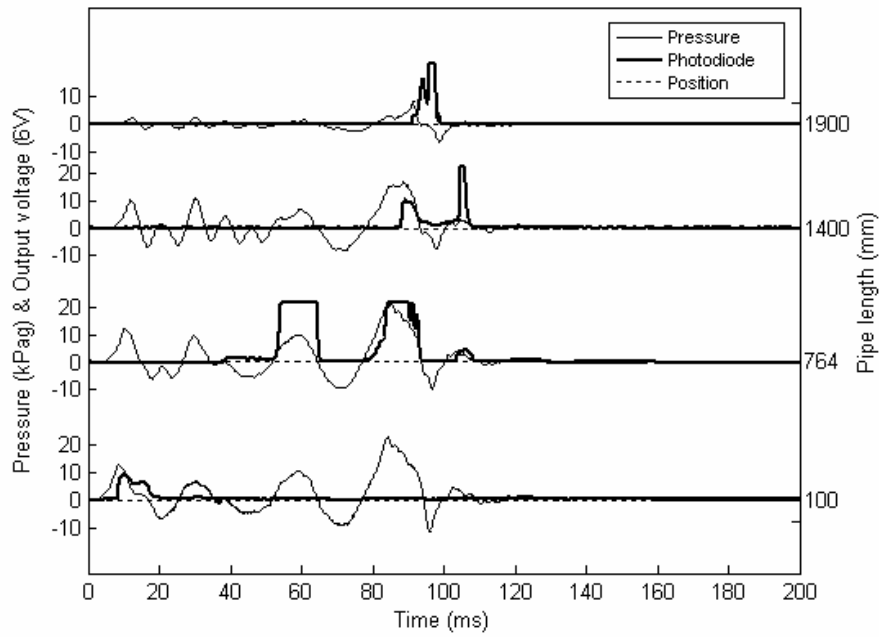


Figure 3.27: Experimental results for propane-air mixture at $\phi = 1.2$ in the 2 m steel pipe. The pressure and photodiode records are shown at their four positions along the pipe.

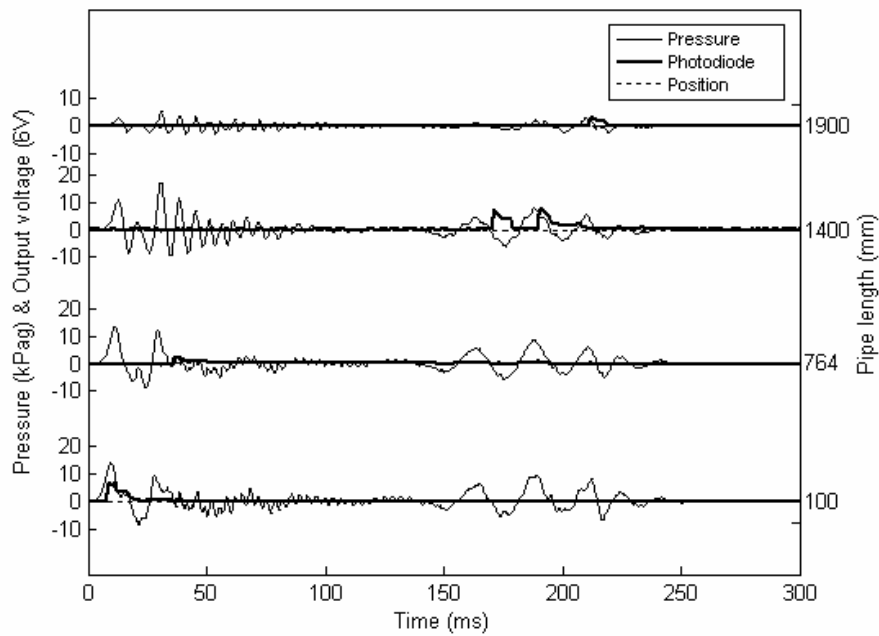


Figure 3.28: Experimental results for propane-air mixture at $\phi = 1.4$ in the 2 m steel pipe. The pressure and photodiode records are shown at their four positions along the pipe.

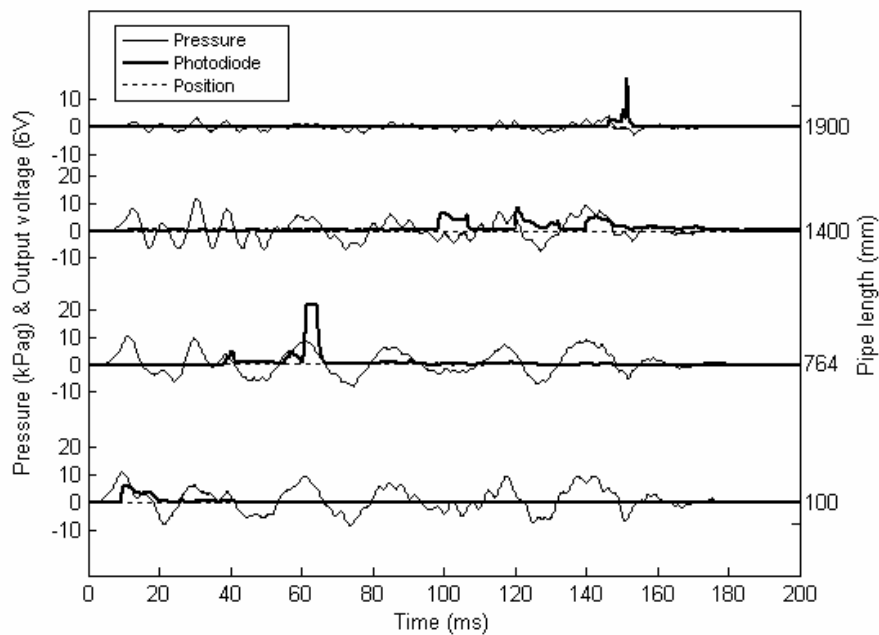


Figure 3.29: Experimental results for propane-air mixture at $\phi = 1.5$ in the 2 m steel pipe. The pressure and photodiode records are shown at their four positions along the pipe.

reaches photodiode 4 and the average flame speed up to photodiode 3 is calculated. For the other equivalence ratios the average flame speed up to photodiode 4 is used. When photodiode 3 is used, the average flame speed should become smaller than if photodiode 4 is used because the flame is usually accelerated towards the pipe outlet. The maximum average flame speed is obtained for $\phi = 1.2$ and is just above 20 m/s. The average flame speed is largely determined by the number of oscillations in the pipe because one more oscillation will increase the residence time of the flame considerably.

The time of occurrence for the first pressure peak should agree with the time when the flame front first hits the pipe wall, t_{wall} , which depends on the laminar burning velocity. In Figure 3.31, these times are plotted versus equivalence ratios. These times are determined as the period from the first signal is recognized at transducer 1 to where the first pressure peak appears at the same transducer. When plotted against the equivalence ratios, the curve takes on a parabolic shape with a minimum at $\phi = 1.3$.

In Figures 3.32 and 3.33, the flame arrival times at each photodiode are summarized for several equivalence ratios. Figure 3.33 is an enlarged version of Figure 3.32, where the ordinate axis is reduced in order to get a better picture of the more reactive mixtures. The two lean mixtures are both being quenched before they reach the

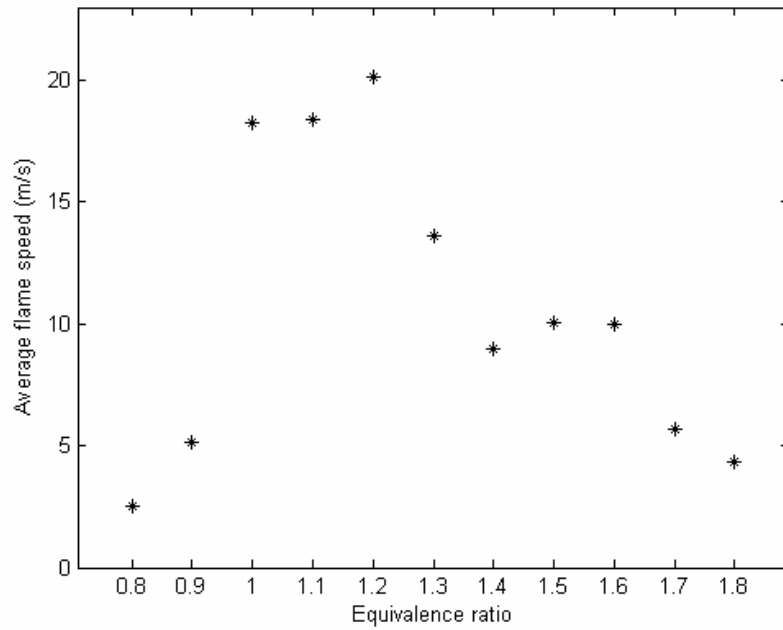


Figure 3.30: Average flame speed to photodiodes 3 or 4 for various propane-air mixtures in the 2 m steel pipe.

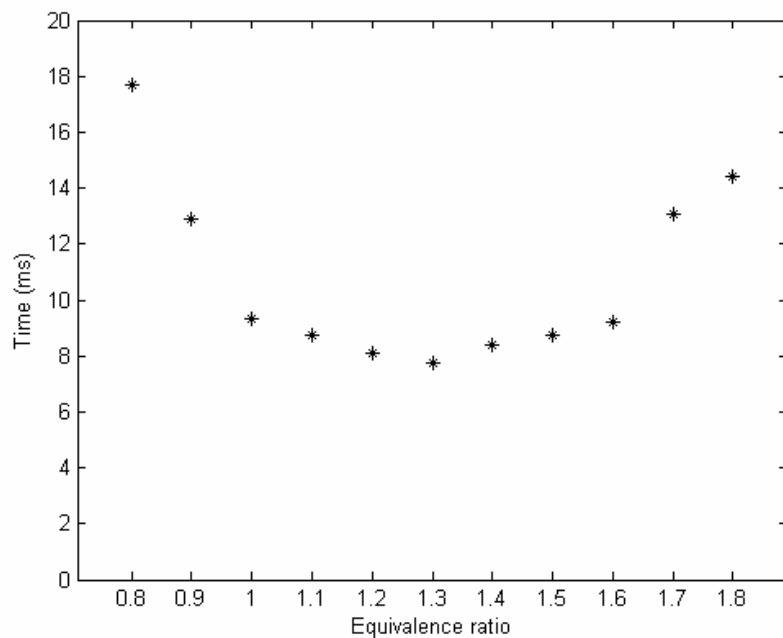


Figure 3.31: Time of the first pressure maximum for experiments with various propane-air mixtures in the 2 m steel pipe.

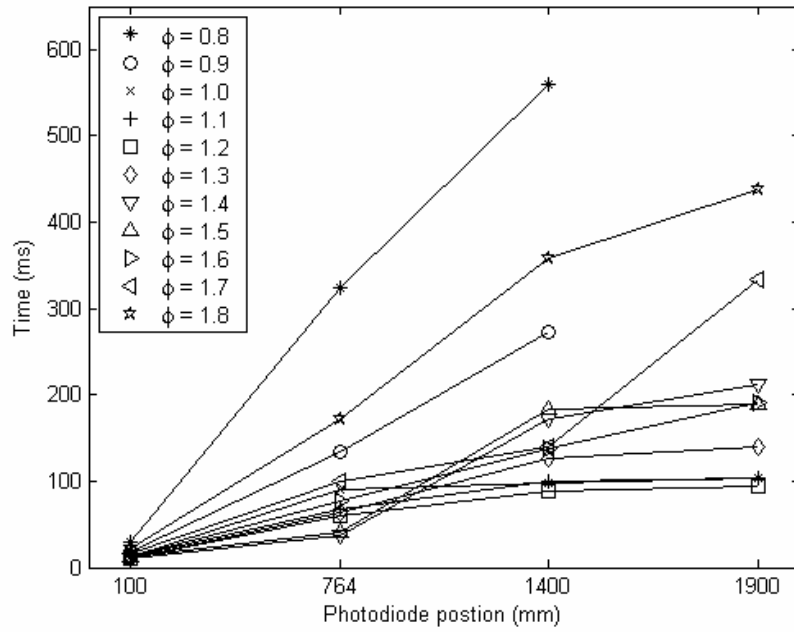


Figure 3.32: Flame arrival times at the four photodiodes for various propane-air mixtures in the 2 m steel pipe.

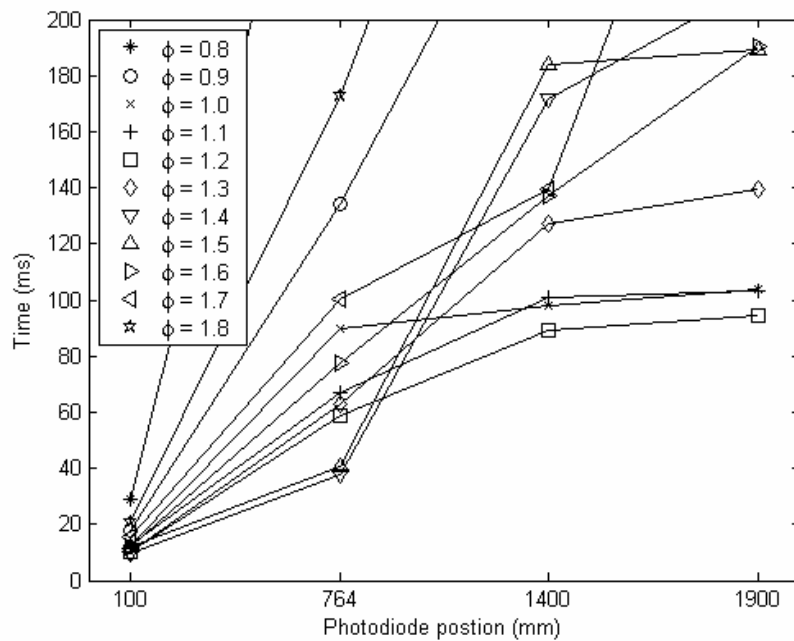


Figure 3.33: Flame arrival times at the four photodiodes for various propane-air mixtures in the 2 m steel pipe. (Enlarged version of Figure 3.32)

fourth position, while the mixture with $\phi = 1.8$ is not quenched despite the flame propagation being slower than for $\phi = 0.9$. It is clear to see that in most mixtures the flame accelerates when it approaches the pipe outlet. The discontinuous flame acceleration is caused by flame oscillations where the flame propagation is reversed.

3.3.3 Acetylene-air mixtures in a 2 m steel pipe

Experiments are performed with acetylene-air mixtures at various equivalence ratios in the 2 m steel pipe. Flame propagation is captured by photodiodes on the optical sensors TSL250 and pressure is measured by Kistler 603B transducers in the set-up shown in Figure 3.7. One example of the experiments with an equivalence ratio of 0.8 is shown in Figure 3.34. The pressures are shown by solid lines and the signal from the photodiodes by dashed lines. Values are shown at their positions along the pipe. The signals from the optical sensors are enhanced by a factor of 20 to make the signal visible within the pressure range. It is apparent that the light emission is greater for the acetylene-air mixtures than for the propane-air mixtures. At all photodiodes, the maximum output voltage is reached and the signal remains at this value for a certain time, which means that the flame would be more elongated than in the cases with propane. When the flame is accelerated, the increase of the photodiode signals also becomes steeper, which indicates that the light emission is increased above the maximum level of the photodiodes even from the first signals that are recognized. There are tails of lower emission at the end of the combustion zones. The flame reached photodiode 4 after 31 ms, which gives an average flame speed of 61.3 m/s up to this photodiode. The flame is initially accelerated due to an increase of the flame surface area. A pressure wave is generated which has its maximum value when the first flame inversion occurs due to wall quenching. Due to instability mechanisms and turbulence generation, the flame will again be accelerated after the inversion, now continuously towards the pipe opening. The pressure has a maximum value of 29.6 kPag, which occurs after the first acceleration at around 3 ms.

In Figure 3.35, an example of the experiments with stoichiometric mixtures is shown. This mixture is more reactive than the previous one and has an average flame speed of 106.1 m/s. The first maximum amplitude occurs after 2 ms and has a value of 41.0 kPag. At the pipe end, a secondary explosion is recognized. The largest pressure peak after this explosion was recorded at transducer 4. It is therefore probable that this secondary explosion occurs after the flame has passed transducer 3 and that the flame has accelerated towards the pipe opening. Pressure waves would however propagate in both directions, but are larger in the direction of the flame propagation. The peak value of the pressure recorded by transducer 4 is 629.8 kPag. Only a portion of the

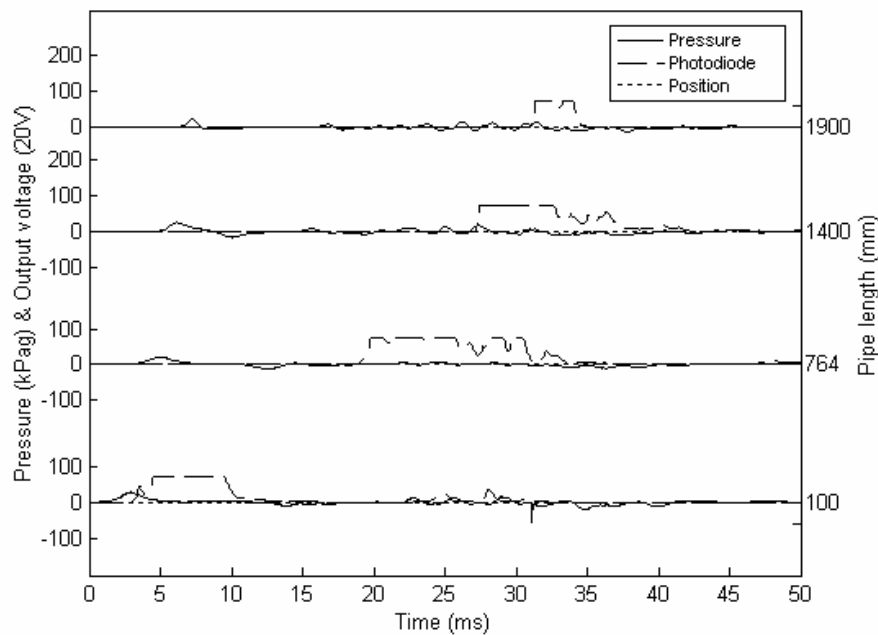


Figure 3.34: Experimental results for acetylene-air mixture at $\phi = 0.8$ in the 2 m steel pipe. The pressure and photodiode records are shown at their four positions along the pipe.

peak is shown in Figure 3.35 in order to keep the pressure in a range where pressure waves other than the pressure peak are also visible.

In Figure 3.36, the results of an experiment with $\phi = 1.2$ are shown. For this mixture, the second pressure peak first appears at transducer 2. The secondary explosion therefore occurs after a shorter run-up distance in the pipe. The flame propagation is strongly accelerating towards the pipe outlet but DDT has probably not occurred. The average flame speed is 244.6 m/s between photodiodes 2 and 3 and increases to 555.6 m/s between photodiodes 3 and 4.

The maximum pressures of the first pressure peak, which occur due to the initial flame acceleration, are shown in Figure 3.37 as a function of the equivalence ratio. The maximum pressure is observed at an equivalence ratio of 1.4. Average flame speeds in the pipes are calculated by using the flame arrival times at the fourth photodiode. Average flame speeds at various equivalence ratios are shown in Figure 3.38. The maximum value appears at an equivalence ratio of 1.4, but there are only minor changes in the average flame speed from 1.3 to 1.6. Law (1993) gave that the largest laminar burning velocity of 1.56 m/s occurs for an acetylene-air mixture of $\phi = 1.4$.

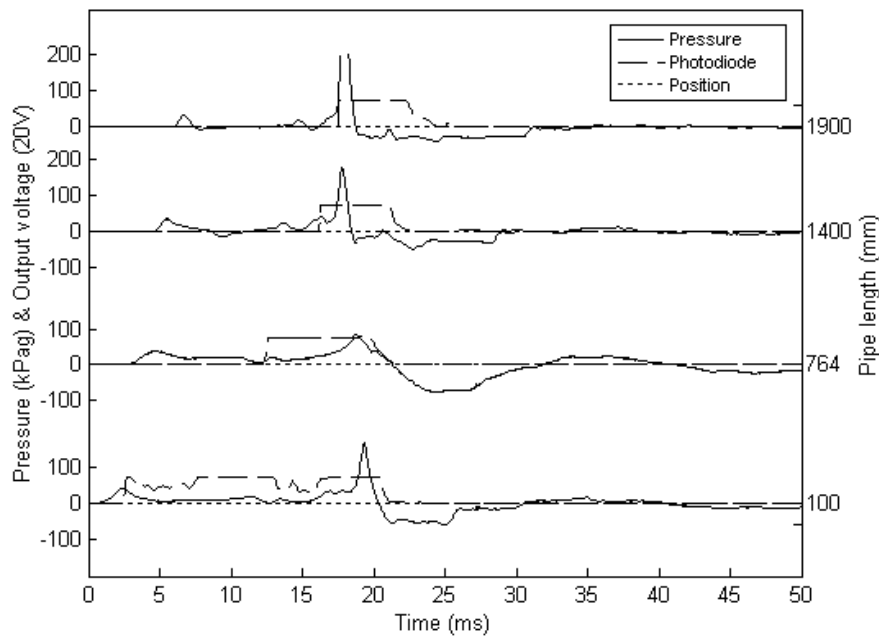


Figure 3.35: Experimental results for acetylene-air mixture at $\phi = 1.0$ in the 2 m steel pipe. The pressure and photodiode records are shown at their four positions along the pipe. Maximum value at transducer 4 is 629.8 kPag.

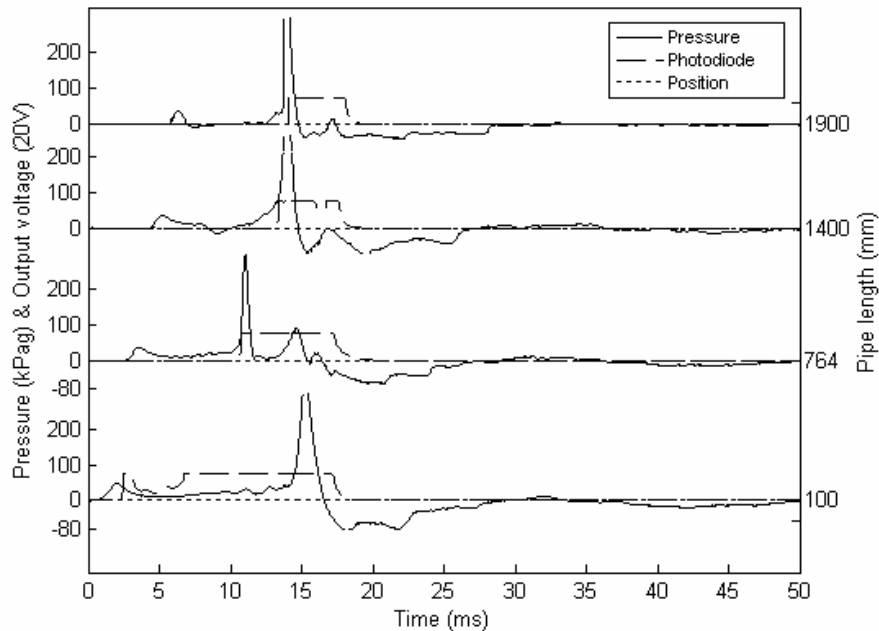


Figure 3.36: Experimental results for acetylene-air mixture at $\phi = 1.2$ in the 2 m steel pipe. The pressure and photodiode records are shown at their four positions along the pipe. Maximum values for the pressure peaks that have been cut off are in chronological order 367.6 kPag, 364.2 kPag and 796.3 kPag.

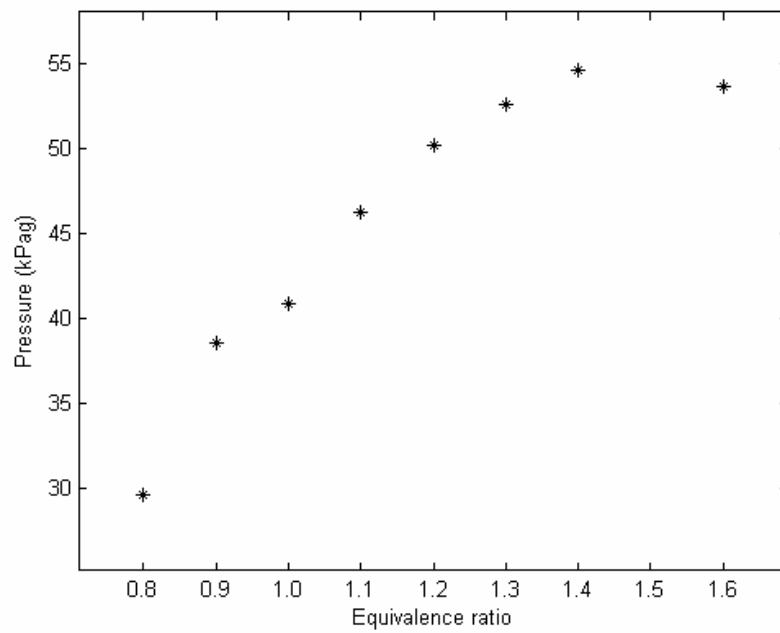


Figure 3.37: First pressure peak at transducer 1 versus equivalence ratio for acetylene-air mixtures in the 2 m steel pipe.

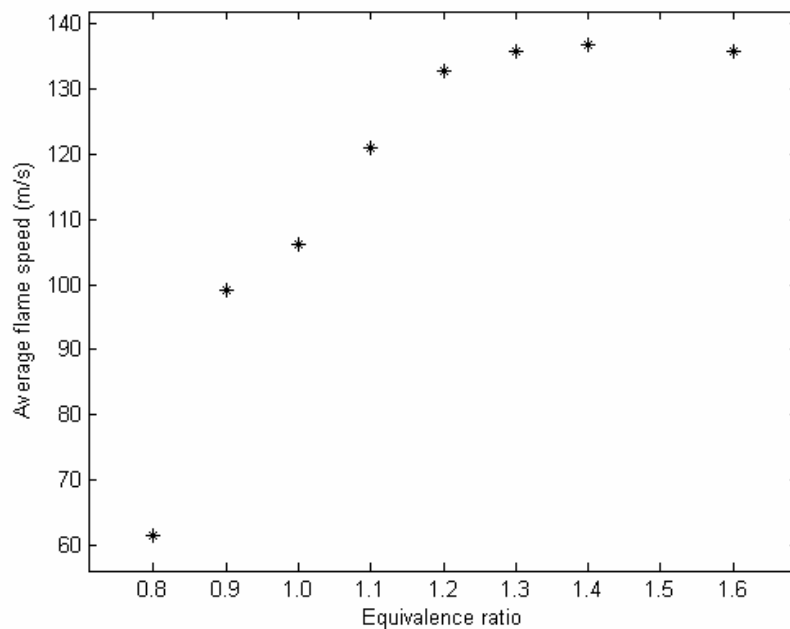


Figure 3.38: Average flame speed versus equivalence ratio for acetylene-air mixtures in the 2 m steel pipe.

3.3.4 Acetylene-air mixtures in a 5 m steel pipe

Experiments with acetylene-air mixtures at various equivalence ratios were performed in the 5 m steel pipe with large apertures for transducers as shown in Figure 3.8. Kistler 603B transducers were used to measure the pressure. Transition to detonations were experienced for all mixtures up to $\phi = 2.3$. DDT may be caused by the increased turbulence generation by the obstructions in the pipe at each transducer position. Just after the transition, the detonation will be overdriven and pressures well beyond the CJ values are measured. An example at $\phi = 1.1$ is shown in Figure 3.39. In this figure, the pressure history at each transducer is displayed, but the initial positions are displaced with 5 kPa for each transducer to make the figure more readable. The maximum pressure of 7000 kPag is measured by transducer 2, which indicate DDT (i.e. a highly overdriven detonation). When the detonation wave has reached transducer 3, the pressure is reduced to 2500 kPag and at transducer 4 to 1750 kPag. The CJ value calculated from SuperSTATE² is 1868 kPag. The detonation has therefore not become a steady CJ detonation. Possible reasons can be that transducer 4 is too near the pipe outlet that the detonation can sustain at the CJ conditions, or that the obstructions made by the transducer apertures will disturb the detonation propagation because the free pipe area is in the same size order as the detonation cell size (Knystautas et al., 1984). The detonation speed between transducer 3 and 4 is 1994 m/s and the CJ value from SuperSTATE is 1895 m/s. The difference may appear because the detonation has not reached the CJ value at transducer 3.

It can be assumed that the transition occurs closest to the transducer where the maximum pressure is recorded. The transducer position at which the maximum pressure is recorded can therefore be used as a qualitative measure for the run-up distance to DDT. In Figure 3.40, the times after ignition at which the maximum recorded pressures occur are given. The transducer positions at which these pressures are recorded are indicated by different symbols. For the more reactive mixtures, the maximum pressure is recorded at transducer 2, but for the other mixtures it is recorded at transducer 3 or 4. The run-up distance to DDT is therefore shorter for the more reactive mixtures. For $\phi = 1.0$, the initial flame propagation after ignition was very slow compared to the other experiments with a departure of 2 - 3 ms. This could explain the late maximum pressure recorded at transducer 2.

In Figure 3.41, the detonation speed for experiments at various equivalence ratios are presented. The detonation speed is determined between transducer 3 and 4 by using the time difference between the maximum pressures recorded at these trans-

²SuperSTATE by Combustion Dynamics Ltd is used for solving problems in gas dynamics, chemical equilibrium and chemical kinetics.

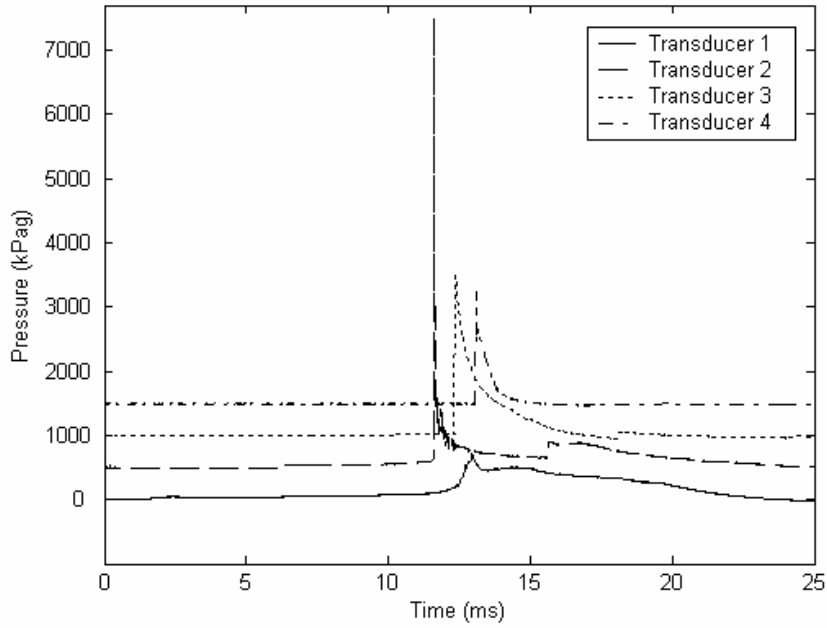


Figure 3.39: Example of pressure histories for an acetylene-air mixture at $\phi = 1.1$. The initial positions are displaced with 5 kPa for each transducer to make the figure more readable.

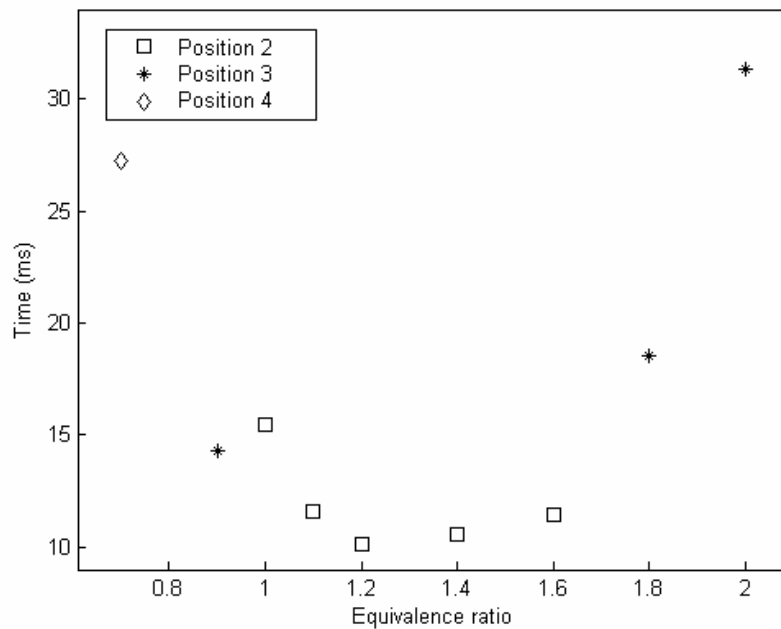


Figure 3.40: The times after ignition at which the maximum recorded pressure occurs. The transducer positions where the pressures are measured are indicated by symbols. Experiments with acetylene-air mixtures in the 5 m steel pipe.

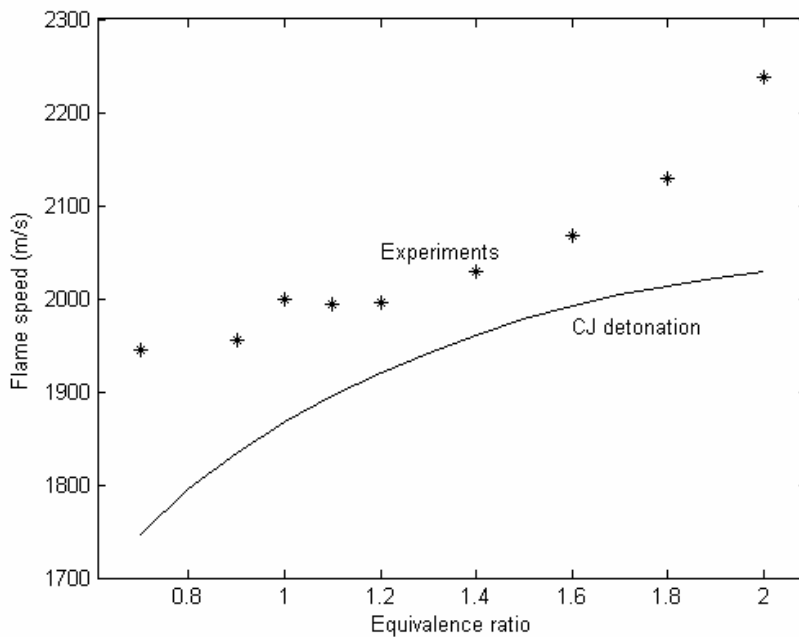


Figure 3.41: Flame speed between transducer 3 and 4 for acetylene-air mixtures in the 5 m steel pipe. The CJ values from SuperSTATE are indicated by the solid line.

ducers. In a detonation, the combustion wave and pressure wave are coupled, and when measuring the speed of the pressure wave the speed of the flame front is also known. CJ values calculated in SuperSTATE are indicated by the solid line in the figure. The experimental results are above the calculated CJ values for all mixtures, but are closest for the most reactive mixtures between $\phi = 1.2$ and 1.4. There is a larger increase of the detonation speed with the equivalence ratio in the experiments than in the calculated CJ values for mixtures above the most reactive mixtures and a smaller decrease below. These could be attributed to the longer run-up distance for these less reactive mixtures, which means that the detonation has not had enough time to reach the CJ state after the overdriven detonation first occurred.

3.3.5 Hydrogen-air mixtures

Experiments with hydrogen-air mixtures were performed in the 2 m and 5 m steel pipes. Pressure were recorded only with the Kistler 7261 transducers, and photodiodes were not used. As for the other fuels, the pipes were horizontally level also in these experiments. Since hydrogen is a lighter gas than air, the gas mixtures in the pipe may therefore have had a higher concentration of hydrogen in the upper part of the pipe.

Sudden pressure increases occasionally occur at all transducers during the experi-

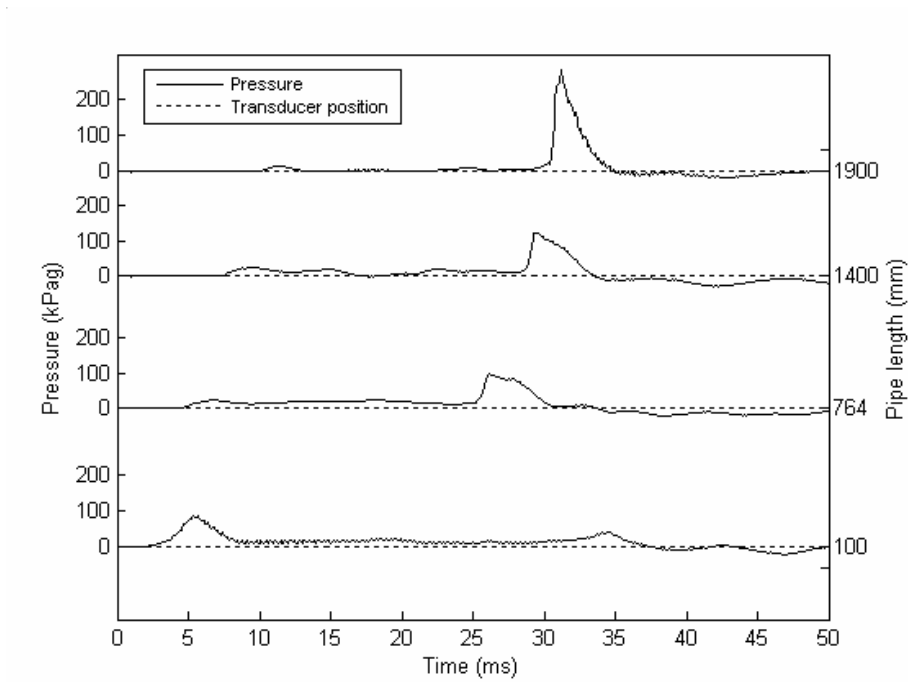


Figure 3.42: Experimental results from an experiment with hydrogen-air mixture at $\phi = 1.1$ in the 2 m steel pipe.



Figure 3.43: Finger shaped flame front.



Figure 3.44: Flame front influenced by gravity.

ments. These pressure peaks could be above 200 kPag. Because these pressure peaks seem independent of the preceding pressure history and of the pressure record at the other transducers, a conclusion can be that these sudden explosions occur within the adapter of the transducer. The transducers have a small volume within the adapter as shown in Figure 3.6, and when the flame in the pipe could penetrate into this volume the mixture could be ignited and explode within the adapter. To illustrate this phenomenon, pressure records for a hydrogen-air mixture with $\phi = 1.1$ are shown in Figure 3.42. For this example, the gas volume in each transducer seems to have exploded. The gas volume in the transducers is ignited when the flame is passing, and the shorter distance between the pressure peaks towards the pipe outlet indicate that the flame propagation in the pipe is accelerated. The first signal from the explosion in the adapter of transducer 4 is recognized 31 ms after ignition. If it is assumed that the gas volume in the adapter is exploding at the time when the flame front reaches the position, an average flame speed can be calculated to 61.3 m/s. The flame propagation is accelerated towards the pipe outlet, and between transducer 2 and 3 the average flame speed is 192.1 m/s, while it has increased to 284.1 m/s between transducer 3 and 4.

3.3.6 Propane-air mixtures, SLR camera

Experiments with propane-air mixtures are performed with the circular plexiglass pipe of 40 mm ID. The experiments have previously been reported by Kristoffersen et al. (2003a) and Johnsen (2003). Pressure is recorded with Kistler 7261 transducers at 100 mm, 710 mm, 1319 mm and 1785 mm from the ignition point. The flame propagation is captured by a Fujifilm Finepix S2 Pro SLR camera.

Instant pictures of the flame front were taken with high shutter speed. Very illus-



Figure 3.45: Flame front disturbed by pressure waves. The flame is probably a vortex ring along the pipe wall.

trative pictures were obtained and some examples are shown here. In Figure 3.43, a finger shaped flame front is shown. This shape will often occur in the initial acceleration of the flame front. Gravity will influence the flame front shape and give a higher flame speed in the upper part of the pipe than in the lower part (Kawakami et al., 1999), as shown in Figure 3.44. In Figure 3.45, a flame front that has been disturbed by a pressure wave is shown. The flame is probably a vortex ring along the pipe wall.

Pictures are also taken with open shutter to capture the whole flame propagation in one picture. Because of the larger pipe diameter, both the overall energy content and t_{wall} are larger in the plexiglass pipe than in the steel pipes, and the pressures will therefore become higher. The photograph for one trial with a propane-air mixture at $\phi = 0.8$ is shown in the lower part of Figure 3.46. The variation in the intensity of light emission along the pipe is determined by extracting the blue colour in the pictures by a MATLAB script. The maximum amount of blue colour in an RGB formatted picture is by definition 255. The amount of blue colour as a fraction of the maximum amount is shown in the upper part of Figure 3.46. Pressure records and a photograph for a stoichiometric mixture and a photograph for a rich mixture with equivalence ratio at 1.2 are shown in Figure 3.47 - 3.49. It is clearly seen that the amount of blue colour is increasing with increasing equivalence ratio. This could be a result of the increased heat release with reactivity of the mixtures, and of an increased amount of more emissive particles in the richer mixtures.

The number of oscillations in the flame propagation also varies with equivalence

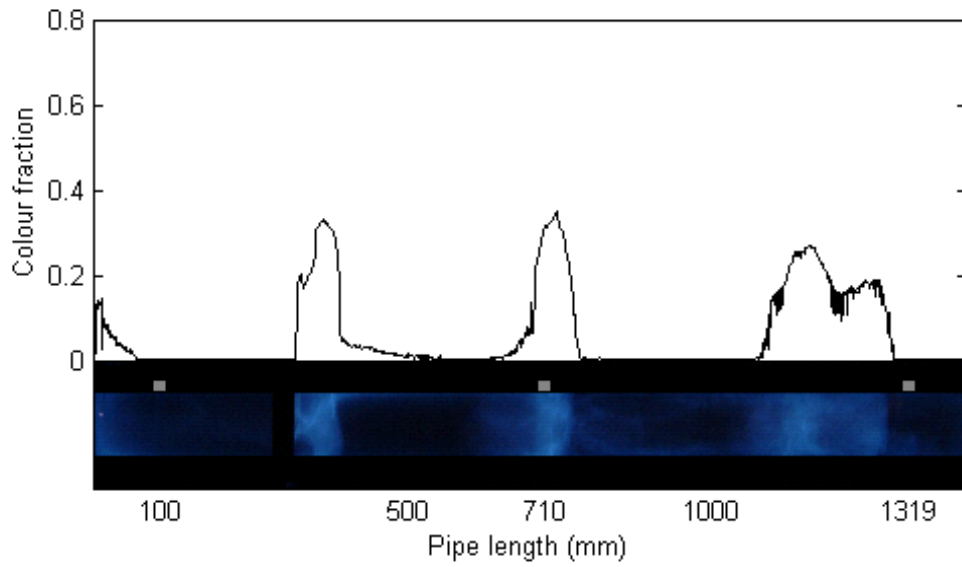


Figure 3.46: Picture captured with open shutter of the flame propagation in the 1.9 m plexiglass pipe for a propane-air mixture at $\phi = 0.8$. The amount of blue colour in the picture is shown in the upper part.

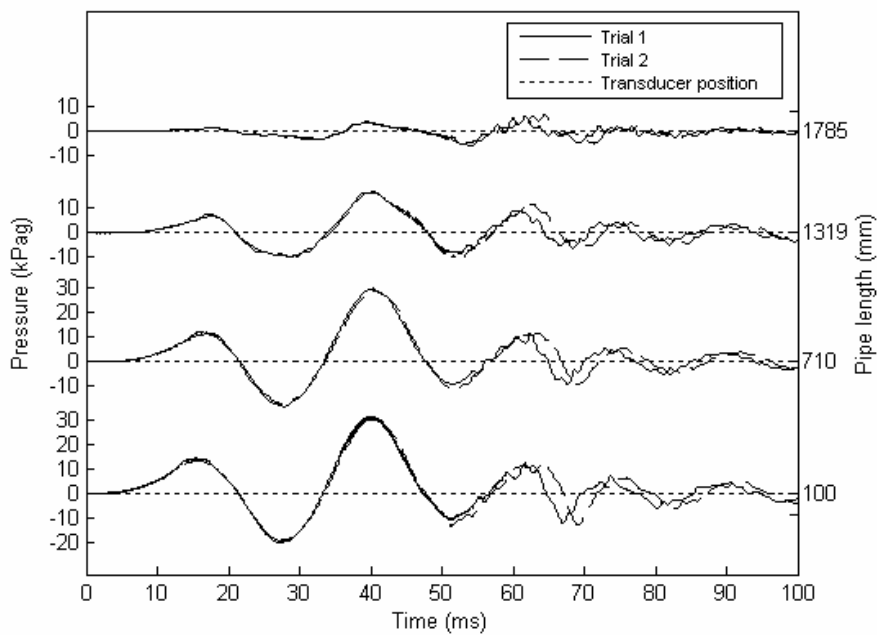


Figure 3.47: Experimental results for a propane-air mixture at $\phi = 1.0$ in the 1.9 m plexiglas pipe.

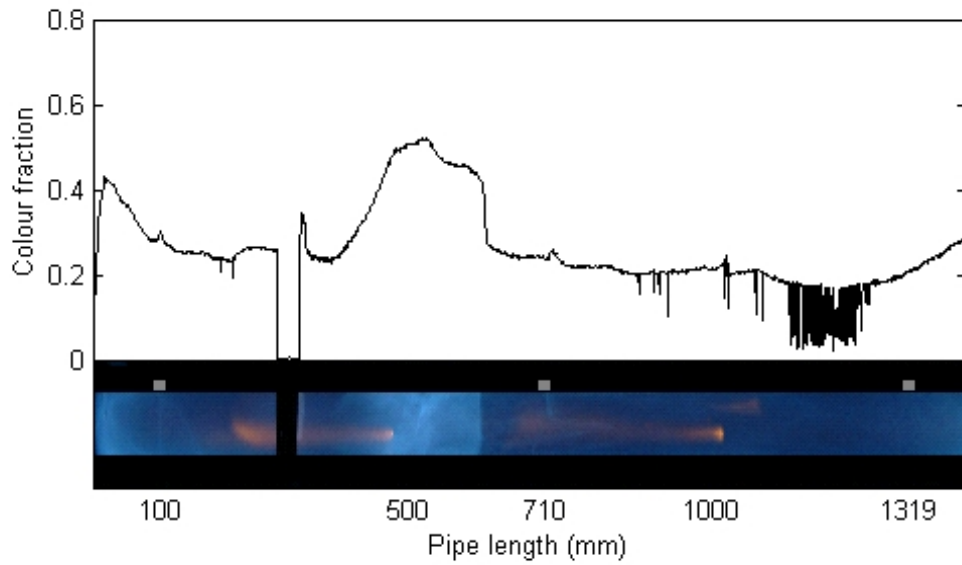


Figure 3.48: Picture captured with open shutter of the flame propagation in the 1.9 m plexiglass pipe for a propane-air mixture at $\phi = 1.0$. The amount of blue colour in the picture is shown in the upper part.

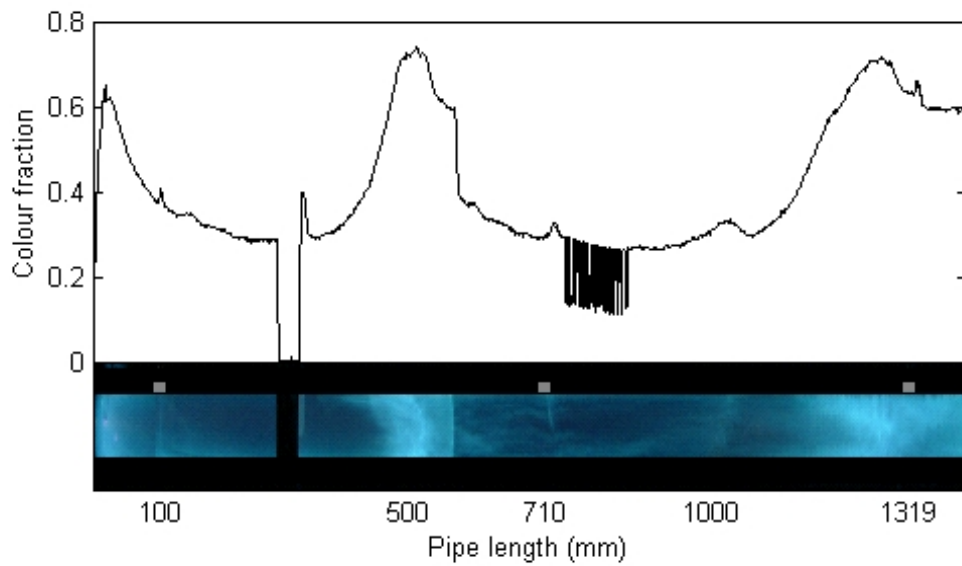


Figure 3.49: Picture captured with open shutter of the flame propagation in the 1.9 m plexiglass pipe for a propane-air mixture at $\phi = 1.2$. The amount of blue colour in the picture is shown in the upper part.

ratio. In the lean mixture, there are three oscillations, in the rich mixture there are two and in the stoichiometric mixture there is only one.

3.3.7 Propane-air mixtures, high speed camera

The flame propagation is also captured by a high speed camera. The experiments are performed in the 40 mm ID circular plexiglass pipe and with propane-air mixtures. Results from experiments with a stoichiometric mixture and a rich mixture at $\phi = 1.2$ are shown in Figure 3.50 and 3.51 respectively.

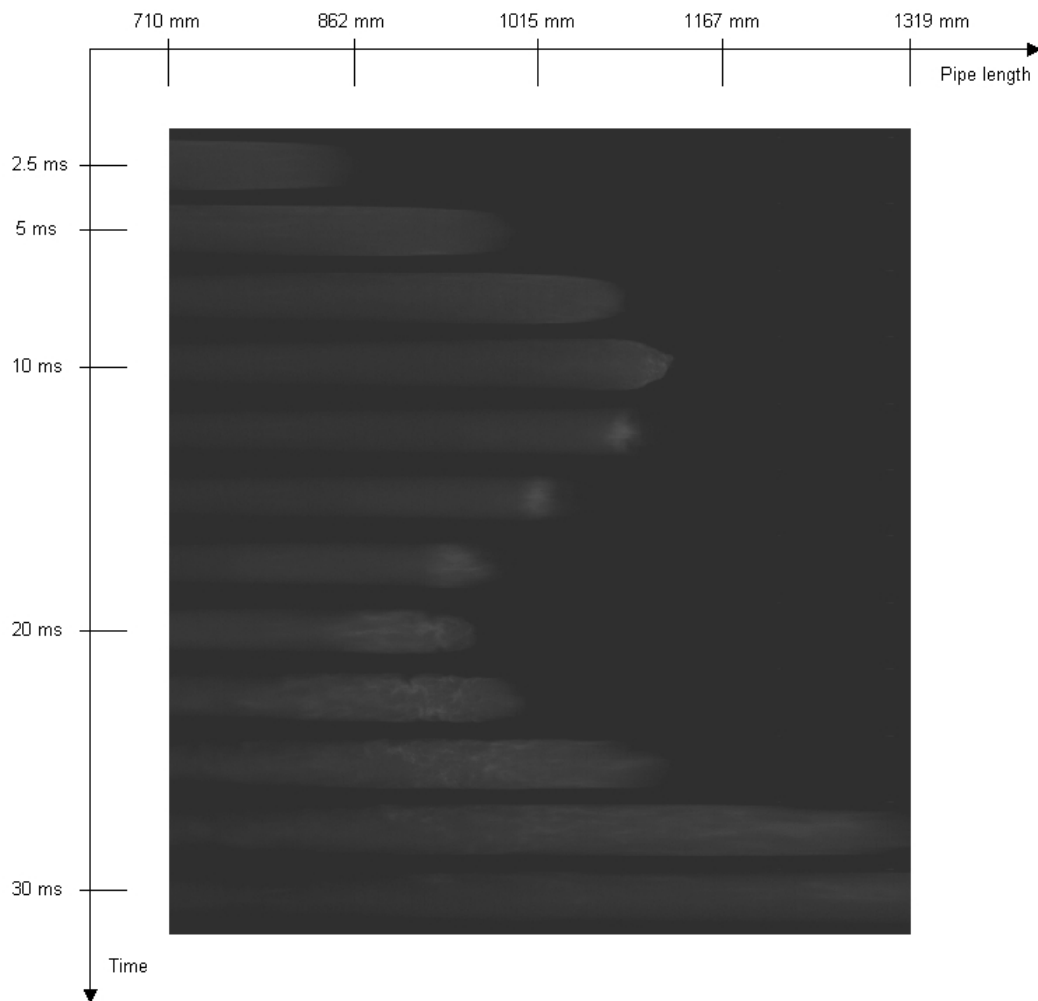


Figure 3.50: Pictures captured with a high speed camera of the flame propagation in the 1.9 m plexiglass pipe. Propane-air mixture at $\phi = 1.0$.

In Figure 3.50, the flame propagation is captured between transducer 2 and 3. The frame rate is 2000 fps, and the time axis is defined from when the flame front first appears on the pictures. A maximum of the flame front position is recognized after around 10 ms. After this, the flame propagates backwards and a small inversion of the

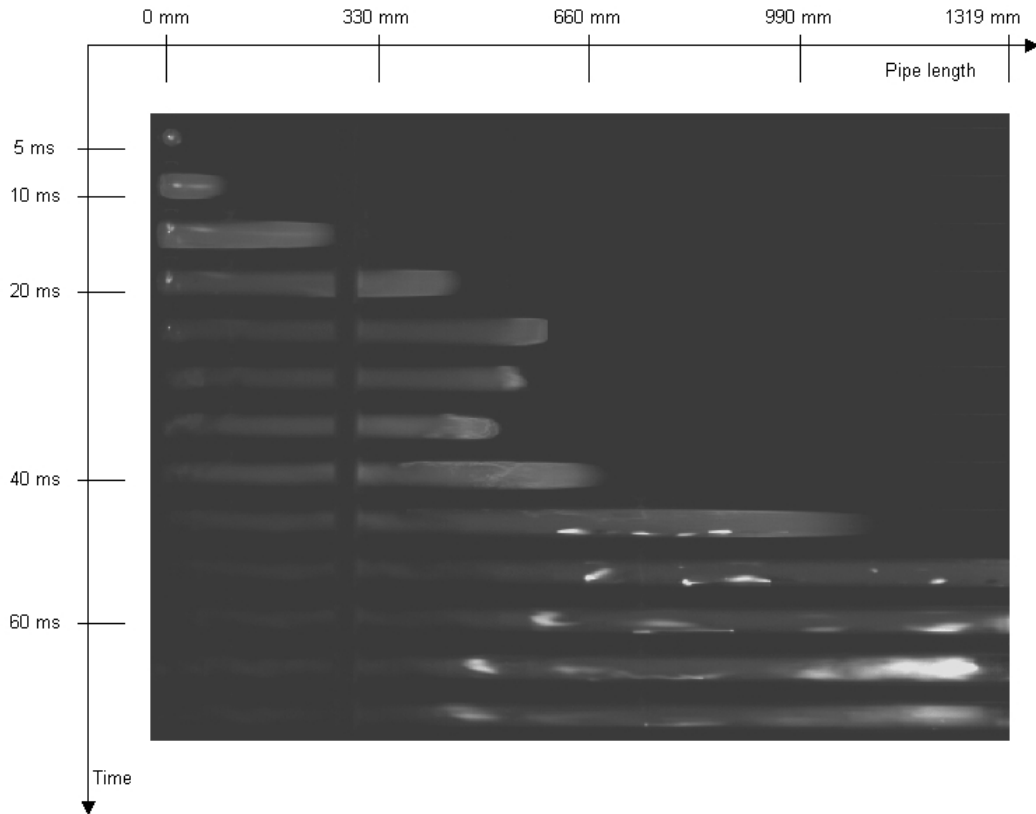


Figure 3.51: Pictures captured with a high speed camera of the flame propagation in the 1.9 m plexiglass pipe. Propane-air mixture at $\phi = 1.2$.

flame front occurs. These mechanisms occur due to interaction of the flame front with the acoustic oscillations in the pipe. The flame front is becoming turbulent and after a minimum flame position is reached at 20 ms the flame propagation is reaccelerated.

In Figure 3.51, the flame propagation in a mixture at $\phi = 1.2$ is captured from the ignition point. The frame rate used was 1000 fps, and the time axis is defined from when the flame front first appears on the pictures. An inversion is also captured for this mixture, but this inversion is the first one that occurs after the ignition and is therefore probably initiated by the quenching of the flame front at the pipe wall. Pressure waves however also seem to have an influence on this inversion. After the minimum flame position is reached, the flame propagation is again accelerated. On the last pictures in Figure 3.51, burning of soot particles is seen by the high light emission. Due to the longitudinal pressure waves in the pipe these particles are transported back and forth in the pipe. The soot particles are a result of the excess of fuel in the original gas mixture. The pictures of the flame propagation taken with the high-speed camera clearly show the oscillating flame propagation.

Chapter 4

Numerical simulations

Numerical simulations have been performed with two codes. The commercial CFD code FLACS by GexCon AS (www.gexcon.com) and a MATLAB version of the Random Choice Method that was developed at Telemark University College, which is called RCMLAB.

4.1 FLACS

The first version of the FLACS (FLame ACcellerator Simulator) code was released in 1986. It is used among others for modeling gas explosions and gas dispersion. FLACS is today in use by several oil and gas companies e.g. Norsk Hydro, Statoil, Total, Dupont and Gaz de France. In this section, some aspects of the modeling in FLACS are described and simulation results are presented and compared to experiments.

FLACS is a 3D finite volume CFD code. In the calculations, a second order central differencing scheme is used for diffusive fluxes and an upward differencing scheme for convective fluxes. The discretised equations are as default solved by BiCGStab in the SIMPLE algorithm on staggered grid. The turbulent flow field is modelled with the $k - \epsilon$ turbulence model, and combustion is modelled by a flame model that uses the results from a burning velocity model as an input parameter.

4.1.1 Flame models in FLACS

The flame thickness is often smaller than the thickness necessary to represent other features of a reactive flow. To fully resolve the flame in numerical simulations therefore requires a grid size that is considerably smaller than for the other regions of the flow. A solution is to use an adaptive grid scheme with a finer resolution in the flame zone. When an adaptive grid scheme is not available, the solution has been to change the

flame structure, and permit use of a coarser grid to reduce the computation time. There are two common ways to change the flame structure, it can be considered as a discontinuity with zero thickness or it can be artificially thickened so that its structure is resolved in the calculation. In FLACS, these two methods are used in the SIF and the β flame models respectively.

β flame model

The β flame model was introduced by Butler and O'Rourke (1976) as a technique for artificially thickening a deflagration wave. The flame thickness is increased by a factor β , by increasing the thermal diffusivity by the same factor. As a consequence, the flame speed is also increased by this factor, but to preserve the original flame speed the chemical reaction rate is reduced by a factor $1/\beta$. The flame speed will be a result of the calculation and is unchanged as long as the flame remains thin compared to the other length scales of the flow field. A disadvantage of this model is that it may change the growth rate of gas dynamical instabilities with wavelengths in the same range as the flame thickness. In the first version of the model the same scaling factor is used everywhere in the calculation domain, however it should differ from unity only around the flame. This disadvantage was indicated by Butler et al. (1981), and they made a new formula, in which the flame is identified by its large temperature gradients:

$$\beta = \max \left(1, \frac{w^2 \Delta^2 |\nabla T|}{l_F \Delta T} \right), \quad (4.1)$$

where l_F is the true flame thickness, Δ is the grid cell size, w the number of cells over which the flame is spread and ΔT the temperature change across the flame.

The model is also discussed by O'Rourke and Bracco (1979). They showed that the β flame model is useful for high Reynolds number and that the Reynolds number is reduced by $1/\beta$ through the transformation. In their simulations, a new model for β was used:

$$\beta = \rho \Lambda / \mu, \quad (4.2)$$

where ρ is the density, μ is the dynamic viscosity and Λ is a constant that is varied between 50, 100 and 150.

The model for β used in FLACS today is given by Arntzen (1998):

$$\beta \propto \frac{4\Delta}{l_T}, \quad (4.3)$$

where l_T is the integral length scale.

The artificial thickening of the flame front is based on the idea from Neumann and Richtmyer (1950) on artificially thickening a shock wave. They introduced artificial dissipative terms into the equations to give the shock a size comparable to or somewhat larger than the cell sizes.

SIF - Simple Interface Flame model

SIF is based on a code introduced by Noh and Woodward (1976) called SLIC (Simple Line Interface Calculation). SLIC is used to define fluid interfaces by an alternating-direction method. Fluid surfaces are represented locally in each control volume, and are defined as a composition of one space dimensional components in each direction. These components are composed of straight lines, perpendicular or parallel to the coordinate directions. The perpendicular lines are preferred, the fluids are then advected one at a time to the neighbouring control volume. When three fluids are present in a Y-like intersection, a T configuration is used. The localization of the interfaces are determined by the volume fractions in the control volume and by testing whether or not the various fluids are found in the control volumes just to the right and just to the left. Three types of variables are used, they are defined as:

f_1, f_2, \dots, f_n	volume fractions within a control volume
IL_1, IL_2, \dots, IL_n	fluid occupation numbers (1 for present, 0 for absent in the control volume to the left)
IR_1, IR_2, \dots, IR_n	fluid occupation numbers (1 for present, 0 for absent in the control volume to the right)

The fluid occupation numbers can be combined in four ways $(IL_i, IR_i) = (0,0), (0,1), (1,0), (1,1)$. When fluids with identical combinations are treated as one single group, there are at most four different fluids in the control volume, which gives six possible configurations, as shown in Figure 4.1.

The SLIC code is entirely one-dimensional and is relatively easily extended to two and three dimensions. This is possible by the alternating-direction feature by which the interfaces are calculated one-dimensional for each coordinate direction. The calculations are performed independently in each direction, and it has been emphasized that it is this freedom that gives the method its power. The one-dimensional nature makes it possible to incorporate any one space dimensional method for advancing the interface. It has also been pointed out that false diffusion is not possible, and that this is avoided by defining unique "pictures" for each control volume and further that the "nearest" fluid exists first.

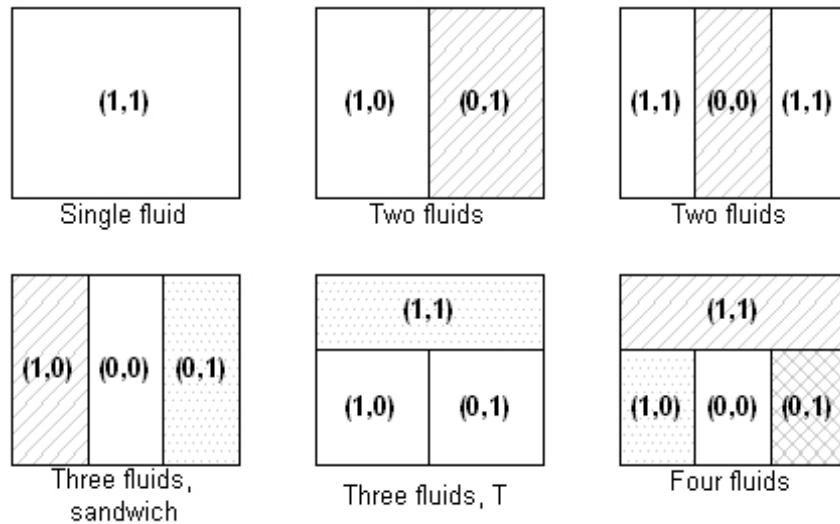


Figure 4.1: The six possible configuration types for fluid interfaces in a control volume (Noh and Woodward, 1976).

The SLIC model has also been used to track flame fronts. Then the flame front is regarded as the interface between burnt and unburnt gas, where the reactants are transformed to products. Chorin (1980) mentioned five types of interfaces between the two gases: no interface, vertical interface, horizontal interface, corner and thin finger. For a thin finger, the location of the flame fronts are random and calculated each half timestep for the horizontal and vertical directions by use of two independent van der Corpus algorithms. Chorin (1980) used the Huyghens principle to calculate the motion of the flame front. A number of points are defined on the flame front and from each of these the flame expands with the burning velocity. The summation of the new expanded volumes and the original burnt volume forms the new volume of burnt gas. The method was similarly used by Sethian (1984) and Ghoniem et al. (1982).

Bielert et al. (1996) compared the methods of Noh and Chorin and concluded that the SLIC algorithm could give significant nonphysical deformations of the interface. Instead they used a method called Volume of Fluid (VOF) where the interface is also represented by skew lines.

4.1.2 Burning velocity

Modelling of the burning velocity is divided into three models in FLACS (Arntzen, 1998). Initially there is a laminar burning velocity model. When instability mechanisms enhance the burning rate, a quasi laminar burning velocity is calculated. The laminar burning velocity is then multiplied by an enhancement factor, which increases the burning velocity due to the instabilities. The enhancement factor is a function of

flame radius and gas mixture and the quasi laminar burning velocity is defined as:

$$S_{QL} = S_L (1 + ar)^{1/2}, \quad (4.4)$$

where r is the flame radius and a is a constant. When using the SIF model, some of the flame wrinkling is simulated and the enhancement factor should be lower than when using the β model.

Two expressions are used for the calculation of the turbulent burning velocity in FLACS. They are derived from a correlation developed by Bray (1990). The first one is given by:

$$S_{T1} = 1.8 S_L^{0.784} u'^{0.412} l_T^{0.196} \nu^{-0.196}, \quad (4.5)$$

where u' is the turbulent intensity, l_T is the integral length scale and ν is the kinematic viscosity. This expression is not satisfactory at low turbulent intensities, $u' \rightarrow 0$. Equation 4.5 then gives $S_T \rightarrow 0$, when it should give $S_T \rightarrow S_L$. Arntzen (1998) therefore made a correlation by adding the product of Equation 4.5 and the square root of u'/S_L to the laminar burning velocity:

$$S_{T2} = 0.96 S_L^{0.284} u'^{0.912} l_T^{0.196} \nu^{-0.196} + S_L. \quad (4.6)$$

Equation 4.6 gives a too large influence of the integral length scale and is only used for low values of the turbulent intensity. The burning velocity is always chosen as the maximum of the turbulent and the quasi laminar burning velocities.

4.1.3 Turbulent viscosity

The effective viscosity used in FLACS is equal to the sum of the laminar and turbulent viscosities (Arntzen, 1998):

$$\mu_{\text{eff}} = \mu_L + \mu_T \quad (4.7)$$

In FLACS, the Boussinesq eddy viscosity model is used to model the turbulent viscosity:

$$\mu_T = 0.09 \rho \frac{k^2}{\varepsilon}, \quad (4.8)$$

where k is the turbulent kinetic energy and ε is the dissipation rate of turbulent kinetic energy from the $k - \varepsilon$ model. Simulations have been performed in which the effective viscosity is calculated from the $k - \varepsilon$ model in the default way, and with constant values

of k and ε at their initial values, which in FLACS is 10^{-3} for both. This involves a constant turbulent kinematic viscosity:

$$\nu_T = \frac{\mu_T}{\rho} = 0.09 \frac{k^2}{\varepsilon} = 9e^{-5} \text{ m}^2/\text{s} \quad (4.9)$$

4.1.4 Courant numbers

In FLACS, two Courant numbers are used (FLACS-98 User's Guide). The first number, CFLC (Courant-Friedrich-Levy, speed of sound), is based on the speed of sound, and the time step length is determined by:

$$\Delta t = \frac{CFLC \times \Delta}{c}, \quad (4.10)$$

where Δ is the smallest grid cell size and c is the speed of sound. The default value for CFLC is 5.0. The second number, CFLV, is based on fluid flow velocity and has a default value of 0.5. The most stringent criterion for the time step length is always chosen. When CFLV is used, this also involves comparison of the ratio between the grid cell size and the flow velocity in all directions.

4.1.5 Simulations

When simulating pressure oscillations in pipes with FLACS, it was found that the amplitude of the oscillations was reduced considerably. It was first assumed that this reduction was caused by a too large production of turbulent viscosity in the burnt mixture behind the flame. Three new models for the generation of turbulent viscosity were therefore implemented. The first one had no generation of turbulent viscosity at all, the second had generation of turbulent viscosity only ahead of the flame front, i.e. only when the concentration of products was below 5%. In the last model, generation of turbulent viscosity in the flame was also included, i.e. generation up to a concentration of products of 90%. In addition to these models, three ways of generating turbulent viscosity in the original code were used. These include generation by the default model, limited generation by keeping the values of k and ε at their initial values and by skipping generation of turbulent viscosity along the wall by not using wall functions. The models are summarized in Table 4.1.

Table 4.1: Models for generation of turbulent viscosity.

1	the default model	
2	generation only ahead of the flame	limit at PROD = 5%
3	generation ahead of and in the flame	limit at PROD = 90%
4	no generation	
5	$k = \varepsilon = 10^{-3}$	initial values
6	no wall function	WALL = 0

The geometry used is a 2 m long square pipe with inner pipe width of 40 mm. The pipe is closed at one end and open at the other, with ignition at the closed end. Four monitor points are placed at the centre line of the pipe at distances 0.1 m, 0.76 m, 1.4 m and 1.9 m from the closed end. The size of the simulation volume is $6 \times 2 \times 2 \text{ m}^3$ with start position in (0,-2,-2). The pipe is designed from position (0,0,0). The grid in the volume outside the pipe is stretched with a factor of 1.4. The boundary conditions are PLANE_WAVE except at the low x-boundary where EULER is used. In the pipe, the grid size in the x-direction is 20 mm. In the two other directions, the grid size is varied. These non-cubic control volumes deviate from GexCon's recommendations and can affect the simulation results. The burning velocity model in FLACS seems to give a too large value for the burning velocity in a pipe, and in the following simulations the burning velocity is frozen at 0.44 m/s, which is the laminar burning velocity for the stoichiometric propane-air mixture used (Law, 1993). The three parameters, 1) CFLC, 2) number of grid cells in the cross section and 3) the model for generation of turbulent viscosity, are varied.

CFLC

CFLC is varied between 0.1 and 10. In Figure 4.2, the pressure values at the four monitor points are shown for simulations with 11 grid cells in each direction in the cross section and with the default model for generation of turbulent viscosity. For the two highest values of CFLC, the amplitude of the second pressure peak is reduced significantly compared to the simulation when $CFLC = 1$. For $CFLC = 2$ there is a smaller reduction of the second pressure peak. The maximum pressure at the second peak for the six values of CFLC tested are shown in Figure 4.3. The largest pressure is obtained for $CFLC = 1$. A CFLC value of 1, or perhaps also smaller, should therefore be used.

Number of grid cells

The second parameter tested is the number of grid cells in each direction in the pipe cross section. Six grid sizes are used and in Table 4.2 they are summarized with the

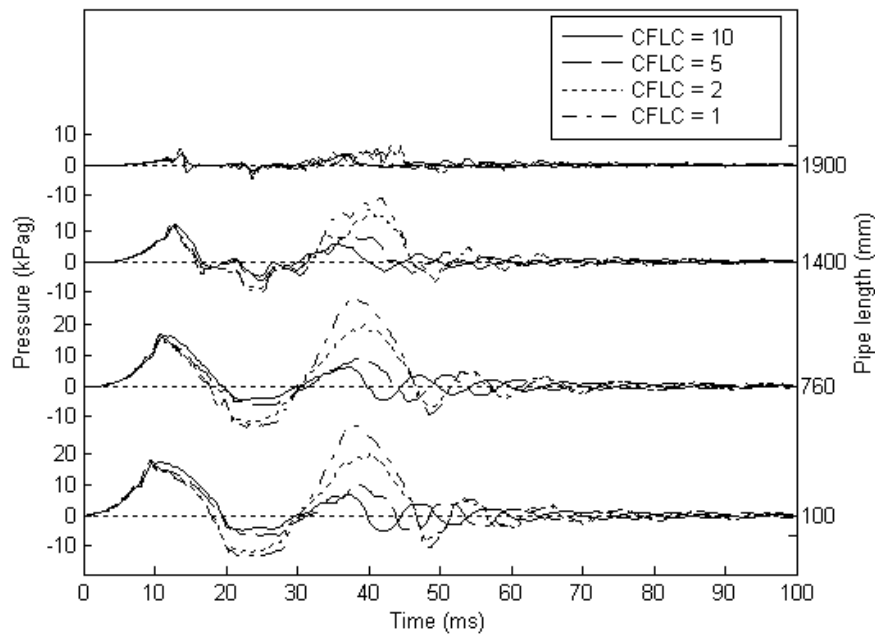


Figure 4.2: Simulations in FLACS with a stoichiometric propane-air mixture for various CFLC numbers. 11 grid cells are used in each direction of the cross section and the default model for generation of turbulent viscosity is applied.

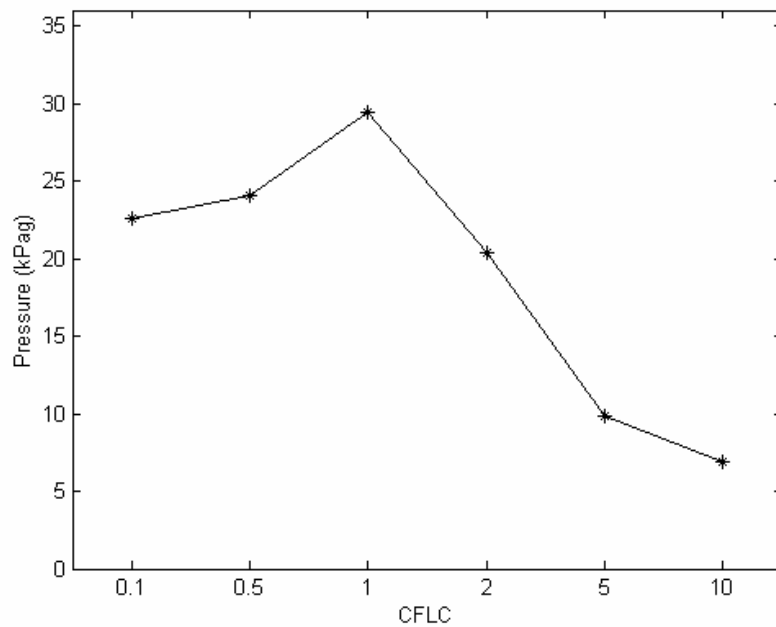


Figure 4.3: Maximum pressure at the second peak for various CFLC numbers. Simulations in FLACS with a stoichiometric propane-air mixture. 11 grid cells are used in each direction in the cross section and the default model for generation of turbulent viscosity is applied.

Table 4.2: Number of grid cells used in each direction of the pipe cross section and the associated grid sizes.

Number of grid cells	Grid size
3	13.3 mm
5	8.0 mm
7	5.7 mm
9	4.4 mm
11	3.6 mm
13	3.1 mm

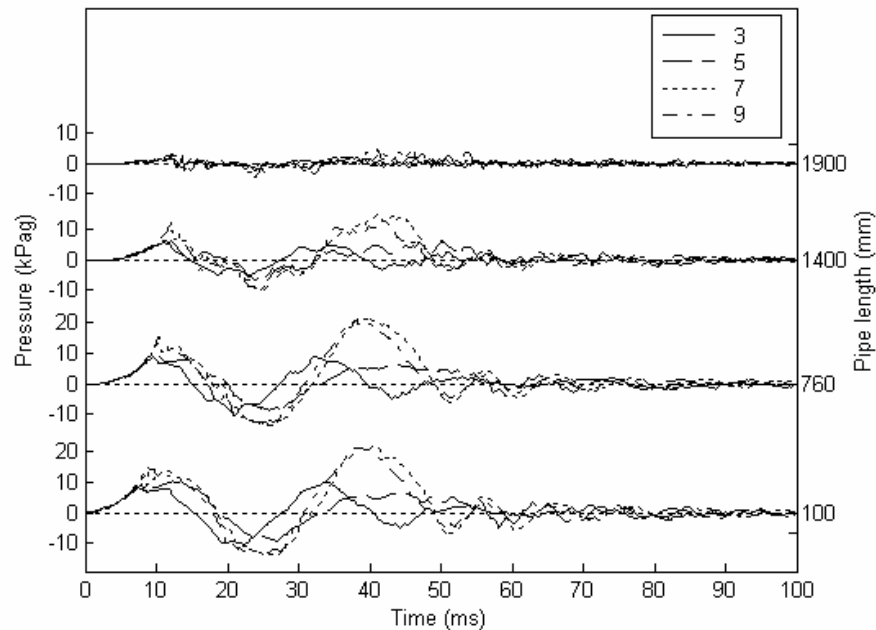


Figure 4.4: Simulations in FLACS with a stoichiometric propane-air mixture for various numbers of grid cells in the pipe cross section. $CFLC = 0.5$ and the default model for generation of turbulent viscosity is applied.

number of grid cells. In Figure 4.4, pressure histories with the four largest grid sizes are shown for simulations with the default model for generation of turbulent viscosity and $CFLC = 0.5$. There are clear reductions of the amplitude for the second pressure peak for the two largest grid sizes compared to the two others, but there are only minor differences between the pressure values when 7 or 9 grid cells are used in the cross section. The same conclusion can be drawn from Figure 4.5 where the maximum pressure of the second peak for all grid sizes used is given. Two criteria could therefore be defined; the grid size should not exceed 5.7 mm or the number of grid cells in the cross section should exceed 7. It would be necessary to emphasize that these criteria are tested only for one pipe width of 40 mm.

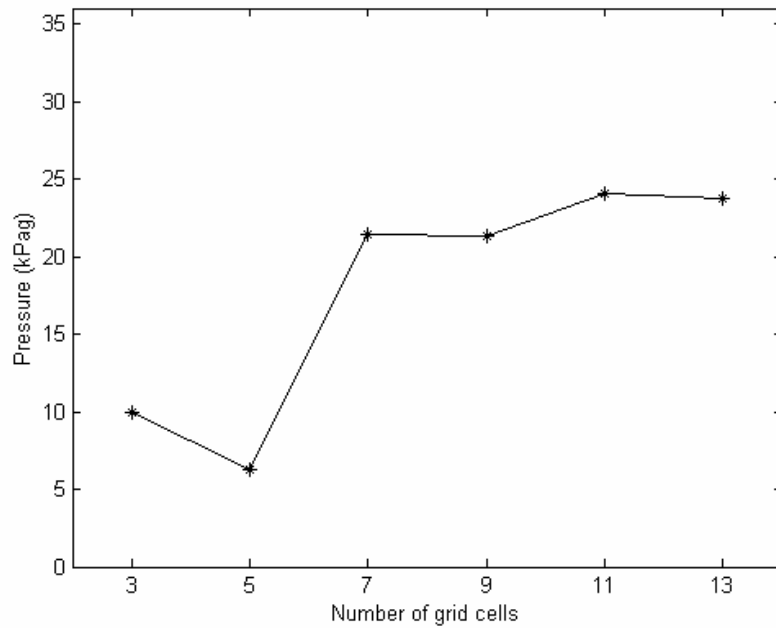


Figure 4.5: The maximum pressure at the second peak for various numbers of grid cells in the pipe cross section. Simulations in FLACS with a stoichiometric propane-air mixture. CFLC = 0.5 and the default model for generation of turbulent viscosity is applied.

Models for generation of turbulent viscosity

The maximum pressures of the second pressure peak, obtained for the 6 models for generation of turbulent viscosity, are shown in Figure 4.6 for various values of CFLC and with 11 grid cells in each direction in the pipe cross section. In Figure 4.7, the same pressure peak is shown for various numbers of grid cells and CFLC = 0.5.

For the three models (1, 2 and 3) with generation of turbulent viscosity, an equal behavior is seen, with two clusters of pressure values. For the various values of CFLC, shown in Figure 4.6, the division between the clusters is for CFLC = 2 or lower, and for the grid resolution shown in Figure 4.7, the division is for 7 grid cells or more in the pipe cross section. In the simulations with the three models (4, 5 and 6) where none or only minor amounts of turbulent viscosity are generated, the maximum pressure at the second pressure peak is generally larger than for the first models. This indicates that the turbulent viscosity will reduce the pressure values. However it seems like the influence of generation of turbulent viscosity on the amplitude of the pressure oscillations is more important for values of CFLC above 2. For the various grid resolutions, there is a clear division into two clusters for all models. For the largest grid size, there is practically no changes in the pressure value for the different

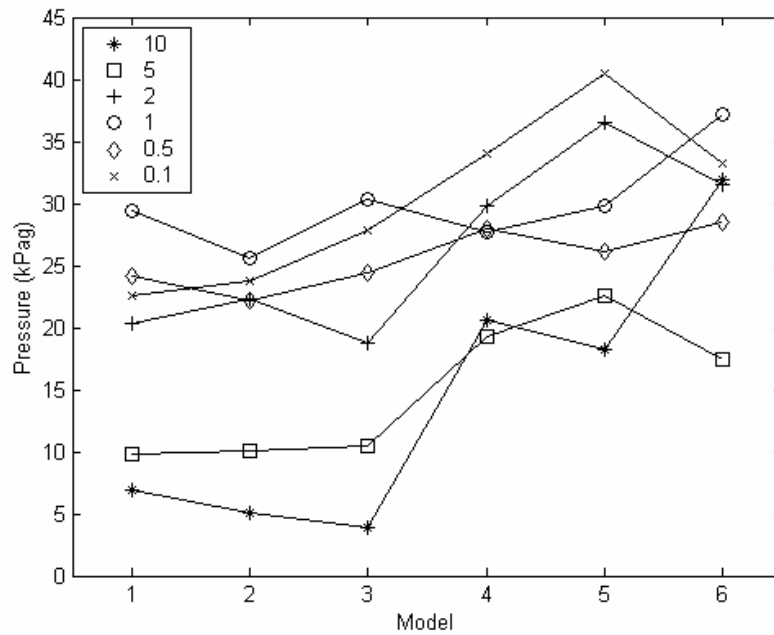


Figure 4.6: Maximum pressure at the second pressure peak for various CFLC numbers and models for generation of the turbulent viscosity (Table 4.1). Simulations in FLACS with a stoichiometric propane-air mixture and with 11 grid cells in each direction in the pipe cross section.

models, while for the other grid sizes there are generally lower pressures when turbulent viscosity is generated.

Combustion modeling

As shown, there should be at least 7 grid cells in the pipe cross section and the CFLC should be less or equal to 1. These two parameter values are used in a simulation to test the combustion model when the burning velocity is determined from the default burning velocity model. The results of this simulation are shown in Figure 4.8 where the pressure histories at each monitor point are given by solid lines and the flame arrival times at the monitors are given by solid circles. The flame front reaches the fourth monitor point after 17 ms, which gives an average flame speed of 112 m/s. The results can be compared to similar experimental results in a circular pipe of 40 mm ID, which is shown in Figure 3.47. The flame speed is much higher than in the experiments and this strong flame acceleration generates a pressure wave that is more than double the experimental pressures. This result indicates that the initial flame acceleration is too strong in the FLACS code. The reason could be that the enhancement factor in the quasi laminar burning velocity model is determined for spherical propagation

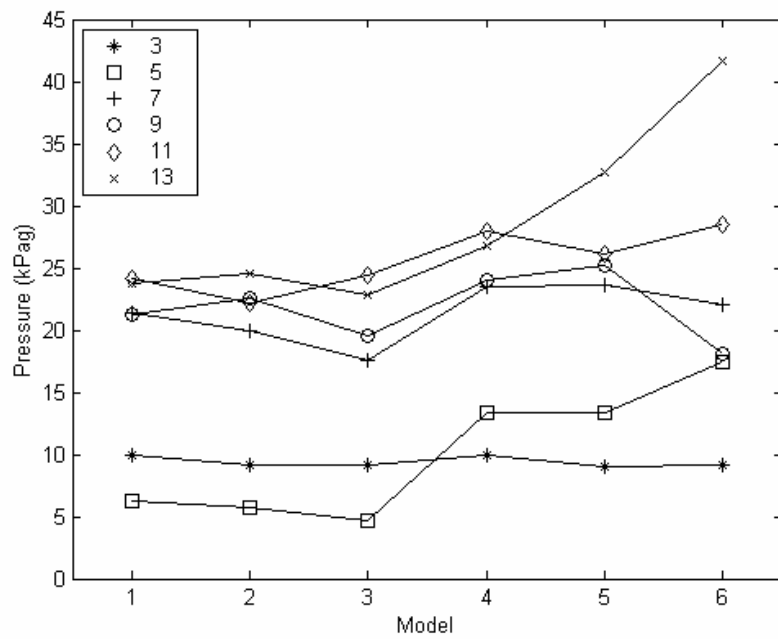


Figure 4.7: Maximum pressure at the second pressure peak for various numbers of grid cells in each direction in the pipe cross section and for various models for generation of the turbulent viscosity (Table 4.1). Simulations in FLACS with a stoichiometric propane-air mixture and with $CFLC = 0.5$.

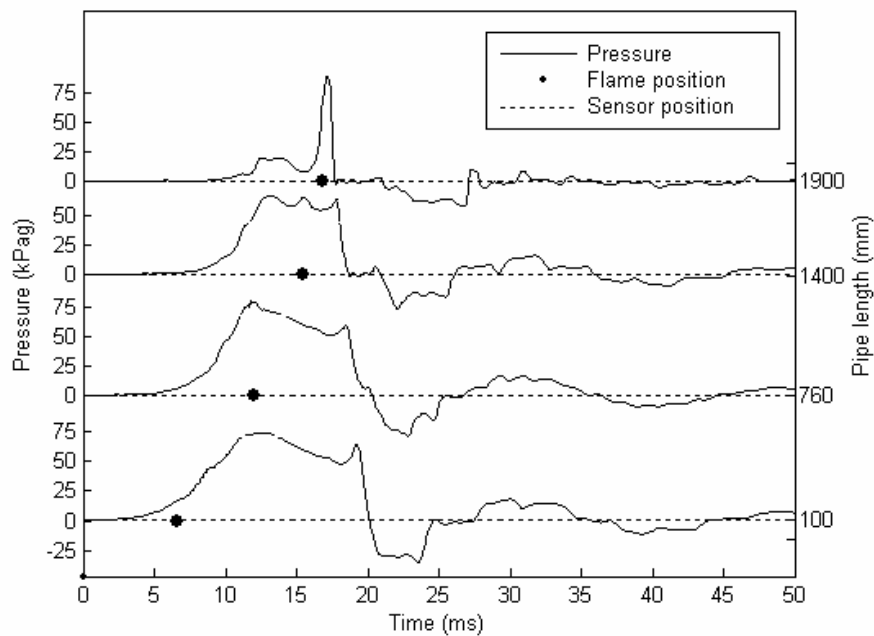


Figure 4.8: Test of the combustion model with 7 grid cells in each direction of the cross section and with $CFLC = 1$. Simulations in FLACS with a stoichiometric propane-air mixture.

and is therefore not suitable for the elongated hemispherical flame propagation in a pipe due to the dependence on the flame radius. For the very large surface area to gas volume ratio that is present in this small pipe diameter, heat loss is expected to reduce the flame speed. These effects are not completely included in the simulations, and can therefore also be a part of the explanation for the too high flame speed in the simulations compared with the experiments.

4.1.6 Summary FLACS

Simulations have been performed in FLACS to test how the gas dynamical models could handle acoustic oscillations in a pipe and how the combustion model handles flame propagation from the closed end of a pipe.

By comparing the simulation results to experiments it has been shown that a minimum of 7 grid cells in each direction of the pipe cross section and a CFLC ≤ 1 are necessary to handle the acoustic oscillations.

The initial flame propagation in pipes is too high compared to experiments and the enhancement factor in the quasi laminar burning velocity model should be reduced for such geometries. Heat loss will also affect the flame propagation and should be completely included in simulations of flame propagation in pipes.

4.2 Random Choice Method

A MATLAB version of the Random Choice Method (RCM) was developed at Telemark University College. The code is called RCMLAB and is presented by Bjerketvedt and Mjaavatten (2001) and by Bjerketvedt et al. (2002). In this section, the principles of RCM are described together with advances in the code. Simulation results are presented and compared to experimental results. The RCM described here is for solving a 1D non-stationary unsteady flow of a compressible gas with combustion.

The RCM was originally introduced by Glimm (1965). The method was further developed by Chorin (1976) who also extended the RCM to combustion problems (Chorin, 1977). More details and extensions of the method are presented by Saito and Glass (1979), Gottlieb (1986) and Toro (1999).

The main advantage of the RCM is its unique capability for predicting complex wave interactions while maintaining the discontinuities of shock waves and contact surfaces. Such discontinuities are often smeared over several cells in other more traditional CFD codes. However, the randomness of the RCM introduces numerical noise that is more obvious for smooth waves such as rarefaction waves. This noise is dimin-

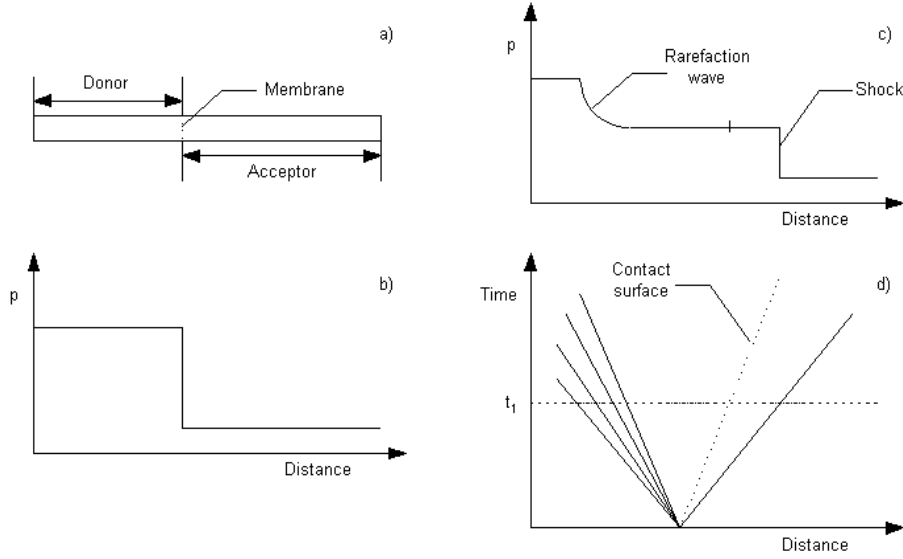


Figure 4.9: Principles for a shock tube.

ished when the number of computational cells is increased. The principle of the RCM is to solve the Riemann problem in the domain between two neighboring grid points.

4.2.1 The Riemann problem for the Euler equations

The Riemann problem is a solution to the one-dimensional time-dependent Euler equations:

$$\frac{\partial \rho}{\partial t} + \frac{\partial (\rho u)}{\partial x} = 0, \quad (4.11)$$

$$\frac{\partial (\rho u)}{\partial t} + \frac{\partial (\rho u^2 + p)}{\partial x} = 0, \quad (4.12)$$

$$\frac{\partial E}{\partial t} + \frac{\partial (u(E + p))}{\partial x} = 0, \quad (4.13)$$

where ρ is the density, t is the time, u is the velocity, x is the position, p is the pressure and E is the total energy per unit volume, with the following initial conditions:

$$U(x, 0) = \left\{ \begin{array}{l} U_l \text{ if } x < 0 \\ U_r \text{ if } x > 0 \end{array} \right\}, \text{ where } U = \begin{bmatrix} \rho \\ u \\ p \end{bmatrix} \quad (4.14)$$

The initial Riemann problem consists of two constant states separated by a discontinuity at $x = 0$. The left side has the initial conditions U_l and the right side the initial

conditions U_r . The Riemann problem is a generalization of the shock tube problem. In a shock tube, a high pressure section is separated from a section with lower pressure by a membrane, as shown in Figure 4.9 a). When the membrane is broken, a shock wave is propagating into the low pressure section followed by a contact discontinuity, while a rarefaction wave is expanding the gas in the high pressure section. Pressure profiles before the membrane is broken and at a time after the membrane is broken are shown in Figure 4.9 b) and c) respectively. At the contact surface, the velocity u_* and the pressure p_* must be the same for the shocked gas and the expanded gas. In the Riemann problem, non-zero initial velocities at each side of the discontinuity are allowed. Four different wave patterns are then possible for a Riemann problem. As shown in Figure 4.10, these could be: a) left rarefaction wave, contact surface and right shock wave, b) left shock wave, contact surface and right shock wave, c) left rarefaction wave, contact surface and right rarefaction wave and d) left shock wave, contact surface and right rarefaction wave. Along the x-axis, four different constant states are considered. They are separated by the three waves that are presented in each wave pattern. The two regions between the left and right pressure waves are called the Star Region. These two regions are separated by a contact surface and the pressure p_* and velocity u_* are equal on each side of this contact surface. The density, however takes on two constant values ρ_{*l} and ρ_{*r} . In the Riemann problem, the states to the left and to the right are known and it is necessary to find a solution for p_* , u_* , ρ_{*r} and ρ_{*l} .

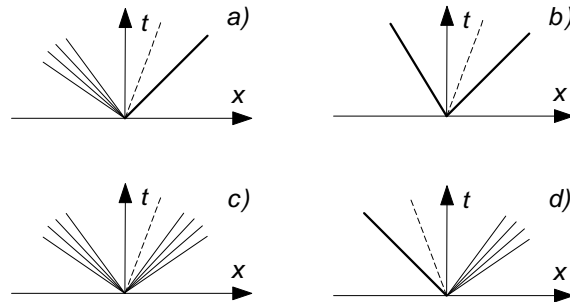


Figure 4.10: Possible wave patterns of a Riemann problem.

A solution procedure for u_* and p_* is presented by Toro (1999). Functions are first developed for the four wave patterns, where the states on each side of a shock wave are connected by using the Rankine-Hugoniot equations and the states on each side of a rarefaction wave are connected by using the isentropic relation. The pressure p_* can be found by solving the equation:

$$f(p_*, U_l, U_r) = f_l(p_*, U_l) + f_r(p_*, U_r) + \Delta u = 0, \quad (4.15)$$

where $\Delta u = u_r - u_l$, and the functions f_l and f_r are given by:

$$f_l(p_*, U_l) = \left\{ \begin{array}{ll} (p_* - p_l) \left[\frac{A_l}{p_* + B_l} \right]^{\frac{1}{2}} & \text{if } p_* > p_l \text{ (shock)} \\ \frac{2c_l}{(\gamma-1)} \left[\left(\frac{p_*}{p_l} \right)^{\frac{\gamma-1}{2\gamma}} - 1 \right] & \text{if } p_* \leq p_l \text{ (rarefaction)} \end{array} \right\}, \quad (4.16)$$

$$f_r(p_*, U_r) = \left\{ \begin{array}{ll} (p_* - p_r) \left[\frac{A_r}{p_* + B_r} \right]^{\frac{1}{2}} & \text{if } p_* > p_r \text{ (shock)} \\ \frac{2c_r}{(\gamma-1)} \left[\left(\frac{p_*}{p_r} \right)^{\frac{\gamma-1}{2\gamma}} - 1 \right] & \text{if } p_* \leq p_r \text{ (rarefaction)} \end{array} \right\}, \quad (4.17)$$

where γ is the ratio between heat capacities at constant pressure and constant volume, c_l and c_r are the speed of sound at each side and the constants A_l, B_l, A_r, B_r are given by:

$$A_l = \frac{2}{(\gamma + 1) \rho_l}, \quad (4.18)$$

$$B_l = \frac{(\gamma - 1)}{(\gamma + 1)} \rho_l, \quad (4.19)$$

$$A_r = \frac{2}{(\gamma + 1) \rho_r}, \quad (4.20)$$

$$B_r = \frac{(\gamma - 1)}{(\gamma + 1)} \rho_r. \quad (4.21)$$

The velocity u_* for a left wave is given by:

$$u_* = u_l - f_l(p_*, U_l), \quad (4.22)$$

while the velocity u_* for a right wave is given by:

$$u_* = u_r + f_r(p_*, U_r). \quad (4.23)$$

The velocity can also be determined as a mean velocity:

$$u_* = \frac{1}{2} (u_l + u_r) + \frac{1}{2} [f_r(p_*) - f_l(p_*)]. \quad (4.24)$$

4.2.2 Solution of the Riemann problem by the RCM

The computational domain is first discretised into a number of cells of size $\Delta x = x_{i+\frac{1}{2}} - x_{i-\frac{1}{2}}$. The method assumes a piecewise constant distribution of data within each cell as shown in Figure 4.11, with discontinuities at the midpoint positions, i.e. at $i \pm 0.5$. The Riemann problem is solved in the domain between two neighbouring grid points, the left domain $[i, i + 0.5)$ and the right domain $[i + 0.5, i + 1)$.

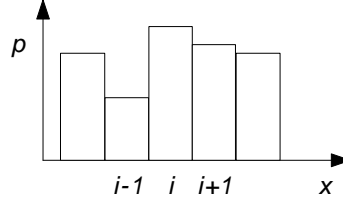


Figure 4.11: Piecewise constant distribution.

The Riemann problem must be solved by iteration and the Newton-Rhapson procedure is used. An initial guess for p_* is determined by:

$$p_0 = \max(p_{ig}, \min(p_l, p_r)), \quad (4.25)$$

where p_{ig} is given by:

$$p_{ig} = \frac{1}{2}(p_l + p_r) - \frac{1}{8}(u_r - u_l)(\rho_l + \rho_r)(c_l + c_r) \quad (4.26)$$

From p_0 the wave pattern is determined by comparing p_0 to the values on each of the outer sides of the waves. The functions f_l and f_r and their derivatives are calculated from Equations 4.16 and 4.17. The values of the functions are summarized by introducing:

$$f(p) = f_l(p) + f_r(p) + u_r - u_l, \quad (4.27)$$

$$f'(p) = f'_l(p) + f'_r(p) \quad (4.28)$$

In the Newton-Rhapson procedure, a new value for p_* is calculated by:

$$p_1 = p_0 - \frac{f(p_0)}{f'(p_0)}. \quad (4.29)$$

The iteration continues until the relative pressure change between two iterations (k) defined as CHA is below a tolerance value (TOL):

$$CHA = \frac{|p_k - p_{k-1}|}{\frac{1}{2}(p_k + p_{k-1})} < TOL = 10^{-6}. \quad (4.30)$$

The velocity u_* is then determined by Equation 4.24. The values for ρ_* can now be determined. If the wave is a shock wave, the density is calculated according to:

$$\rho_{*d} = \rho_d \left(\frac{\frac{p_*}{p_d} + \frac{\gamma_d - 1}{\gamma_d + 1}}{\frac{\gamma_d - 1}{\gamma_d + 1} \frac{p_*}{p_d} + 1} \right), \quad (4.31)$$

where d denotes the wave direction, either left (l) or right (r). The density for the rarefaction waves is determined from the isentropic law:

$$\rho_{*d} = \rho_d \left(\frac{p_*}{p_d} \right)^{\frac{1}{\gamma_d}} \quad (4.32)$$

Sampling points are found from the Van der Corput pseudo random number sequence, because it is known that this sequence gives better results than when using completely random numbers. A number $\zeta \in [0, 1]$ in the sequence is determined by:

$$\zeta(n) = \sum_{i=0}^m A_i \times 2^{-(i+1)}, \quad (4.33)$$

where m and A_i is given by an expression for the natural numbers:

$$n = \sum_{i=0}^m A_i \times 2^i. \quad (4.34)$$

The first 10 numbers in the sequence will be 0.5, 0.25, 0.75, 0.125, 0.625, 0.375, 0.875, 0.0625, 0.5625, 0.3125. At a given time step, the same ζ is used for all grid cells. The solution in each domain between neighbouring grid points is taken at the sampling points ($i + \zeta$), as shown by the sampling scheme in Figure 4.12. The solution is placed into grid point ($i + 1$) for the first half time step and into grid point (i) for the second half time step. The length of the time step is determined by the Courant-Friedrich-Levy criterion:

$$\Delta t = C \frac{\Delta x}{|u| + c}, \quad (4.35)$$

where the Courant number C is given the value $C = 0.45$.

4.2.3 Combustion model

The combustion model is based on the Rankine-Hugoniot relations. The state (p_{*u}, ρ_{*u}) ahead of the combustion wave and the state (p_{*b}, ρ_{*b}) behind the combustion wave are related by a quasi one-dimensional burning velocity, S [m/s], as defined by the equation for the Rayleigh line:

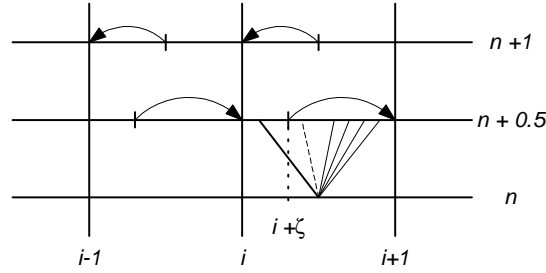


Figure 4.12: Sampling scheme of RCM.

$$-(\rho_u S)^2 = \frac{(p_{*b} - p_{*u})}{\frac{1}{\rho_{*b}} - \frac{1}{\rho_{*u}}}. \quad (4.36)$$

Since the calculations are performed one-dimensionally, three-dimensional effects on the flame propagation are incorporated in S . The 1D burning velocity is used as an input parameter to the combustion model and the determination of this parameter is described in the next subsection. The solution for the state of the burnt mixture is found by the intersection of the Rayleigh line with the Hugoniot curve. The solution could be either a weak deflagration or a CJ deflagration (Williams, 1985).

In the combustion model, the combustion wave is treated as a discontinuity (i.e. thin flame model). When the 1D burning velocity is known, the flame propagation in the domain between two neighbouring grid points can be handled in essentially the same way as for the non-reactive Riemann problem. As illustrated in Figure 4.13, the left and right propagation waves (shock or rarefaction) are handled as in the Riemann problem. The only difference is that the state at the contact surface, u_* and p_* must be treated as u_{*u} and p_{*u} for unburnt gas and u_{*b} and p_{*b} for the burnt gas.

The value of p_{*u} is found by using the Newton-Rhapson iteration procedure and u_{*u} and ρ_{*u} are found from the equations given in subsection 4.2.1 and 4.2.2. The values for the burnt mixture p_{*b} , u_{*b} and ρ_{*b} are found from the Rankine-Hugoniot relations. The flame position at each time step is determined by the position of a jump in the value of the fraction γ .

4.2.4 Method for estimation of the quasi 1D burning velocity

Some testing of models for the burning velocity was performed initially. The burning velocity was also modelled with an initial increase as an error function up to a constant level. This modeling gave reasonable results, but it was decided to focus the work on a method for estimating a burning velocity from experimentally determined pressure records.

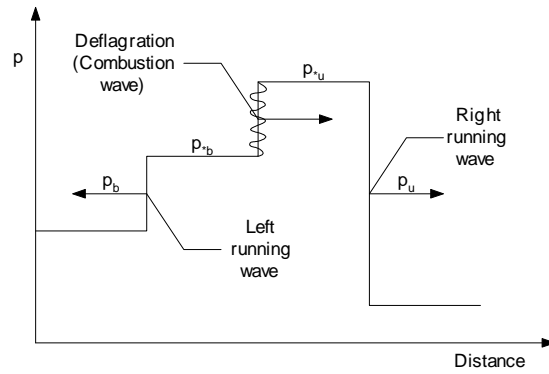


Figure 4.13: The combustion model used in RCMLAB.

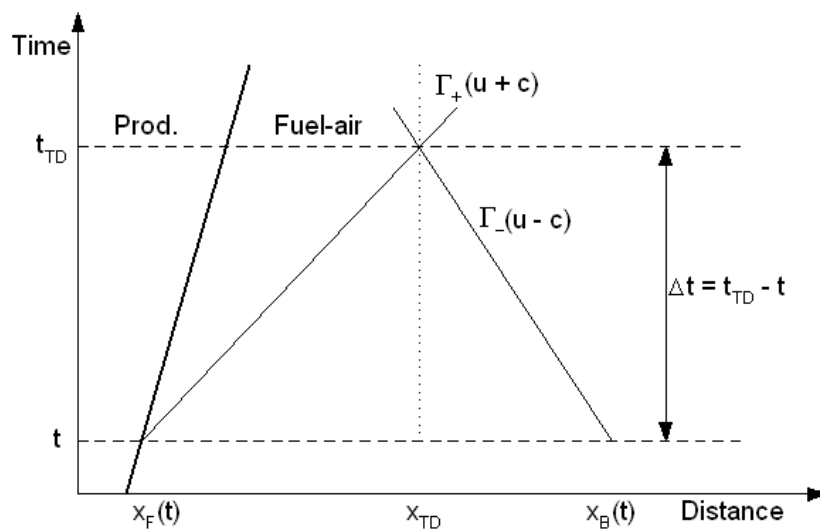


Figure 4.14: Location of $\Delta p (x_{TD}, t_{TD})$.

A version of the method is presented by Bjerketvedt et al. (2003 and 2004) and the validation of the method against experimental data is presented by Kristoffersen et al. (2003b and 2004).

In Figure 4.14, the principles for the method are illustrated. When the burning velocity of the flame front at x_F is changed at time t , pressure waves are generated that propagate away from the front in both directions. The forward propagating wave will reach the point of the next pressure transducer ahead of the flame at time t_{TD} . The time t_{TD} is governed by the speed $(u + c)$ of the right running characteristic Γ_+ . A point $x_B(t)$ at the right side of the transducer is determined by the left running characteristic Γ_- with propagation speed $(u - c)$. To find the most appropriate point for $x_B(t)$, a vector of positions is tested and the position that gives a characteristic that will be closest to x_{TD} at time t_{TD} is used. A pressure value $p_*(x_{TD}, t_{TD})$ is determined by solving a Riemann problem with the left state given by the state at $x_F(t)$ and the

right state given by the state at $x_B(t)$. This calculation is done in a single time step, Δt , in the standard RCMLAB Riemann solver as described in Subsection 4.2.2. The length of the time step is determined by the difference $\Delta t = t_{\text{TD}} - t$. The calculated pressure $p_*(x_{\text{TD}}, t_{\text{TD}})$ is compared to experimental pressure records for the transducer at position x_{TD} at time t_{TD} and an pressure error value is determined:

$$\Delta p_\varepsilon = p_{\text{TD}}(x_{\text{TD}}, t_{\text{TD}}) - p_{*\text{RCM}}(x_{\text{TD}}, t_{\text{TD}}). \quad (4.37)$$

During each time step in the main RCM routine, a vector of values for the 1D burning velocity is tested, which gives a vector of pressure error values. A value for the 1D burning velocity that gives $\Delta p_\varepsilon = 0$ is determined by cubic spline interpolation within the vectors of the 1D burning velocities and the pressure error values. This quasi 1D burning velocity is then used as an input to the combustion model.

The first transducer ahead of the flame is used as a reference transducer. However since transducer 4 (last one) is used to control the boundary conditions at the pipe outlet, the simulation will be unstable if the same transducer is also used to control the 1D burning velocity. Transducer 3 is therefore also used after the flame has passed this transducer. The conditions behind the flame are much more unstable than before the flame, and the 1D burning velocity would also be unstable if it is estimated from values of Δp_ε at a single time step. The estimation of the 1D burning velocity is therefore not performed independently of the values in the former time steps. Instead, a proportional controller is used to estimate a new 1D burning velocity from the 1D burning velocity in the previous time step and the pressure error value at the actual time step for the associated transducer position. The equation for determining $S(t)$ is shown in Equation 4.38. This can be regarded as a proportional controller with Δp_ε as the disturbance and K as the gain. To avoid instabilities when the flame is passing the transducer position 4, the 1D burning velocity is kept constant at the end of the pipe.

$$S(t) = S(t - \Delta t) + K(p_{\text{TD}}(x_{\text{TD}}, t_{\text{TD}}) - p_{*\text{RCM}}(x_{\text{TD}}, t_{\text{TD}})) = S(t - \Delta t) + K\Delta p_\varepsilon(x_{\text{TD}}, t_{\text{TD}}) \quad (4.38)$$

4.2.5 Determination of pipe outlet conditions

Determination of the pipe outlet is a crucial parameter because of the longitudinal acoustic waves that propagate in the pipe. These waves are reflected at the pipe ends. At the left pipe end is a wall, which is calculated by defining the velocity at the left

boundary of the first grid point to have the opposite direction of the velocity to the right of the boundary. The same definition could also be used at the right end of the pipe if a wall should be presented there. If the right end is open, the pressure waves should be able to propagate freely into the ambient air at atmospheric conditions.

Two methods are used to represent the pipe outlet. In the first one, the pressure waves are allowed to propagate spherically outwards from the pipe opening. A parameter defining the area increase during the expansion at the outlet is used:

$$AC(i) = \frac{k_{\text{angle}}}{D/2 + L(i - nt + 1)/nt} \quad (4.39)$$

where k_{angle} is a constant defining the angle of the expansion at the outlet with $k_{\text{angle}} = 1$ when the expansion angle is 180° , D is the pipe diameter, L is the pipe length, i is the grid cell used and nt is the number of grid cells in the pipe. The density and pressure in the grid cells are then reduced because of the expansion and new values for these parameters are calculated by using the area increase parameter:

$$\rho = \rho(1 - ACu\Delta t), \quad (4.40)$$

$$p = p(1 - AC\gamma u\Delta t). \quad (4.41)$$

In the second method, the conditions at the outlet are estimated from experimental data by using the Riemann solver in an equivalent manner to the estimation of the quasi 1D burning velocity as described in Figure 4.14. The pressure records at the fourth transducer are used as reference. The pressure at this position is calculated by using the conditions at the outlet as the right state. The position of the left state is determined in such a way that the right running characteristic reaches the transducer at the same time as the left running characteristic. The calculated pressure is compared to the experimental pressure and a pressure error value is calculated by Equation 4.37. At each time step, a vector of various pressures at the outlet is used to calculate a vector of pressure error values. The value for the outlet pressure that gives $\Delta p_\varepsilon = 0$ is determined by cubic spline interpolation within the vectors of the outlet pressures and the pressure error values.

4.2.6 Modeling of heat loss and friction

For flame propagation in pipes, there will always be a momentum loss due to friction along the pipe walls and a heat loss to the surroundings by heat transport through the pipe walls. In the 1D RCMLAB code, these inhomogeneous effects are taken

into account by a operator-splitting method (Sod, 1977). Modeling of heat loss and friction is described by Bjerketvedt (1985). Three regimes are identified according to the value of the Reynolds number, which are given different values of a factor C_f as defined in Equation 4.42. For the laminar regime, C_f is defined to zero, and for the two other regimes models are given by Kays and Crawford (1993). For the fully developed turbulent regime, an empirical equation that equals the Kármán-Nikuradse equation for a circular pipe is used.

$$C_f = \left\{ \begin{array}{ll} 0, & \text{for } \text{Re} < 10000, \text{ laminar regime} \\ 0.078 \text{Re}^{-0.25}, & \text{for } 10000 < \text{Re} < 30000, \text{ transition regime} \\ 0.046 \text{Re}^{-0.2}, & \text{for } \text{Re} > 30000, \text{ turbulent regime} \end{array} \right\} \quad (4.42)$$

This factor is also influenced by the wall specifications, such as roughness and conductivity of the wall. The C_f value for the fully developed velocity profile is therefore enhanced by multiplication with a wall specific factor, ξ . For the simulations of the experiments with plexiglass pipes (campaign 4 and 5 in Table 4.3), a factor $\xi = 2.2$ was found to give good results in all simulations. For the simulations of the experiments in the steel pipes, the same factor was not used in all campaigns. In simulation campaign 1 in Table 4.3, where the simulation results are only compared to experimental pressure records, good results were obtained with a factor $\xi = 2.5$. When the simulation results were also compared to records of the flame propagation from experiments, as in simulation campaign 2, a larger factor of $\xi = 8.0$ had to be used to obtain good results. It seems like the flame propagation is more sensitive to ξ than the pressure waves. In simulation campaign 3, good results were obtained with $\xi = 1.0$. For this fast flame propagation, the value of ξ seems to have less consequences on the flame propagation than in the slow flame propagation with propane. Further investigation of the factor ξ has to be accomplished to determine its dependence on pipe specifications, mixture reactivity etc.

The wall friction, τ_w , can be given as (Kays and Crawford, 1993):

$$\tau_w = \xi C_f \frac{\rho u^2}{2}, \quad (4.43)$$

where ρ is the density and u the velocity. The heat flux at the wall surface, \dot{Q} , can be defined by (Eckert and Drake, 1987):

$$\dot{Q} = h (T_r - T_w), \quad (4.44)$$

where h is the heat transfer coefficient, T_w is the wall temperature and the recovery

temperature T_r is given by $T_r = T + r \frac{u^2}{2C_p}$. The recovery factor, r , in a turbulent layer, is defined by the Prandtl number $r = \sqrt[3]{\text{Pr}}$ (Eckert and Drake, 1987). For the gases used, Pr is approximately 0.7. The heat transfer coefficient is related to the friction factor by the Reynolds analogy (Schlichting and Gersten, 2000):

$$h = \frac{\xi C_f}{2} \rho C_p u, \quad (4.45)$$

where C_p is the heat capacity at constant pressure. When assuming ideal conditions and that the wall temperature is equal to the ambient temperature, the heat flux at the wall surface can be written:

$$\dot{Q} = \frac{1}{2} \xi C_f \left[0.45 \rho u^3 + \frac{\gamma}{\gamma - 1} u \left(p - \rho \frac{p_0}{\rho_0} \right) \right], \quad (4.46)$$

where p_0 and ρ_0 are ambient conditions.

From the energy conservation equations, the new energy content after the heat loss has been taken into account is:

$$E = \frac{p}{\gamma - 1} + \frac{1}{2} u^2 - \frac{4}{D} \dot{Q} \Delta t, \quad (4.47)$$

The velocity is reduced due to friction according to:

$$u = u - \frac{4\tau_w \Delta t}{\rho D} = u - \frac{2\xi C_f}{D} u^2 \Delta t, \quad (4.48)$$

and a new value for the pressure is obtained from the energy equation.

4.2.7 Simulation of experiments

The experimental results are used to estimate the quasi 1D burning velocity and outlet conditions in the RCMLAB simulations. Simulations are performed both for the experiments in the steel pipes and in the plexiglass pipe, and for propane-air mixtures and acetylene-air mixtures in the different pipe lengths used. Five campaigns of simulations are performed to test the reliability of the RCMLAB code. A summary of the campaigns is given in Table 4.3, where references to the experimental campaigns are also given. The purpose of the first campaign was to test the simulated pressures against the experimental pressure records used in the estimation methods for different pipe lengths. In campaign 2, the simulated flame propagation was compared to photodiode records. In campaign 3, the code was tested for higher flame speeds, which were achieved by using acetylene-air mixtures. In campaigns 4 and 5, the flame propagation was tested against pictures of the flame propagation obtained by an SLR camera and

Table 4.3: Simulations performed in RCMLAB. References to the experimental campaigns are indicated.

Campaign	Description	Ref. exp.
1	Propane-air mixtures in various pipe lengths	1
2	Validation by photodiode records	2
3	Testing for fast flame propagation	3
4	Validation by SLR camera pictures	6
5	Validation by high-speed camera records	7

a high-speed camera.

Propane-air mixtures in 1, 2 and 5 m steel pipes

Simulations are performed of the experiments with propane-air mixtures in the 1, 2 and 5 m steel pipes. The simulations were performed to test the code by using experimental pressure records. The simulated pressure histories are compared to the experimental data.

1 m pipe Simulations with propane-air mixtures at equivalence ratios 1.0 and 1.2 in the 1 m pipe are shown together with experimental data in Figures 4.15 and 4.16 respectively. There is good agreement between the simulated pressure values and the experimental pressure records. The simulated position of the flame fronts is shown by the dashed line. The simulated initial flame propagation is somewhat larger for the stoichiometric mixture, but the mixture with $\phi = 1.2$ gives a stronger acceleration towards the pipe outlet and will have a larger average flame speed. For the stoichiometric mixture, the flame front reaches the pipe outlet after 31 ms and the average flame speed is 32.3 m/s. When $\phi = 1.2$, the flame front reaches the outlet after 29 ms, which gives an average flame speed of 34.5 m/s. For both mixtures, the flame propagation is reversed as the flame front is interacting with the acoustic oscillations. In Figure 4.17, the estimated quasi 1D burning velocity for the two equivalence ratios is shown. The value of the first maximum burning velocity is 5.3 m/s and 6.2 m/s for $\phi = 1.0$ and 1.2 respectively. During the interactions with the acoustic oscillations, the 1D burning velocity goes to zero.

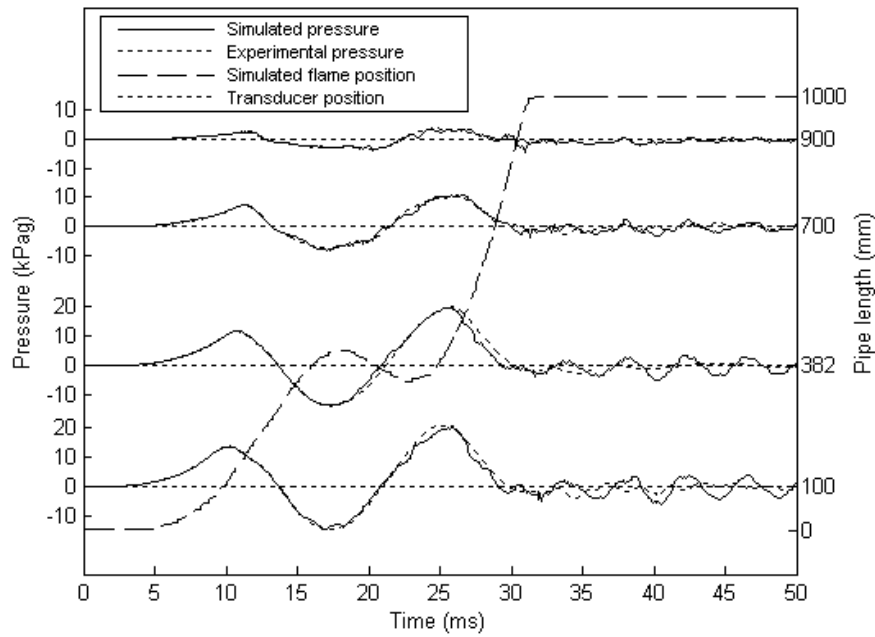


Figure 4.15: Simulation in RCMLAB of a propane-air mixture at $\phi = 1.0$ in the 1 m steel pipe.

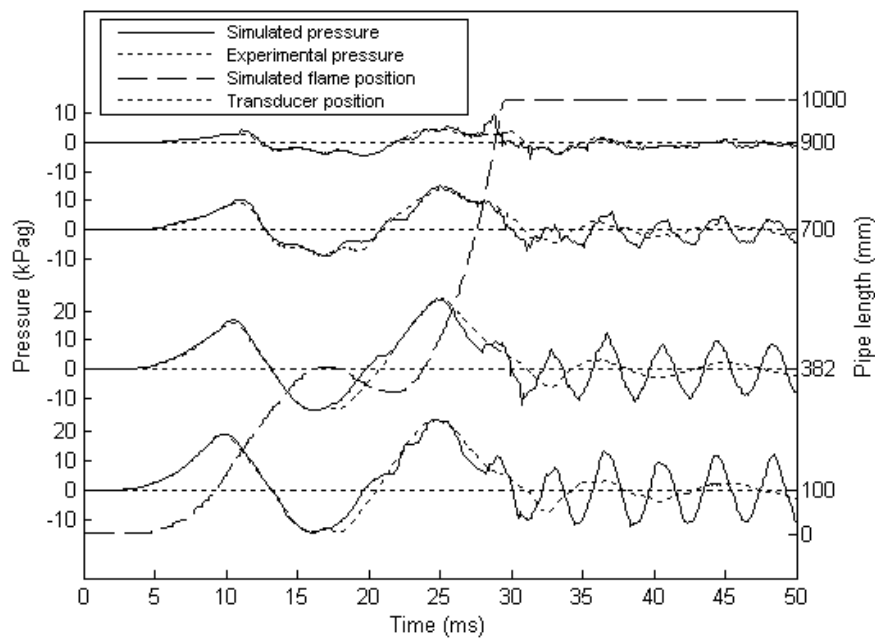


Figure 4.16: Simulation in RCMLAB of a propane-air mixture at $\phi = 1.2$ in the 1 m steel pipe.

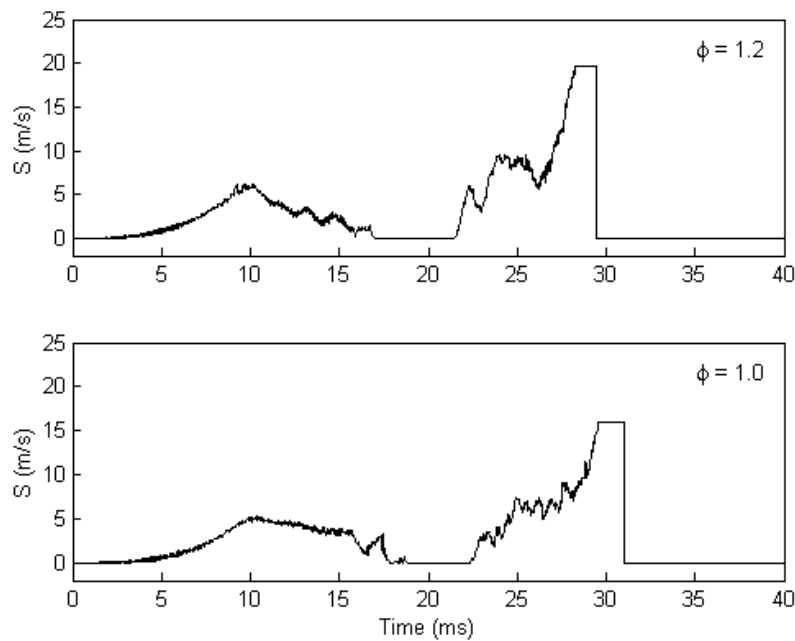


Figure 4.17: Estimated quasi 1D burning velocity for $\phi = 1.0$ and 1.2 for propane-air mixtures in the 1 m steel pipe.

2 m pipe One example of the simulations in the 2 m pipe is shown for a stoichiometric propane-air mixture in Figure 4.18. There is also good agreement between the simulated and the experimental pressure histories for this pipe length. At transducer position 3, the simulated pressure history is independent of the experimental pressure record during the first 64 ms. In this period, the experimental records from transducer 3 is not used. The estimated pressure history at transducer 3 is therefore giving a useful indication of the reliability of the code. In Figure 4.19, the simulated and experimental pressure histories at transducer 3 for the first 80 ms is shown. The simulated values are shifted 5 kPa to better distinguish the two histories. From the figure it can then be concluded that the simulation results are satisfactory. In Figure 4.18, the simulated flame position is plotted as a dashed line. The flame reaches the pipe outlet after 97 ms, which gives an average flame speed in the pipe of 20.6 m/s.

5 m pipe For the 5 m pipe shown in Figure 4.20, the simulation results become more noisy after a time. In this pipe, deviations have a longer time to influence the simulation and therefore the results could become more noisy. Some inaccuracies are also introduced by the longer distances between the flame position and the transducers. The simulations are, however, giving a good indication of the pressure history. The flame front reaches the pipe outlet at 253 ms, which gives an average flame speed of

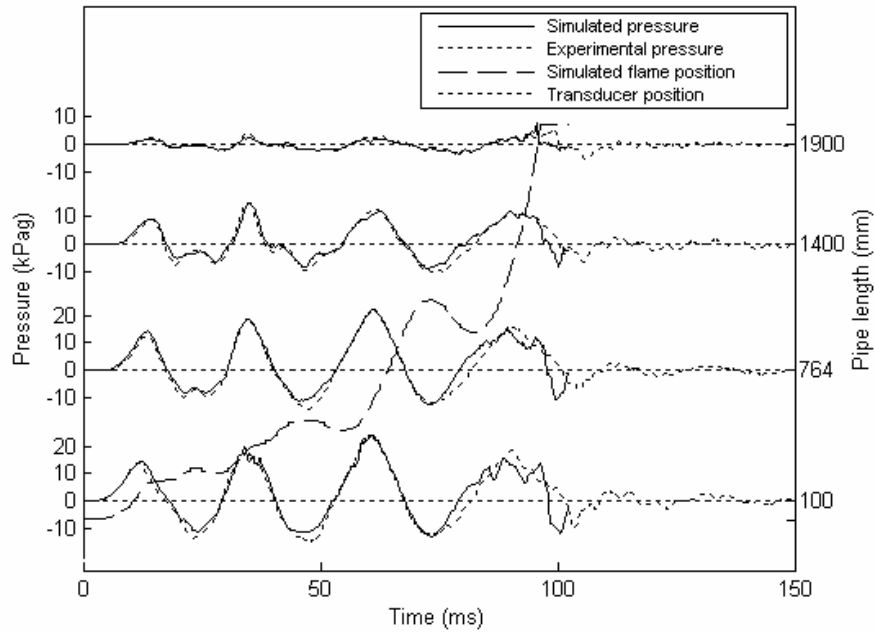


Figure 4.18: Simulation in RCMLAB of a propane-air mixture at $\phi = 1.0$ in the 2 m steel pipe.

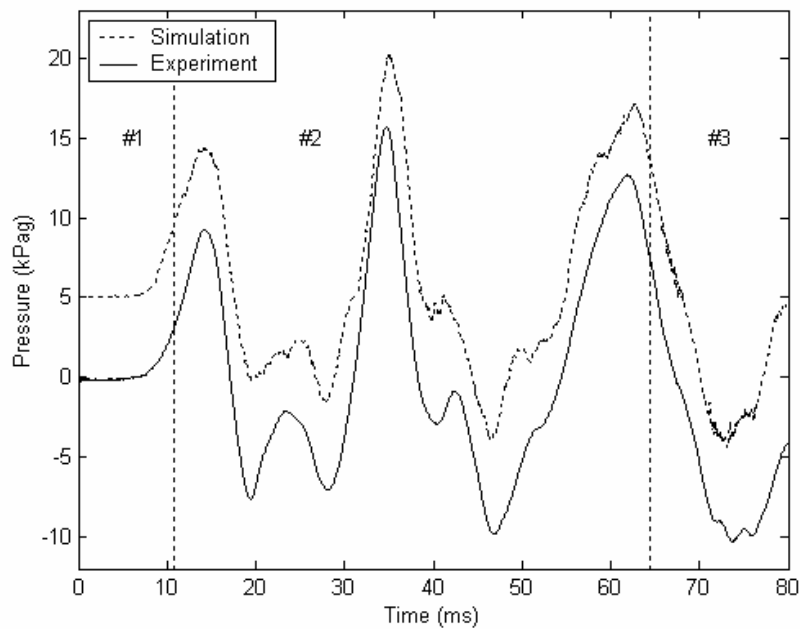


Figure 4.19: Pressure histories at transducer position 3 from experiment and simulation in RCMLAB with a stoichiometric propane-air mixture in the 2 m steel pipe. The simulation has an offset of 5 kPa. The transducers used for estimation of the quasi 1D burning velocity are indicated.

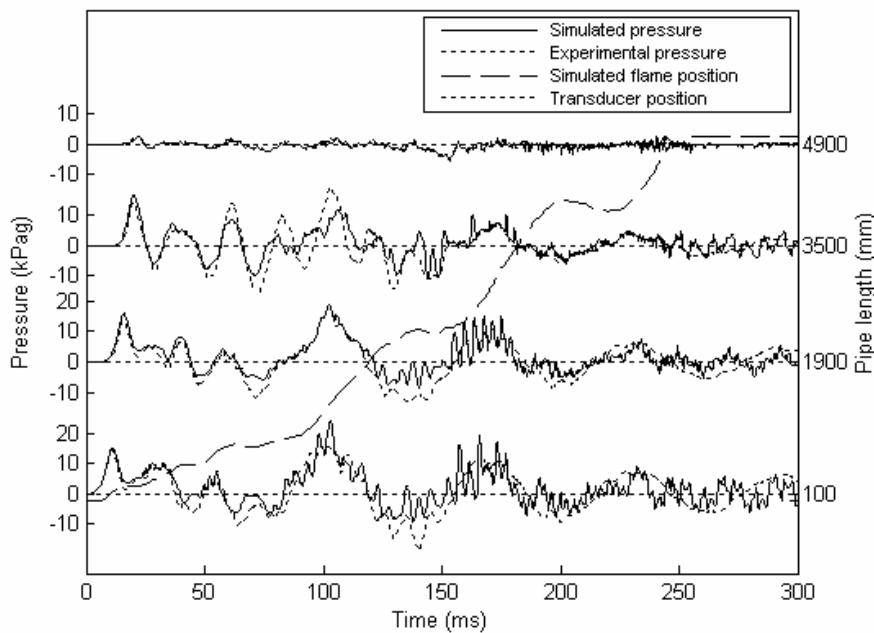


Figure 4.20: Simulation in RCMLAB of a propane-air mixture at $\phi = 1.0$ in the 5 m steel pipe.

19.8 m/s.

Concluding remarks The estimated quasi 1D burning velocities for the three pipe lengths are shown in Figure 4.21 for stoichiometric mixtures. The 1D burning velocities go to zero in some intervals, which appear during the inversions. The 1D burning velocity histories in the initial state are quite similar for all three pipe lengths. In the case of the 1 m pipe it appears that when the rarefaction wave reaches the flame, the 1D burning velocity remains at a higher value for an extended time period than for the two other pipe lengths. This behavior is influenced by the density fall across the rarefaction wave in combination with the increased heat release. For the 2 and 5 m pipes, the 1D burning velocity is decreasing in nearly the same manner. In the 2 m pipe, the flame front begins to interact with the pressure waves from after around 24 ms, where the 1D burning velocity goes to zero during an inversion of the flame front. Similar behaviour is seen for the 1 m pipe from around 18 ms. In the 5 m pipe, the 1D burning velocity goes almost to zero at 16 ms. This short minimum 1D burning velocity probably occurs during the flame inversion due to quenching of the flame front at the pipe wall.

In Figure 4.22, estimated 1D burning velocities of stoichiometric mixtures in the three pipe lengths are compared. For both the 2 m and 5 m pipe, the first peak is

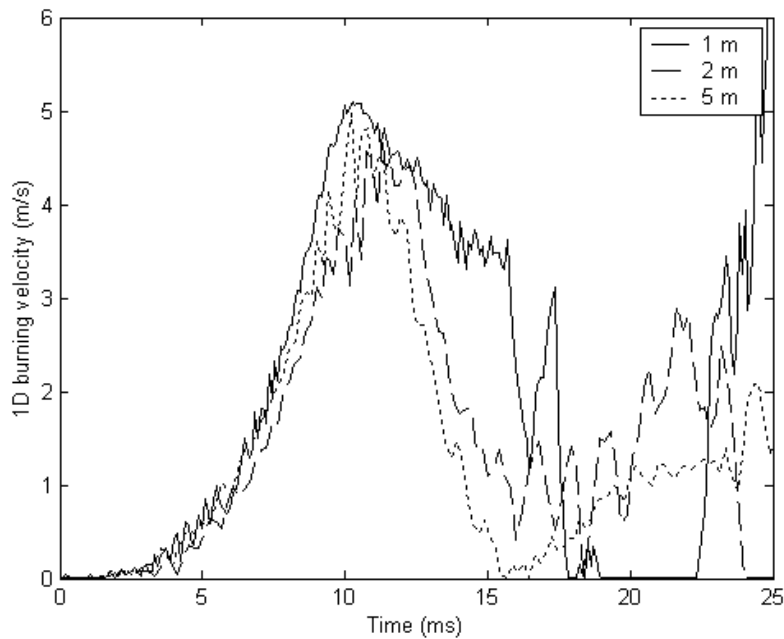


Figure 4.21: The estimated quasi 1D burning velocity for three pipe lengths. Propane-air mixtures at $\phi = 1.0$.

similar because the reduction is caused by quenching at the pipe wall. In the 1 m pipe, the 1D burning velocity has a small and steady reduction during the interaction with the rarefaction wave before the flame inversion occurs and the 1D burning velocity goes to zero. After the inversion, the flame propagation is accelerated strongly up to an approximately constant level, before a new acceleration occur towards the pipe outlet. A similar behaviour is seen for the 2 m pipe, where the 1D burning velocity is reduced gradually before the inversions and with a strong acceleration after the inversions. These latter phenomena are not seen clearly for the 5 m pipe, because there are more oscillations in the 1D burning velocity. For all pipes, there is an acceleration towards the pipe outlet.

The average flame speeds for the stoichiometric propane-air mixtures in the 1, 2 and 5 m pipes are 31.5 m/s, 20.7 m/s and 19.7 m/s respectively. For the two longest pipes the average flame speed is around 20 m/s, while in the 1 m pipe it is considerably higher. Also in agreement with Kerampran et al. (2001), it seems that the average flame speed is independent of the pipe length. This independence is probably caused by the oscillations in the flame propagation, and will therefore only occur for slow flames where these oscillations are substantial. The larger average flame speed in the 1 m pipe may occur because of the large acceleration towards the pipe outlet after only one oscillation of the flame propagation. When more oscillations occur, a potential

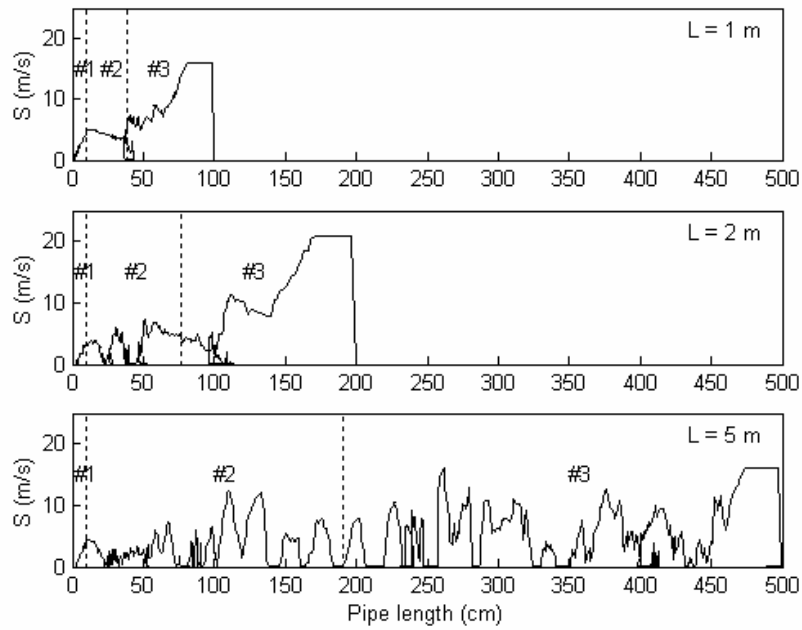


Figure 4.22: Estimated quasi 1D burning velocity for stoichiometric propane-air mixtures in steel pipes of different lengths. The transducers used for estimation of the quasi 1D burning velocity are indicated.

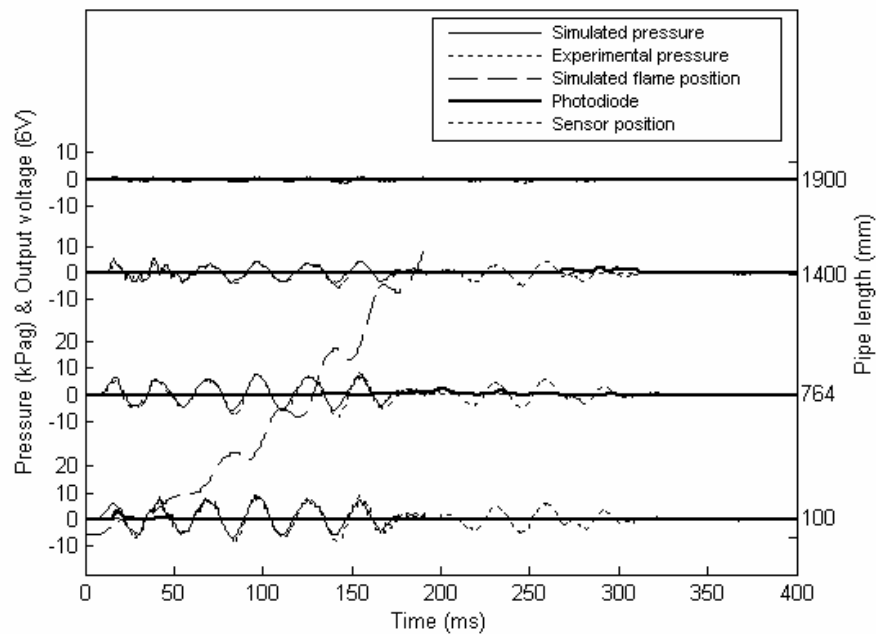


Figure 4.23: Simulation in RCMLAB of a propane-air mixture at $\phi = 0.9$ in the 2 m steel pipe.

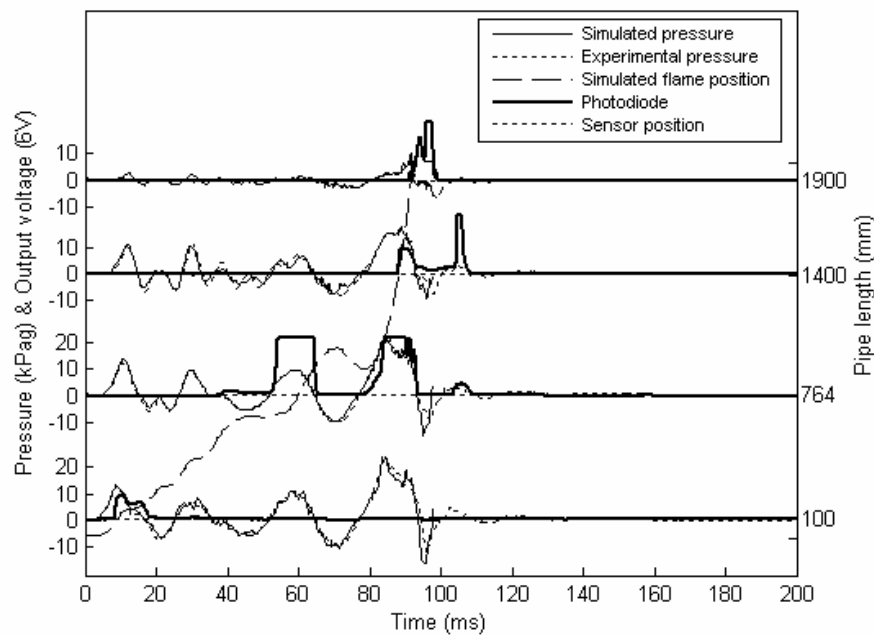


Figure 4.24: Simulation in RCMLAB of a propane-air mixture at $\phi = 1.2$ in the 2 m steel pipe.

acceleration of the flame propagation towards the pipe outlet will be of less importance.

Propane-air mixtures in the 2 m steel pipe with photodiodes

Simulations with propane-air mixtures in the 2 m pipe for equivalence ratios 0.9, 1.2 and 1.5 are shown in Figures 4.23 - 4.25. There is good agreement between experimental and calculated pressure records and flame positions. For $\phi = 0.9$, the flame is quenched just after it has passed the third transducer. In the experiments, it seems like the combustion process is reinitiated, but this would not occur in the simulations. For $\phi = 1.2$, the flame is traveling back into the pipe after it has reached the outlet in the experiment, but in the simulations the flame could not travel backwards after it has reached the outlet. A similar behaviour is observed for $\phi = 1.5$. Then the flame in the experiment is oscillating around the third transducer before it is accelerated towards the opening. In the simulation, the flame propagates to the fourth transducer and is quenched there. The simulation of the two rich mixtures indicate that it could be difficult to simulate oscillations in combustion and acoustic waves near the pipe outlet. The problem could also be a result of air entering into the pipe such that the reactivity of the mixture is changed. This effect is not simulated.

In Figure 4.26, the density in the pipe ahead of the flame front is shown for the mixture at $\phi = 1.2$. The first flame inversion occurs independently of the pressure

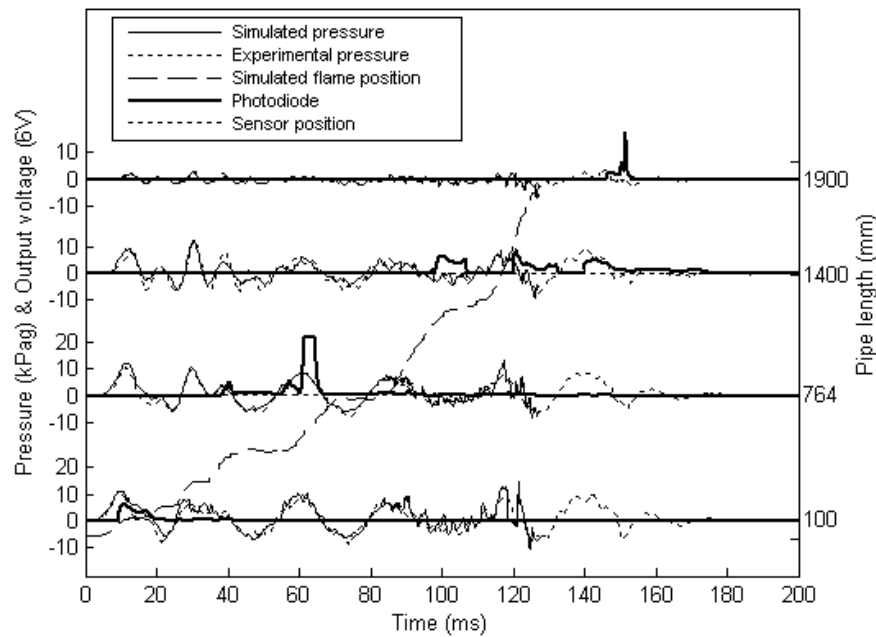


Figure 4.25: Simulation in RCMLAB of a propane-air mixture at $\phi = 1.5$ in the 2 m steel pipe.

waves in the pipe. For the next inversions there will be some interactions with the pressure waves, but the flame front propagation will begin to oscillate with the acoustic oscillations in the pipe only for the two last inversions.

The flame positions from simulations with four equivalence ratios are shown in Figure 4.27. The lean mixture is clearly less reactive than the other mixtures and there are several oscillations in the flame propagation. For $\phi = 1.0$ and 1.2, the flame is propagating very similar up to around 63 ms. The stoichiometric mixture achieves a somewhat higher flame speed than the mixture at $\phi = 1.2$, and experiences therefore the reversal of the flame propagation because of the interactions with the acoustic oscillations after a longer distance in the pipe. After the reversal, the flame propagation is reaccelerated. For $\phi = 1.2$, the reversal occurs earlier and there is therefore more time for acceleration after the reversal, such that the flame reaches the pipe outlet earlier for this mixture than for the stoichiometric mixture. The flame speed for $\phi = 1.5$ is smaller than the two former mixtures and the flame is quenched before it reaches position 4.

The estimated 1D burning velocities for three equivalence ratios, 0.9, 1.0 and 1.2, in the 2 m pipe are shown in Figure 4.28. Only a small difference is observed between equivalence ratios 1.0 and 1.2. For the ratio 0.9, the 1D burning velocity is considerably less and the time to reach the first maximum is greater.

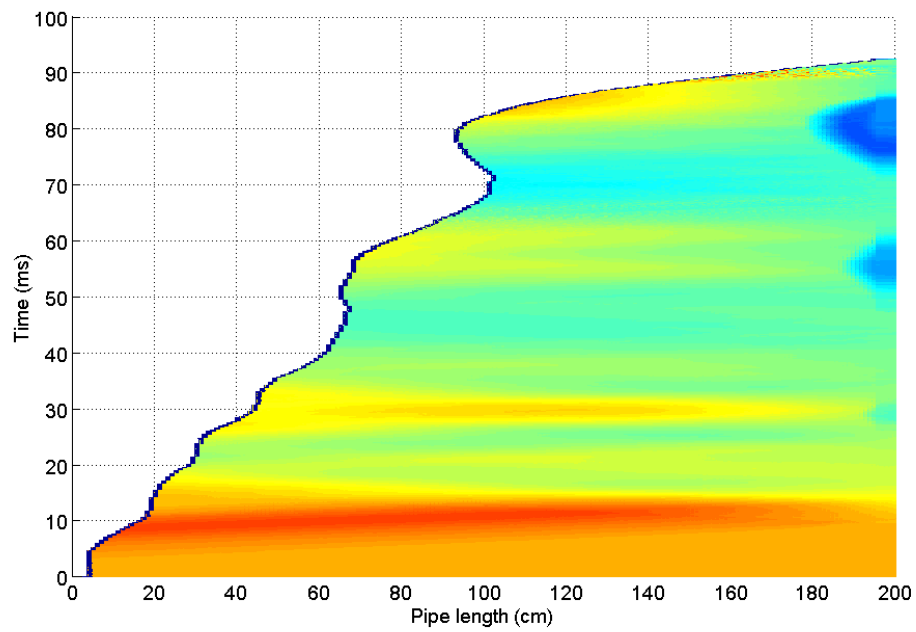


Figure 4.26: The density development ahead of the flame front for a simulation in RCMLAB of a propane-air mixture at $\phi = 1.2$.

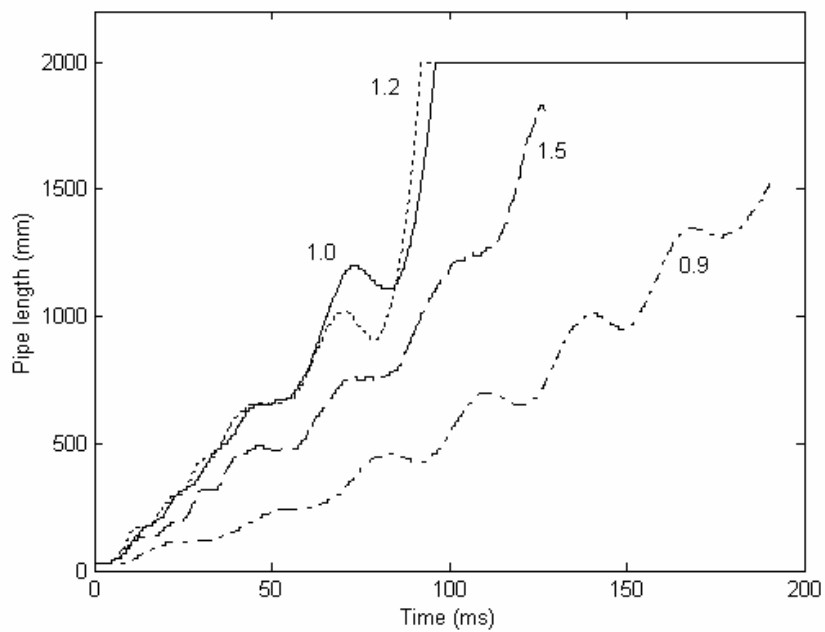


Figure 4.27: The simulated flame positions for four trials with propane-air mixtures at $\phi = 0.9, 1.0, 1.2, 1.5$.

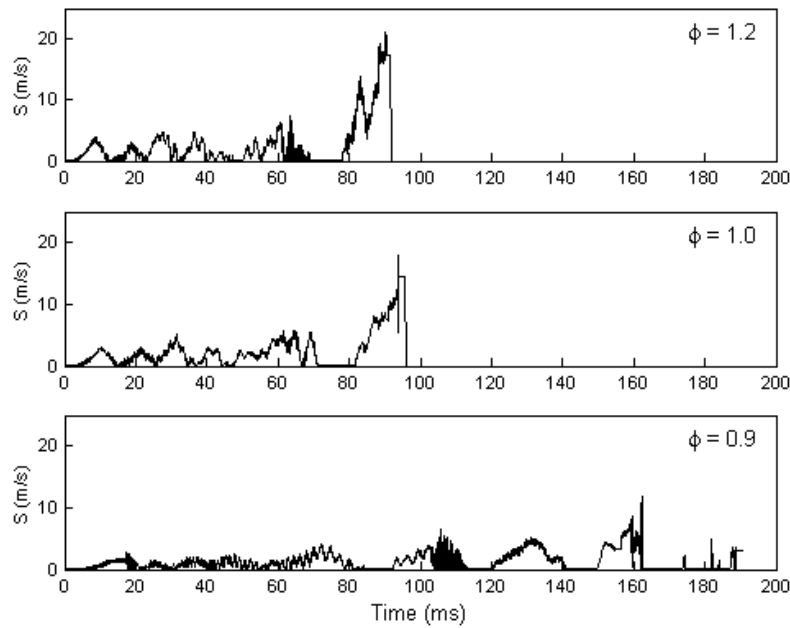


Figure 4.28: The estimated quasi 1D burning velocity, S , for propane-air mixtures at three equivalence ratios in the 2 m pipe.

Acetylene-air mixtures in the 2 m steel pipe

Simulations have been performed of the experiments with acetylene-air mixtures in the 2 m steel pipe. Because of the higher flame speed in these mixtures than in the propane-air mixtures, the RCMLAB code will be tested for fast flame propagation in this simulation campaign. The results with acetylene for a 2 m pipe in Figure 4.29 indicate a much stronger FA which gives much higher pressures. The simulated pressure histories follow the experiments with some small deviations. These deviations may also be a result of a too short recording frequency in the experiments. In the experiments, there is a second explosion near the outlet which is first recognized at transducer 4. It is difficult to get the same pressure rise at transducer 4 in the simulation, but the explosion is intercepted at the third transducer and gives a large increase in the 1D burning velocity. There is adequate agreement between the simulated flame position and the captured radiation from the flame front by the photodiodes on the optical sensors.

In Figure 4.30, the estimated 1D burning velocity is given. The estimated 1D burning velocity is larger than for propane and has a maximum value of 35.7 m/s.

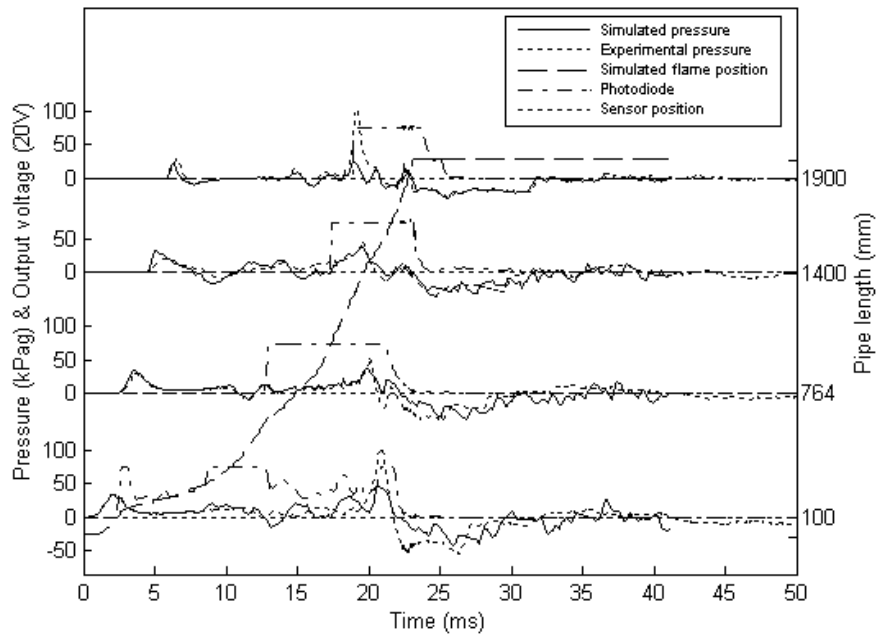


Figure 4.29: Simulation in RCMLAB of a acetylene-air mixture at $\phi = 1.0$ in the 2 m steel pipe.

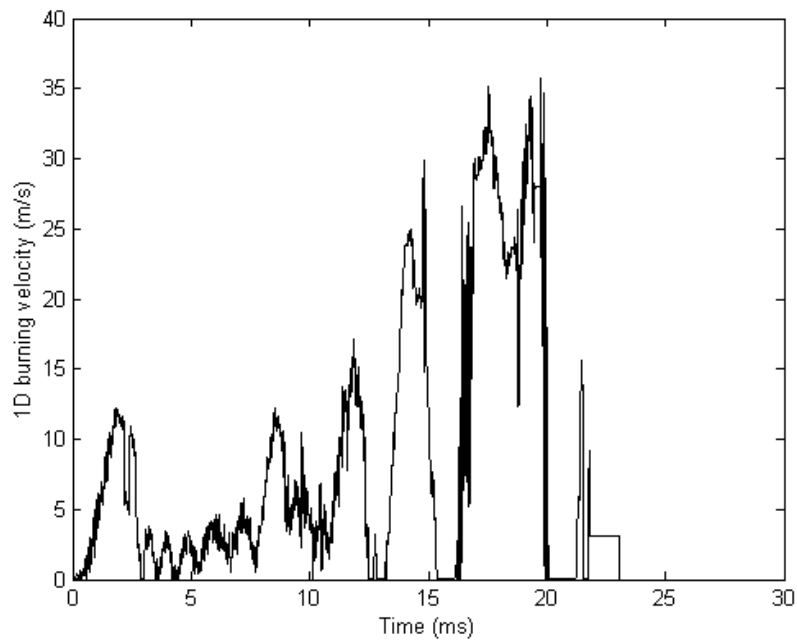


Figure 4.30: Estimated quasi 1D burning velocity for a stoichiometric acetylene-air mixture in the 2 m steel pipe.

Propane-air mixtures in plexiglass pipe. SLR camera

Simulations have been performed of the experiments with propane-air mixtures in the 1.9 m plexiglass pipe, where a SLR camera was used to capture the flame propagation.

In Figures 4.31, 4.32 and 4.33, the intensity of the blue colour in the pictures from the experiments is compared to the integrated local burning rate from simulations. The magnitude of the simulated values is adjusted to the same level as the blue colour fraction. The pictures do not cover the whole pipe length, but there is good agreement between the oscillations in the intensity of light emission and in the integrated local burning rate within the covered length.

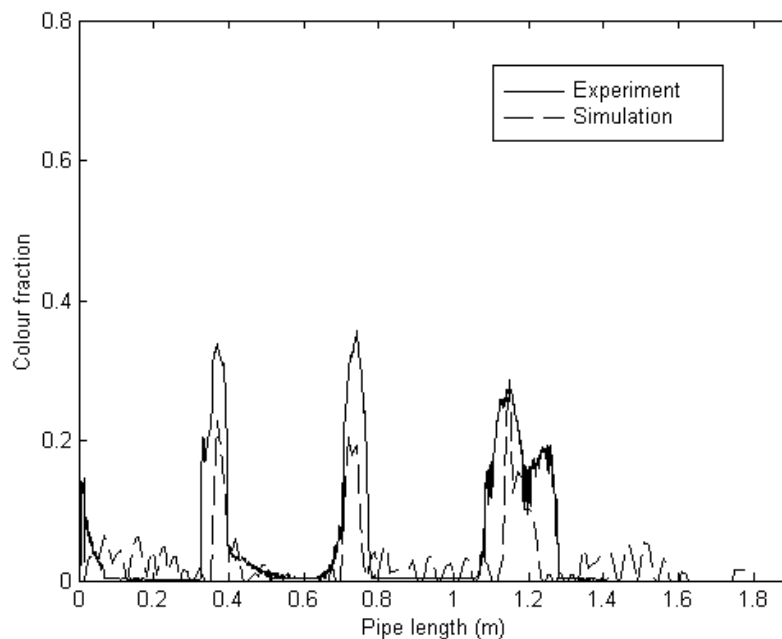


Figure 4.31: Light emission from experiment and integrated local burning rate from simulation. Propane-air mixture at $\phi = 0.8$ in the plexiglass pipe.

Propane-air mixtures in plexiglass pipe. High-speed camera

Simulations are also performed for the experiments in the plexiglass pipe where a high-speed camera was used to capture the flame propagation. Experiments are simulated for $\phi = 0.8, 1.0$ and 1.2 . As shown in Figure 4.34 for $\phi = 1.0$, there is good agreement between the simulated and the experimental pressure data. From the figure it is also clearly seen that the flame oscillations are interacting with the acoustic oscillations from the first flame oscillation, which is in agreement with the experiments of Kerampran et al. (2001).

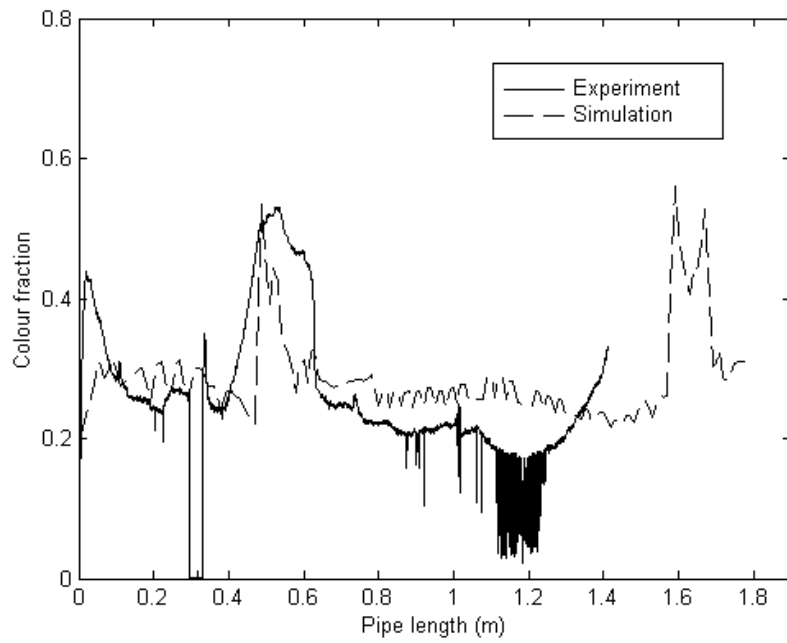


Figure 4.32: Light emission from experiment and integrated local burning rate from simulation. Propane-air mixture at $\phi = 1.0$ in the plexiglass pipe.

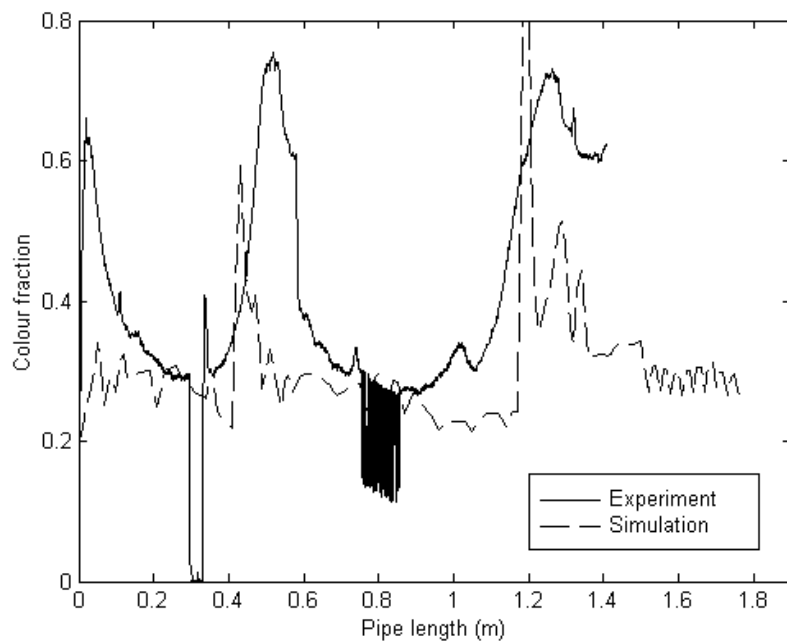


Figure 4.33: Light emission from experiment and integrated local burning rate from simulation. Propane-air mixture at $\phi = 1.2$ in the plexiglass pipe.

The flame position could be compared to the pictures given in Chapter 3, which is done for $\phi = 1.0$ and 1.2 in Figures 4.35 and 4.36. The simulated flame propagation is displayed as a white line on the pictures from the high-speed camera. The time axes are determined by the simulations. For both equivalence ratios, the simulated flame positions are satisfactorily in agreement with the experiments. In the simulations, the flame front is assumed to be a discontinuity, and it is the position of this discontinuity that is displayed. As seen on the pictures, the flame front in the experiments could have a much larger extension. The 1D model is nevertheless giving a flame front propagation from the experimental pressure records that is in agreement with the propagation of the flame front in the experiments. The oscillations of the flame front are also calculated properly.

In Figure 4.37, the density in the pipe ahead of the flame front is shown for the mixture at $\phi = 1.0$. The first flame inversion is initiated by the quenching of the flame front at the pipe wall. However, during this inversion the flame front will begin to interact with the pressure waves. The oscillations in the flame propagation therefore seem to be caused by the acoustic oscillations in the pipe.

Figure 4.38 shows the estimated quasi 1D burning velocities versus time for the three equivalence ratios. The largest 1D burning velocity is observed for $\phi = 1.2$. During the inversions, the flames are quenched or nearly quenched, which may be explained as local extinction due to an unsteady positive stretch of the flame and is related to flame extinction by a vortex as reported by Mueller et al. (1996). The value of the first maximum of the 1D burning velocity is 2.6 m/s, 3.6 m/s and 4.5 m/s for $\phi = 0.8$, 1.0 and 1.2 respectively. For the gas mixtures at $\phi = 1.0$ and 1.2, the flame propagation is strongly accelerated towards the pipe outlet. In Figure 4.39, the same 1D burning velocities are shown versus pipe length. All of the three 1D burning velocities are increasing the first 0.25 m, for then to decrease to zero or close to zero at around 0.45 m. During some of the inversions, the flame propagation is reversed a distance before it is reaccelerated again in the forward direction. For the stoichiometric gas mixture, two distinct inversions are observed. For $\phi = 1.2$, there is only one distinct inversion and for $\phi = 0.8$ the history is too unstable to recognize more than one distinct inversion.

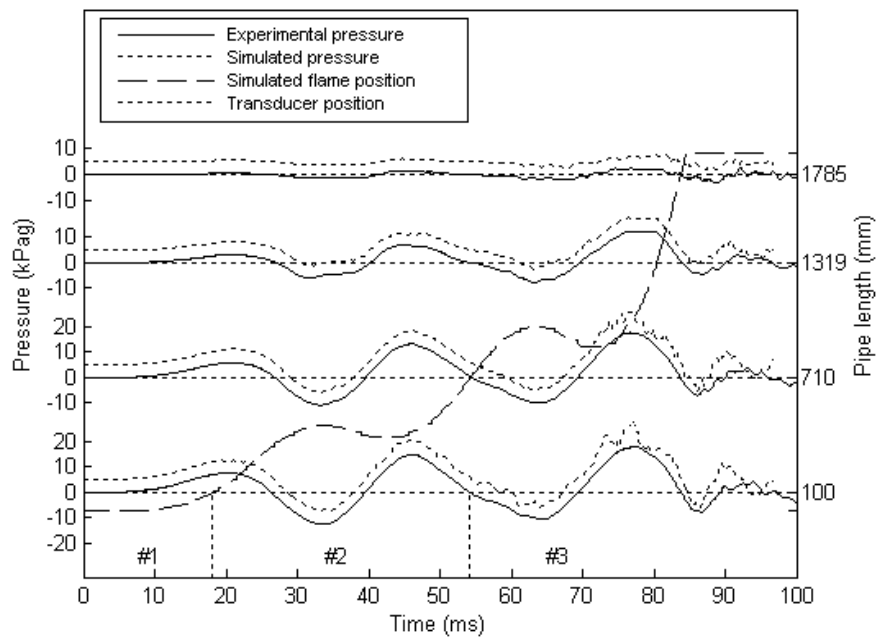


Figure 4.34: Simulation of an experiment with a stoichiometric propane-air mixture. The simulated pressure histories are shifted 5 kPa above the experimental histories. The transducers used for estimation of the quasi 1D burning velocity are indicated.

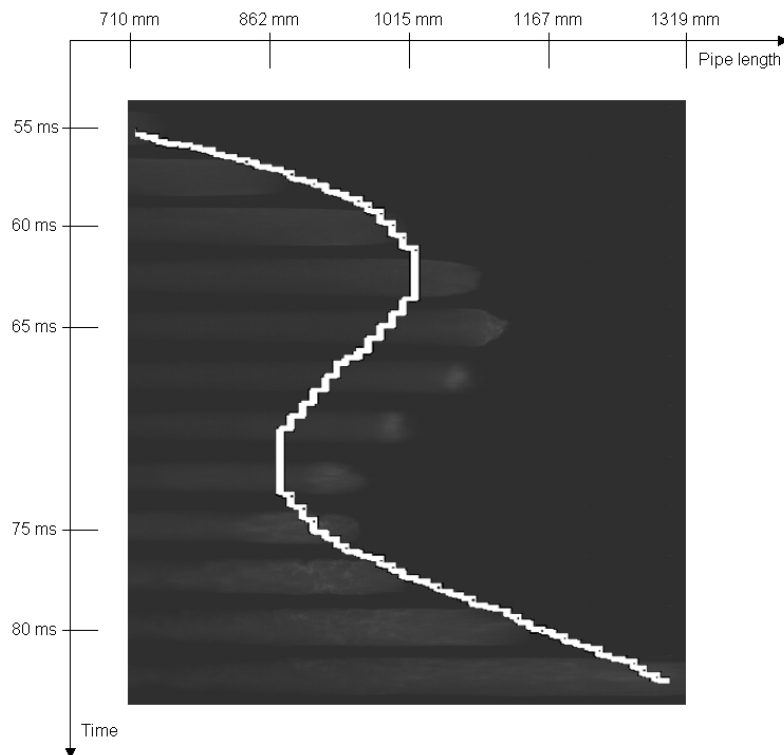


Figure 4.35: Pictures from the high speed camera compared to simulated flame position. Propane-air mixture at $\phi = 1.0$.

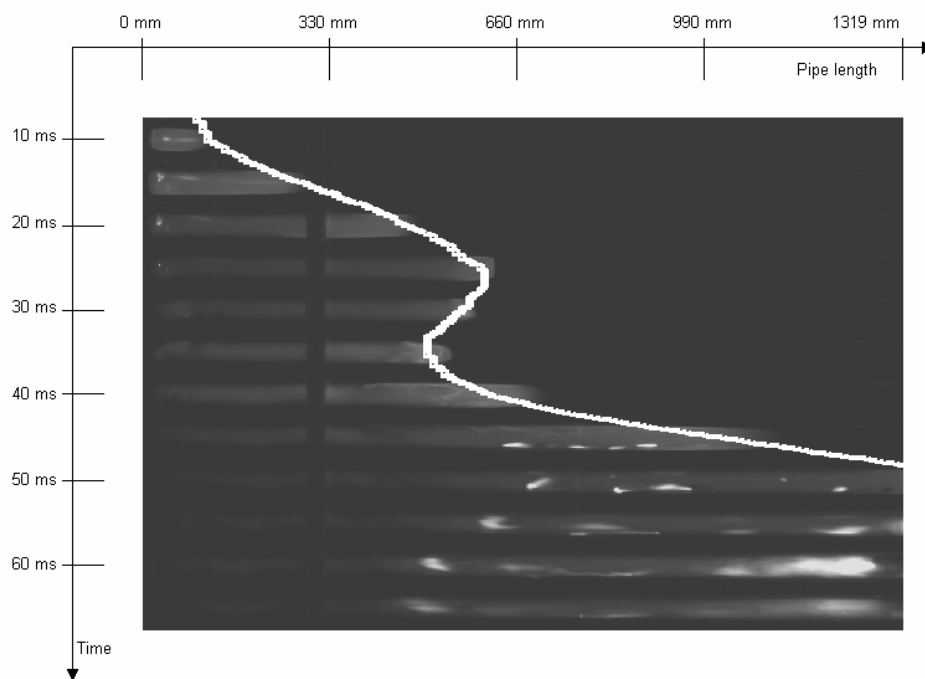


Figure 4.36: Pictures from the high speed camera compared to simulated flame position. Propane-air mixture at $\phi = 1.2$.

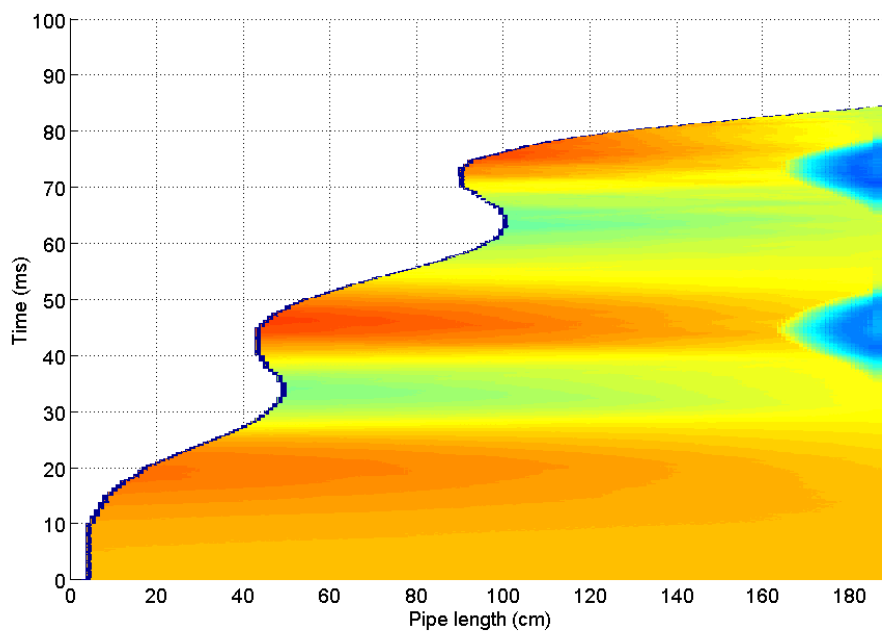


Figure 4.37: The density development ahead of the flame front for a simulation in RCMLAB of a propane-air mixture at $\phi = 1.0$ in the plexiglass pipe.

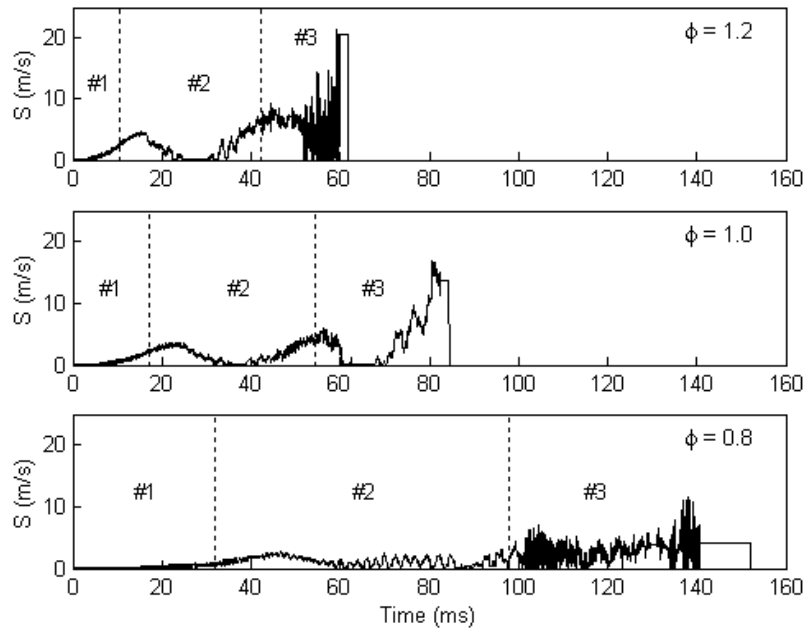


Figure 4.38: Quasi 1D burning velocities for simulations at three equivalence ratios with propane-air mixtures in the plexiglass pipe. The transducers used for estimation of the quasi 1D burning velocity are indicated.

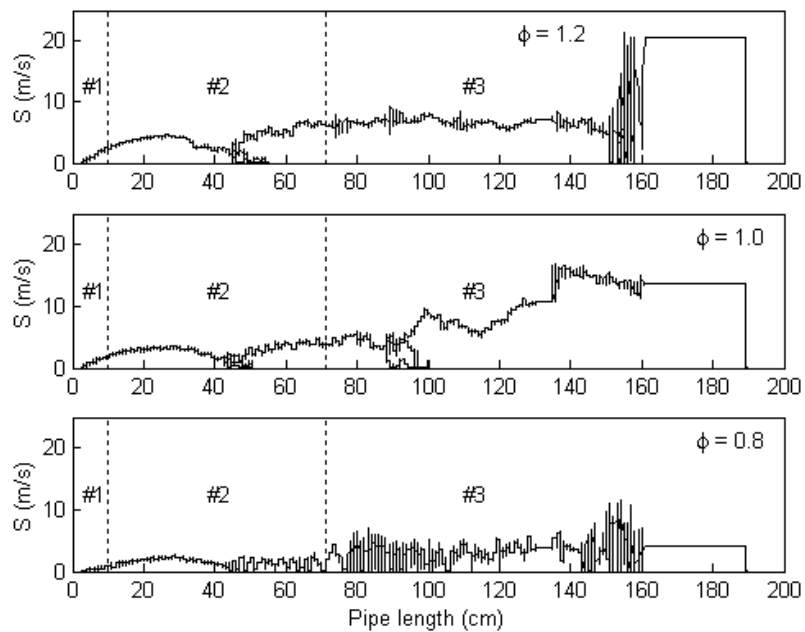


Figure 4.39: Quasi 1D burning velocities for simulations at three equivalence ratios with propane-air mixtures in the 1.9 m plexiglass pipe. The transducers used for estimation of the quasi 1D burning velocity are indicated.

Summary of the simulations in RCMLAB

Five campaigns of simulations have been performed with the RCMLAB code. A brief summary of the results is provided in this subsection.

1. Simulations have been performed of the experiments in 1, 2 and 5 m steel pipes with propane-air mixtures. There is good agreement between the simulated and experimental pressure histories, but the deviations become larger with longer pipes. One reason for this is the greater distance between the transducers in the longer pipes.
2. Simulations have been performed of experiments with propane-air mixtures where the flame front propagation was captured by four photodiodes along the pipe. The experimental pressure data is used to estimate the quasi 1D burning velocity, and there is adequate agreement in the flame arrival times between the experimental and numerical results.
3. Simulations with acetylene-air mixtures showed that the methods in RCMLAB also give good results for fast flame propagation. There was good agreement between experimental and numerical pressure histories except when very abrupt pressure rises occurred in the experiments. The simulated flame front propagation did also follow the experimental flame arrival times.
4. Capturing the flame propagation with an SLR camera made the oscillations in the flame propagation clear, with an increased radiation where the flame speed was reduced. The same oscillations in the energy release were also obtained in the simulations.
5. Simulations of the experiments where the flame propagation was captured by a high-speed camera gave nearly the same propagation of the flame front as in the experiments.

Chapter 5

Conclusions

In this work, gas explosions in pipes have been studied. Focus has been on the development of numerical models that can handle flame propagation in industrial pipelines.

Numerical calculations have been performed with a MATLAB version of the Random Choice Method (RCMLAB) and with the commercial CFD code FLACS. Experimental results have been obtained for pipes of different dimensions and materials, and for different fuel-air mixtures. In the following sections, the main conclusions and recommendations for further work are presented.

A Road Map has been used during the project, and the last version is shown in Figure 1.2. One of the original main targets was to develop models that could handle DDT in pipes. However, to handle DDT properly it appeared to be necessary for the foregoing FA to also be handled properly. It was therefore decided first to concentrate on the FA process. Most of the work has therefore been devoted to the study and modeling of deflagration and pressure waves in smooth pipes. During the project, the RCMLAB code was introduced and the focus has become towards development of this code more than towards FLACS. The work with FLACS has therefore been limited to testing the code for gas explosions in pipes and to define some crucial parameter values. In RCMLAB, new methods that have improved the calculation of flame propagation in pipes have been introduced. The numerical results are compared to the obtained experimental results, but are neither compared directly to other published experimental results nor to a particular accident.

5.1 Main conclusions

The main conclusions of this work can be summarized as follows:

- The RCMLAB code is used for the calculation of pressure waves and flame propa-

gation in pipes. Even though the model is one-dimensional and the gas explosion is a three-dimensional phenomenon, there is good agreement between numerical results and experiments. The main advantage of the RCM is its unique capability for predicting complex wave interactions while maintaining the discontinuities of shock waves and contact surfaces. The RCMLAB code has proved to be useful for the calculation of pressure and deflagration waves in pipes.

- A unique method for the estimation of a quasi 1D burning velocity during gas explosions in pipes has been developed in RCMLAB. The quasi 1D burning velocity is estimated from experimental pressure records from transducers along the pipe and is used as an input parameter to the combustion model. The results of this method have increased the understanding of how the 1D burning velocity will behave during the various phases in the propagation process of a flame front in a pipe. This knowledge will be useful in the development of general models for the burning velocity.
- An experimental data set has been obtained. The data set is used for validation of and as input values to the numerical models. The experimental work has been performed with steel pipes of 22.3 mm ID and lengths of 1, 2, 5 and 11 m, and with a 1.9 m long plexiglass pipe of 40 mm ID. Propagation of flame fronts and pressure waves is recorded by pressure transducers, photodiodes, a digital SLR camera and a digital high speed camera. Fuel-air mixtures including the fuels propane, acetylene and hydrogen have been used.
- A method for estimation of the conditions at a pipe outlet has been developed in RCMLAB. The conditions are estimated by using the experimental pressure records from a transducer near the pipe outlet as the reference. These pipe outlet conditions have proven to be of major importance for flame propagation in pipes. This importance is mainly because the pressure waves reflected at the pipe outlet will interact with the flame front.
- The results with RCMLAB demonstrate that the Euler equations alone are not adequate to calculate the flame propagation in a pipe properly, because friction and heat transfer along the pipe wall will have a significant impact on the flame propagation. The effects of friction and heat transfer are included by an operator-splitting method, which improved the simulation results compared to the experiments. Heat transfer is introduced by a Reynolds analogy.
- FLACS has been tested for flame propagation in pipes by keeping the burning velocity constant. Results show that to avoid damping of the longitudinal

acoustic oscillations that occur in a pipe during slow flame propagation there should be at least 7 grid cells in each direction of the pipe cross-section and it is necessary with time steps given by $CFLC \leq 1$.

- The enhancement factor used in the quasi laminar burning velocity model in FLACS seems to be too high for flame propagation in the initial phase, before the first flame inversion, for the present test conditions with a square pipe of $40 \times 40 \text{ mm}^2$ cross sectional area.
- The initial development of the flame front has shown to be determinant for the further progress of the flame front. To calculate the flame propagation correctly it is therefore necessary to have sufficient knowledge and good models also for the first phases in the propagation process. It is therefore not possible to judge the turbulent propagation in pipes in FLACS before the first phases are calculated correctly.
- During the flame propagation, experiments and simulations have shown that inversions of the flame front occur. These inversions appear to be controlled by the quenching of the flame front at the pipe wall or by interactions of the flame front with acoustic oscillations in the pipe. For pipes above a certain length, which is determined by the pipe diameter and mixture reactivity, the first inversion is determined only by flame quenching at the pipe wall. For shorter pipes, such as the 1 m pipe steel pipe with propane-air mixtures, the first inversion can also be influenced by the pressure waves in the pipe. For fast flames, the interaction with pressure waves would probably have a minor impact on the flame propagation, but for slow flames, several inversions due to interactions with the pressure waves can occur. For long pipes, secondary flame inversions, which are controlled only by the wall quenching, could occur. This was observed for propane-air mixtures in both the 5 m and 11 m pipes.
- For mixtures with high reactivity, flame acceleration creates a steep pressure wave or a shock wave. Pressure transducers connected to small apertures in the pipe wall, have been tested in shock tube experiments . Kistler 7261 had a response time of 2 - 3 ms and was not able to measure the pressure rise from strong FA in an acceptable time range, while the Kistler 603B in the present set-up had a lower response time of around 0.5 ms and provided better results.

5.2 Recommendations for further work

This work has contributed to an increased knowledge of flame propagation in pipes. It has created a basis for further development of the 1D RCMLAB code and has indicated directions for further experimental work with flame propagation in pipes. The most obvious recommendations for further work will be:

- To develop a general model for the quasi 1D burning velocity in RCMLAB. The results from the estimation method for the quasi 1D burning velocity have provided knowledge of the quasi 1D burning velocity, which should be used to develop a general model.
- To develop a general 1D model for the conditions at pipe outlets in RCMLAB. As with the quasi 1D burning velocity, the estimation method has provided increased knowledge of the outlet conditions, which should be used further.
- To extend the RCMLAB code to handle DDT and detonations. It is also necessary to perform more experiments with DDT and detonations in pipes to obtain data sets which can be used for this purpose.
- To increase the understanding of the complex interactions between a flame front and the acoustic oscillations in a pipe. This includes both rarefaction and compression waves that reach the flame front from both the burnt and unburnt side. These investigations should be performed with a high-speed camera and by use of schlieren techniques.
- To use a pretrigger in the data acquisition system to exactly determine the ignition time. In this work, the logging is triggered by inducing a signal from the high voltage wires to the igniter sparks, but system delays, particular in the software, make the exact determination of the ignition time difficult.
- To use pressure transducers with a short enough response time in the actual set-up. Pipes with quadratic cross-sections could also be used, because the transducers can then be installed directly into the pipe wall.

5.3 End statement

This work shows critical mechanisms which are important during flame propagation in smooth pipes. Numerical and experimental studies have been performed to describe these mechanisms. The work is unique in the way experimental pressure data is used to simulate flame propagation in pipes.

Bibliography

- Arntzen, B. J. (1998), Modelling of Turbulence and Combustion for Simulation of Gas Explosions in Complex Geometries, PhD thesis, Norwegian University of Science and Technology.
- Bartenev, A. M. & Gelfand, B. E. (2000), ‘Spontaneous initiation of detonations’, *Progress in Energy and Combustion Science* **26**, 29–55.
- Bartknecht, W. (1981), *Explosions: Course, Prevention, Protection*, Springer-Verlag, New York.
- Bielert, U., Klug, M. & Adomeit, G. (1996), ‘Application of front tracking techniques to the turbulent combustion processes in a single stroke device’, *Combustion and Flame* **106**, 11–28.
- Bjerketvedt, D. (1985), Re-Initiation of Detonation Across an Inert Region, PhD thesis, Norwegian University of Science and Technology.
- Bjerketvedt, D., Hjertager, B. H. & Tokheim, L.-A. (1997), Vurdering av eksplosjon i rørledning 13/4-97 ved HPI (in Norwegian), Technical Report 220217-1, Tel-Tek.
- Bjerketvedt, D., Kristoffersen, K., Vaagsaether, K., Mjaavatten, A. & Thomas, G. (2003), ‘A method for estimating the burning velocity in a tube by using experimental pressure records and the 1-d RCMLAB code’, *Proceedings of the 19th ICDEERS* .
- Bjerketvedt, D., Kristoffersen, K., Vaagsaether, K., Mjaavatten, A. & Thomas, G. (2004), ‘A method for estimating the burning velocity in a tube by using experimental pressure records and the 1-d RCMLAB code’, *Combustion Science and Technology* .
- Bjerketvedt, D. & Mjaavatten, A. (2001), ‘Simulation of gas dynamic flow with a matlab version of the random choice method (RCM)’, *Proceedings of the Nordic Matlab Conference 2001* .

- Bjerketvedt, D., Vaagsaether, K., Kristoffersen, K., Mjaavatten, A., Thomas, G. & Bambrey, R. (2002), 'Simulation of gas explosions with a matlab version of the random choice method (RCM)', *Journal de Physique IV France* **12**, 247–251.
- Bradley, D. (1992a), 'How fast can we burn?', *Proceedings of the Combustion Institute* **24**, 247–262.
- Bradley, D. (1999), 'Flame propagation in a tube: The legacy of henri guénoche', *Proceedings of the 17th ICDERS* .
- Bradley, D. (2002), 'Problems of predicting turbulent burning rates', *Combustion Science and Modeling* **6**, 361–382.
- Bradley, D., Lau, A. K. C. & Lawes, M. (1992b), 'Flame stretch rate as a determinant of turbulent burning velocity', *Phil. Trans. R. Soc. London* **338**, 359–387.
- Bradley, D., Sheppard, C. G. W. & Wolley, R. (2001), 'Unstable explosion flames and acoustic oscillations', *Proceedings of the 18th ICDERS* .
- Bratseth, A., Løvåsen, H., Talberg, O., Skage, F. K., Suttner, T. & Dreetz, C. D. (2002), Granskning av antennelse i fakkelsystemet på sleipner t 10.09.2002 (in Norwegian), Technical Report RUH 195893, Statoil.
- Bray, K. N. C. (1990), 'Studies of the turbulent burning velocity', *Proceedings of the Royal Society of London* **431**, no. **1882**, 315 – 335.
- Butler, T. D., Cloutman, L. D., Dukowicz, J. K. & Ramshaw, J. D. (1981), 'Multidimensional numerical simulation of reactive flow in internal combustion engines', *Progress in Energy and Combustion Science* **7**, 293–315.
- Butler, T. D. & O'Rourke, P. J. (1976), 'A numerical method for two dimensional unsteady reacting flows', *Proceedings of the Combustion Institute* **16**, 1503–1515.
- Chatrathi, K. & Going, J. (1996), 'Pipe and duct deflagrations associated with incinerators', *Process Safety Progress* **15**(4), 237–246.
- Chatrathi, K., Going, J. E. & Grandstaff, B. (2001), 'Flame propagation in industrial scale piping', *Process Safety Progress* **20**(4), 286–294.
- Chorin, A. J. (1976), 'Random choice solution of hyperbolic systems', *Journal of Computational physics* **22**, 517–533.
- Chorin, A. J. (1977), 'Random choice methods with applications to reacting gas flow', *Journal of Computational physics* **25**, 253–272.

- Chorin, A. J. (1980), 'Flame advection and propagation algorithms', *Journal of Computational Physics* **35**, 1–11.
- Chu, B.-T. (1952), 'On the generation of pressure waves at a plane flame front', *Proceedings of the Combustion Institute* **4**, 603–612.
- Clanet, C. & Searby, G. (1996), 'On the "tulip flame" phenomenon', *Combustion and Flame* **105**, 225–238.
- Clanet, C. & Searby, G. (1998), 'First experimental study of the darrieus-landau instability', *Physical Review Letters* **80**(17), 3867–3870.
- Danköehler, G. (1947), 'The effect of turbulence on the flame velocity in gas mixtures', *NACA* **1112**.
- Dorofeev, S. B. (2002), 'Flame acceleration and DDT in gas explosions', *Journal de Physique IV France* **12**, 3–10.
- Dorofeev, S. B., Kuznetsov, M. S., Alekseev, V. I., Efimenko, A. A. & Breitung, W. (2001), 'Evaluation of limits for effective flame acceleration in hydrogen mixtures', *Journal of Loss Prevention in the Process Industries* **14**, 583–589.
- Eckert, E. R. G. & Drake, R. M. (1987), *Analysis of Heat and Mass Transfer*, 3rd edn, Hemisphere Publishing Corporation, New York.
- Ellis, O. C. & Wheeler, R. V. (1928), 'Explosion in closed cylinders. part III. the manner of movement of flame', *Journal of Chemical Society* pp. 3215–3218.
- GexCon (1998), 'FLACS-98 user's guide'.
- Ghoniem, A. F., Chorin, A. J. & Oppenheim, A. K. (1982), 'Numerical modelling of turbulent flow in a combustible tunnel', *Phil. Trans. Royal Society London* **304**, 303–325.
- Glimm, J. (1965), 'Solutions in the large for nonlinear hyperbolic systems of equations', *Communications of Pure and Applied Mathematics* **18**, 697–715.
- Gottlieb, J. (1986), 'Random-choice method for solving one-dimensional unsteady flows in ducts, shock tubes and blast-wave simulators', *AC-Laboratorium Spiez, Switzerland*.
- Guénoche, H. (1964), Flame propagation in tubes and in closed vessels, *in* G. H. Markstein, ed., 'Non-Steady Flame Propagation', Pergamon, Berlin, pp. 107–181.

- He, L. (2000), 'A scaling analysis of the critical conditions for a deflagration-to-detonations transition', *Combustion Theory Modelling* **4**, 107–122.
- Johansen, B. A. (2003), Gasseksplasjoner i rør - visualisering av flammer (in Norwegian), Master's thesis, Telemark University College, Norway.
- Jones, S. A. S. & Thomas, G. T. (1991), 'Pressure hot-wire and laser doppler anemometer studies of flame acceleration in long tubes', *Combustion and Flame* **87**, 21–32.
- Kawakami, T., Okajima, S. & Sakuraya, T. (1999), 'Flame investigation of very lean propane-air mixtures under microgravity', *Proceedings of the 5th International Microgravity Combustion Workshop* .
- Kays, W. M. & Crawford, M. E. (1993), *Convective Heat and Mass Transfer*, 3rd edn, McGraw-Hill, New York.
- Kerampran, S., Desbordes, D. & Veyssi re, B. (1999), 'Study of the mechanisms of flame acceleration in a tube of constant cross section', *Proceedings of the 17th ICDEERS* .
- Kerampran, S., Desbordes, D. & Veyssi re, B. (2000), 'Study of the mechanisms of flame acceleration in a tube of constant cross section', *Combustion Science and Technology* **158**, 71–91.
- Kerampran, S., Desbordes, D. & Veyssi re, B. (2001), 'Propagation of a flame from the closed end of a smooth horizontal tube of variable length', *Proceedings of the 18th ICDEERS* .
- Khokhlov, A. M., Gamezo, V. N. & Oran, E. S. (2001), 'Effects of boundary layers on shock-flame interactions and DDT', *Proceedings of the 18th ICDEERS* .
- Khokhlov, A. M. & Oran, E. S. (1999a), 'Numerical simulation of detonation initiation in a flame brush: The role of hot spots', *Combustion and Flame* **119**, 400–416.
- Khokhlov, A. M., Oran, E. S. & Thomas, G. O. (1999b), 'Numerical simulation of deflagration-to-detonation transition: The role of shock-flame interactions in turbulent flames', *Combustion and Flame* **117**, 323–339.
- Khokhlov, A. M., Oran, E. S. & Wheeler, J. C. (1997), 'A theory of deflagration-to-detonation transition in unconfined flames', *Combustion and Flame* **108**, 503–517.
- Knystautas, R., Guirao, C., Lee, J. H. & Sulmistras, A. (1984), 'Measurement of cell size in hydrocarbon-air mixtures and predictions of critical tube diameter, critical initiation energy and detonability limits.', *Prog. Astronaut. Aeronaut.* **94**, 23–37.

- Kristoffersen, K., Johnsen, B. A., Johnsen, T. & Bjerketvedt, D. (2003a), 'Qualitative evaluation of pressure and radiation data from experiments and matlab simulations', *Proceedings of the Nordic Matlab Conference 2003* pp. 85–90.
- Kristoffersen, K., Vaagsaether, K., Bjerketvedt, D. & Thomas, G. (2003b), 'Estimation of the burning velocity for flame propagation in smooth pipes', *Proceedings of the 3rd Mediterranean Combustion Symposium* pp. 41–49.
- Kristoffersen, K., Vaagsaether, K., Bjerketvedt, D. & Thomas, G. (2004), 'Propane-air pipe explosion experiments. data for estimation of 1-d burning velocity in slow regimes.', *Experimental Thermal and Fluid Science Journal* **28**(7), 723–728.
- Kuo, K. K. (1986), *Principles of Combustion*, John Wiley and Sons, New York.
- Kuznetsov, M., Alekseev, V., Bezmelnitsyn, A., Breitung, W., Dorofeev, S., Matsukov, I., Vesper, A. & Yankin, Y. (1999), Effect of obstacle geometry on behaviour of turbulent flames, Technical Report FZKA-6328, IAE-6137/3, Russian Research Centre "Kurchatov Institute", Forschungszentrum Karlsruhe.
- Kuznetsov, M., Alekseev, V., Matsukov, I. & Dorofeev, S. (2003), 'DDT in hydrogen-oxygen mixtures in smooth tubes', *Proceedings of the 19th ICEDERS* .
- Kuznetsov, M., Aleseev, V., Yankin, Y. & Dorofeev, S. (2002), 'Slow and fast deflagrations in hydrocarbon-air mixtures', *Combustion Science and Technology* **174**, 157–172.
- Laviolette, J.-P., Higgins, A. J. & Lee, J. H. S. (2003), 'Interaction between a flame and a rarefaction', *Proceedings of the 19th ICEDERS* .
- Law, C. K. (1993), A compilation of experimental data on laminar burning velocities, in N. Peters & B. Rogg, eds, 'Reduced Kinetic Mechanisms for Application in Combustion Systems', Springer-Verlag, New York, pp. 15–26.
- Lee, J. H., Knystautas, R. & Yoshikawa, N. (1978), 'Photochemical initiation of gaseous detonations', *Acta Astronautica* **5**, 971–982.
- Mallard, M. & Chatelier, . L. (1883), 'Combustion des mélanges gazeux explosifs', *Annales des Mines, Paris* **8**, 274–377.
- Manson, W. & Wheeler, R. V. (1920), 'The propagation of flame in mixtures of methane and air. part i. horizontal propagation', *Journal of the Chemical Society* **117**, 36–47.

- Markstein, G. H. (1956), 'A shock-tube study of flame front-pressure wave interaction', *Proceedings of the Combustion Institute* **6**, 387–398.
- Moen, I. O. (1993), 'Transition to detonation in fuel-air explosive clouds', *Journal of Hazardous Materials* **33**, 159–192.
- Mueller, C. J., Driscoll, J. F., Reuss, D. L. & Drake, M. C. (1996), 'Effects of unsteady stretch on the strength of a freely-propagating flame wrinkled by a vortex', *Proceedings of the Combustion Institute* **26**, 347–355.
- Neumann, J. V. & Richtmyer, R. D. (1950), 'A method for the numerical calculation of hydrodynamic shocks', *Journal of Applied Physics* **21**, 232–237.
- Noh, W. F. & Woodward, P. (1976), 'SLIC (simple line interface calculation)', *Proceedings of the 5th Int. Conf. Numer. Math. Fluid Mech.* pp. 330–339.
- O'Rourke, P. J. & Bracco, F. V. (1979), 'Two scaling transformations for the numerical computation of multidimensional unsteady laminar flames', *Journal of Computational Physics* **33**, 185–203.
- Pande, J. O. & Tonheim, J. (2001), 'Ammonia plant NII: Explosion hydrogen in a pipeline for CO₂', *Process Safety Progress* **20**(1), 37–40.
- Peraldi, O., Knystautas, R. & Lee, J. H. (1986), 'Criteria for transition to detonation in tubes', *Proceedings of the Combustion Institute* **21**, 1629–1637.
- Richtmyer, R. D. (1960), 'Taylor instability in shock acceleration of compressible fluids', *Communication on Pure and Applied Mathematics* **13**, 297–319.
- Saito, T. & Glimm, I. I. (1979), Applications of random-choice method to problems in shock and detonation-wave dynamics, Technical Report UITAS Report no. 240, CN ISSN 0082-5255, Institute for Aerospace Studies, University of Toronto.
- Salamandra, G. D., Bazhenova, T. V. & Naboko, I. M. (1959), 'Formation of detonation wave during combustion of gas in combustion tube', *Proceedings of the Combustion Institute* **7**, 851–855.
- Schlichting, H. & Gersten, K. (2000), *Boundary Layer Theory*, 8th edn, Springer-Verlag, Berlin.
- Schmidt, E. H. W., Steinecke, H. & Neubert, U. (1952), 'Flame and schlieren photographs of combustion waves in tubes', *Proceedings of the Combustion Institute* **4**, 658–666.

- Sethian, J. (1984), ‘Turbulent combustion in open and closed vessels’, *Journal of Computational Physics* **54**, 425–456.
- Shy, S. S., Lin, W. J. & Peng, K. Z. (2000), ‘High-intensity turbulent premixed combustion: General correlations of turbulent burning velocities in a new cruciform burner’, *Proceedings of the Combustion Institute* **28**, 561–568.
- Sivashinsky, G. I. (2002), ‘Some developments in premixed combustion modeling’, *Proceedings of the Combustion Institute* **29**.
- Sobesiak, A., Battoei, M., Barbour, E., Mackellar, S. & Ting, D. (2003), ‘Flame inversion in a rectangular duct with 90 bend’, *Proceedings of the 19th ICDEERS*.
- Sod, G. A. (1977), ‘A survey of several finite difference methods for systems of non linear hyperbolic conservation laws’, *Journal of Computational Physics* **83**, 232.
- Steen, H. & Schampel, K. (1983), ‘Experimental investigation on the run-up distance of gaseous detonations in large pipes’, *Proceedings of the 4th International Symposium on Loss Prevention and Safety Promotion in Process Industries Series No. 82*, E23–33.
- Taylor, G. (1950), ‘The instability of liquid surfaces when accelerated in a direction perpendicular to their planes’, *Proceedings of the Royal Society of London CCI*, 192–196.
- Texas Instruments Inc. (1995), *TSL250, TSL251, TSL252 Light-to-Voltage Optical Sensors*.
- Thomas, G. O. (1999), ‘Some observation on flame acceleration and the development of detonation in process pipelines’, *5th SAFETYNET seminar*.
- Thomas, G. O., Sands, C. J., Brambrey, R. J. & Jones, S. A. (1997), ‘Experimental observations of the onset of turbulent combustion following shock-flame interaction’, *Proceedings of the 16th ICDEERS*.
- Toro, E. F. (1999), *Riemann Solvers and Numerical Methods for Fluid Dynamics*, Springer-Verlag, Berlin.
- Urtiew, P. A. & Oppenheim, A. K. (1966), ‘Experimental observations of the transition to detonation in an explosive gas’, *Proceedings of the Royal Society of London Series A*, 13–28.

- Veser, A., Breitung, W. & Dorofeev, S. B. (2002), 'Run-up distance to supersonic flames in obstacle-laden tubes', *Journal de Physique IV France* **12**, 333–340.
- Veyssi re, B., Arrigoni, M. & Kerampran, S. (2002), 'Influence of mixture composition on the oscillatory behaviour of flames propagating from the closed end toward the open end of smooth horizontal tubes', *Journal de Physique IV France* **12**, 265–271.
- Veyssiere, B., Kerampran, S., Proust, C. & Gilles, S. (2003), 'Effect of tube length on flame acceleration and DDT in tubes of constant cross section', *Proceedings of the 19th ICDEERS*.
- Warnatz, J., Maas, U. & Dibble, R. W. (1999), *Combustion*, Springer-Verlag, Berlin.
- Williams, F. A. (1985), *Combustion Theory*, Perseus Books, Reading, Massachusetts.
- Zeldovich, Y. B. (1980), 'Regime classification of an exothermic reaction with nonuniform initial conditions', *Combustion and Flame* **39**, 211–214.
- Zeldovich, Y. B., Librovich, V. B., Makhviladze, G. M. & Sivashinsky, G. I. (1970), 'On the development of detonation in a non-uniform preheated gas', *Astronautica Acta* **15**, 313–321.